

# Controlling Local Physico-Chemical Properties of Colloidal Particles and their Self-Assembled Structures

Dissertation

Zur Erlangung des Akademischen Grades

„Doktor der Naturwissenschaften“

Im Promotionsfach Chemie

Vorgelegt dem Fachbereich 09, Chemie, Pharmazie und Geowissenschaften  
der Johannes Gutenberg-Universität Mainz

von

**Karina Bley**

Mainz, 2015



Die vorliegende Arbeit wurde am Max-Planck-Institut für Polymerforschung in Mainz von Mai 2012 bis Juni 2015 angefertigt. Ich versichere, die vorliegende Arbeit selbstständig angefertigt zu haben. Alle verwendeten Hilfsmittel und Quellen habe ich eindeutig als solche kenntlich gemacht.

Mainz, den 05.11.2015

---

Karina Bley

Dekan: Prof.



Erster Gutachter:



Zweiter Gutachter:



Tag der mündlichen Prüfung:



# **Meiner Familie**

*„Alles Schwierige hat seinen Ursprung im Leichten und alles Große im Kleinen.“*

- Laozi, Chinesischer Philosoph -

## Inhalt

1. List of Abbreviations .....	2
2. Abstract .....	5
3. Introduction and Outline .....	6
4. Theoretical Considerations .....	9
4.1. Colloid Stability and Forces at the Air-Water Interface .....	9
4.1.1. Electrostatic Interactions .....	9
4.1.2. Van der Waals Interactions .....	12
4.1.3. DLVO Theory .....	13
4.1.4. Forces at the Air-Water Interface Not Considered in DLVO Theory .....	14
4.2. Structure Control in Two-Dimensional Crystallization of Colloids .....	17
4.2.1. Hexagonal Close-Packed Colloidal Monolayers .....	18
4.2.2. Binary Colloidal Monolayers .....	19
4.2.3. Non-Close-Packed Colloidal Monolayers .....	20
5. Characterization Techniques .....	22
5.1. The Langmuir Trough .....	22
5.2. Scanning Electron Microscopy .....	26
5.3. Atomic Force Microscopy .....	27
6. Results and Discussion .....	29
6.1. Direct Visualization of the Interfacial Position of Colloidal Particles and their Assemblies 29	
6.1.1. The Contact Angle of Nanoparticles in Hexagonal Closed-Packed Arrangements ....	35
6.1.2. Conclusion and Outlook for Section 6.1 .....	39
6.2. Architecture control in Two-Dimensional Colloidal Self-Assembly at the Air-Water Interface .....	40
6.2.1.1. Amphiphilic Copolymers and their Effect on Colloidal Self-Assembly .....	43
6.2.1.2. The Effect of Additives in the Water Subphase on the Amphiphile-Driven Self- Assembly of Carboxylated Polystyrene Particles .....	58

6.2.1.3. Investigation of the Elastic Properties of the Colloid-Copolymer Hybrid Film .....	67
6.2.1.4. From Particle Chains to Square Arrangements– Architecture Prediction .....	69
6.2.2. Conclusion and Outlook of Section 6.2 .....	71
6.3. Controlling Local Optical Properties in Colloidal Monolayers .....	73
6.3.1. Concept of Photoswitchable Colloidal Pixels in Monolayers .....	73
6.3.2. Photo-Physical Properties of Nanoparticles with Photoswitchable Emission .....	77
6.3.2.1. UV-light Induced Photocyclization Reaction in Colloids Prepared by Miniemulsion Polymerization.....	80
6.3.2.2. VIS-light Induced Reverse Cyclization Isomerization Reaction in Colloids Prepared by Miniemulsion Polymerization .....	83
6.3.2.3. Reversibility of the Cyclization Process.....	83
6.3.2.4. Thermal Stability of the Photo-States in Colloids Prepared by Miniemulsion Polymerization.....	84
6.3.2.5. UV-light Induced Photocyclization Reaction in Colloids Prepared by Seeded Emulsion Polymerization.....	85
6.3.2.6. VIS-light Induced Reverse Cyclization Isomerization Reaction and Thermal Stability of the Photo-States in Colloids Prepared by Seeded Emulsion Polymerization .....	87
6.3.3. Self-Assembly of Photoswitchable Colloids at the Air-Water Interface into Complex Binary Monolayers .....	87
6.3.4. Photoswitching in Colloidal Monolayers.....	93
6.3.5. Conclusion and Outlook for Section 6.3.....	95
6.4. Colloidal pH Sensors for the Visualization of pH Dependent Processes in Cells .....	97
6.4.1. Concept for the Visualization of Time-Dependent pH Processes inside Cells by Functionalized Nanoparticles .....	98
6.4.2. Coupling of the pH-Responsive Dye SNARF-1-NHS onto Amine Functionalized Nanoparticles .....	100
6.4.3. Intracellular pH calibration .....	104
6.4.4. Localization and Acidification of pH-Responsive Nanoparticles in Cells .....	106
6.4.5. Conclusion and Outlook for Section 6.4.....	110
7. Experimental Section .....	112

7.1. General Procedures .....	112
7.1.1. Materials .....	112
7.1.2. Carboxyl and Sulfonate Functionalized Nanoparticles by Soap-Free Emulsion Polymerization.....	112
7.1.3. Amine Functionalized Nanoparticles by Soap-Free Emulsion Polymerization .....	113
7.1.4. Cleaning of Colloid Dispersions .....	114
7.1.5. Cleaning of Glass or Wafer Substrates.....	114
7.1.6. Colloidal Monolayer Formation at the Langmuir-Blodgett Trough.....	115
7.1.7. General Analytical Tools.....	115
7.1.7.1. Dynamic Light Scattering and Photon Cross-Correlation Spectroscopy.....	115
7.1.7.2. Zeta-Potential Measurements .....	116
7.1.7.3. Particle Charge Detection .....	116
7.1.7.4. Fluorescamine Assay.....	116
7.1.7.5. Differential Scanning Calorimetry and Thermal Gravimetric Analysis .....	117
7.1.7.6. SEM Measurements .....	117
7.2. Experimental Details for Section 6.1 and 6.2.....	117
7.2.1. Entrapment of Nanoparticles at the Air-Water Interface with Poly(butyl cyanoacrylate).....	117
7.2.2. Preparation of Colloid-Copolymer Mixtures.....	118
7.2.3. Analytical Tools for Section 6.1 and 6.2.....	119
7.2.3.1. Colloidal Probe AFM.....	119
7.2.4. Optical Determination of the contact angle .....	119
7.3. Experimental Details for Section 6.3.....	120
7.3.1. Materials .....	120
7.3.2. Photoswitchable Nanoparticles by Miniemulsion Polymerization .....	120
7.3.3. Photoswitchable Nanoparticles by Seeded Emulsion Polymerization .....	121
7.3.4. Creation of Binary Photoswitchable Colloidal Monolayers .....	122

7.3.5.	Irradiation of the Photoswitchable Dye CMTE in Solutions and Colloids .....	123
7.3.6.	Analytical Tools for Section 6.3.....	123
7.3.6.1.	UV-VIS Spectroscopy .....	123
7.3.6.2.	Fluorescence Emission Spectroscopy .....	123
7.3.6.3.	Confocal Laser Scanning Microscopy .....	124
7.3.6.4.	Fluorescence Microscopy.....	124
7.4.	Experimental Details for Section 6.4.....	124
7.4.1.	Materials .....	124
7.4.2.	Preparation of SNARF-Labeled Nanoparticles .....	125
7.4.3.	Probing of Nanoparticle pH Environment in HeLa Cells .....	125
7.4.4.	Intracellular calibration with SNARF-1-AM Ester and SNARF-1-NP.....	126
7.4.5.	Analytical Tools for Section 6.4.....	126
7.4.5.1.	Fluorescence Emission Spectroscopy .....	126
7.4.5.2.	Confocal Laser Scanning Microscopy .....	127
7.4.5.3.	TEM Measurements .....	127
8.	Bibliography .....	129



## 1. List of Abbreviations

AA	acrylic acid
AFM	atomic force microscopy
AEMH	amino-ethyl methacrylate hydrochloride
APS	ammonium peroxydisulfate
BA	<i>n</i> -butyl acrylate
BCA	butyl cyanoacrylate
BODIPY	4,4-difluoro-1,3,5,7,8-pentamethyl-4-bora-3 <i>a</i> ,4 <i>a</i> -diazas-indacene
<i>c</i>	concentration
CLSM	confocal laser scanning microscopy
CMTE	<i>cis</i> -1,2-dicyano-1,2-bis-(2,4,5-trimethyl-3-thienyl)ethene
CO <sub>2</sub>	carbondioxide
CTMA-Cl	cetyltrimethylammonium chloride
<i>d</i>	days
<i>D</i>	diameter
DLS	dynamic light scattering
DMEM	Dulbecco's Modified Eagle Medium
DMSO	dimethyl sulfoxide
eqn	equation
FCS	fetal calf serum
FRET	Förster resonance energy transfer
fura-2 AM	acetyloxymethyl 2-[5-[bis-[2-(acetyloxymethoxy)-2-oxoethyl]amino]-4-[2-[2-[bis-[2-(acetyloxymethoxy)-2-oxoethyl] amino]-5-methylphenoxy]-ethoxy]-1-benzofuran-2-yl]-1, 3-oxazole-5-carboxylate
<i>h</i>	hours
HBSS	Hank's Balanced Salt Solution
HCl	hydrochloric acid
HD	hexadecane
HEPES	4-(2-hydroxyethyl)-1-piperazineethane sulfonic acid
KCl	potassium chloride
$\lambda_{em}$	emission wavelength
$\lambda_{ex}$	excitation wavelength

MES	2-( <i>N</i> -morpholino) ethane sulfonic acid
min	minutes
MVB	multi vesicular body
NaOH	sodium hydroxide
NaPSS	poly(sodium styrene sulfonate)
NH <sub>4</sub> OH	ammonia solution
N <sub>large</sub>	number of large particles
NP	nanoparticle
N <sub>small</sub>	number of small particles
PAA	poly(acrylic acid)
PBA	poly(butyl acrylate)
PBA-PS	poly(butyl acrylate) particles covered with an additional polystyrene shell
PBCA	poly(butyl cyanoacrylate)
PDADMAC	poly(diallyldimethyl ammoniumchloride)
PESNa	sodium polyethylene sulfonate
PMI	<i>N</i> -(2,6-diisopropylphenyl)-perylene-3,4-dicarboximid
PMMA	poly(methyl methacrylate)
PS	polystyrene
PS-PS	polystyrene particles with additional polystyrene shell
$R_h$	hydrodynamic radius
rpm	round per minute
RT	room temperature
SBFI AM	bis-(acetyloxymethyl) 4-[6-[13-[2-[2, 4-bis-(acetyloxymethoxy carbonyl)phenyl]-5-methoxy-1-benzofuran-6-yl]-1, 4, 10-trioxa-7, 13-diazacyclopenta-dec-7-yl]-5-methoxy-1-benzofuran-2-yl]benzene-1,3-dicarboxylate
SC	solid content
SDS	sodium dodecyl sulfate
SEM	scanning electron microscopy
$\sigma$	standard deviation

SNARF-1	5' (and 6') carboxy-10-dimethylamino-3-hydroxy-spiro-[7 <i>H</i> -benzo[ <i>c</i> ]-xanthene-7,1'(3' <i>H</i> )-isobenzo-furan]-3'-one
SNARF-1-AM	SNARF-1 acetoxymethyl ester acetate
SNARF-1-NHS	SNARF-1 acetate succinimidyl ester
SNARF-1-NP	SNARF-1 labeled nanoparticle
St	styrene
<i>t</i>	time
<i>T</i>	temperature
$t_{1/2}$	half-life time
$T_g$	glass transition temperature
TEM	transmission electron microscopy
VA-044	2,2'-azobis[2-(2-imidazolin-2-yl)propane] dihydrochloride
V59	2,2'-azobis(2-methylbutyronitrile)

## 2. Abstract

In this thesis the physico-chemical properties of colloids and their self-assembled structures are investigated in detail. The focus lies on the fundamental investigation of colloids, their interfacial behavior during self-assembly processes and the influence of the colloid's local environment on the physico-chemical properties.

A novel, versatile entrapment technique was developed to investigate colloids and their interfacial equilibrium position directly at the air-water interface. The entrapment enables to investigate the contact angle position *ex situ* in an scanning electron microscope (SEM), allowing determining local contact angles even for single nanoparticles. The crystallization of nanoparticles into highly crystalline close-packed architectures is well-understood. But as the structure of such colloidal monolayers is limited to hexagonal geometry new techniques have to be developed to create new and more complex architectures. Here, the amphiphile-driven self-assembly approach at the air-water interface of a Langmuir trough is introduced to create reproducibly network- or chainlike packing as well as colloidal assemblies with a pseudo-square lattice. This technique provides the advantage of not using any additional special equipment or pre-treated template substrates as it is commonly used to yield anisotropic self-assembly of colloids. The influence of polymer composition, concentration and manipulation of the electrostatic environment on the chain-like and square arrangements is investigated in detail.

The self-assembly of colloids at the air-water interface is also used to create highly functional two-dimensional colloidal monolayers. The approach of the binary co-assembly of template and functional photoswitchable colloids into complex binary monolayers is used to create locally separated light-responsive nano-pixels as a model system for optical data storage application.

Moreover, functional and trigger responsive nanoparticles are also useful for drug delivery applications in nanomedicine as presented in this work. By functionalization of nanoparticles with a pH responsive dye the path of nanoparticles or nanocapsules through cells can be monitored. Again, localized properties of the nanoparticles and their direct environment can be investigated in detail. Based on the results, drug carriers such as nanocapsules can be designed to release their payload at a distinct position inside the cell upon change of the pH value.

### 3. Introduction and Outline

Nature's ability to form materials with highly complex internal structures from relatively simple building blocks continues to capture scientists' imagining. Though extremely complex in their structural organization, all materials and organisms can be broken down into even smaller building blocks. These, even though they seem small and unimportant, generate the functionality of the entire complex system upon assembly into superstructures with increasing complexity. A very simple analogy can be found in children's playroom. LEGO® stones for instance that appear in different sizes, shapes and colors are also very simple building blocks in the centimeter scale from which impressive macroscopic objects can be assembled in the meter scale. But it is not possible to just stick them chaotically and purposeless together to end up with well-defined architectures. Instead, a systematic plan and design rules need to be followed where every stone placed on another has a special function and affects its environment. Appropriate stones with distinct color, size and shape need to be chosen which form small sub-structures that in turn can be assembled in the right way to complete the construction. This design principle is called a bottom-up process. Of course, this thesis does not focus on the design of macroscopic objects from LEGO® stones. Nevertheless; the essence of the construction principle remains the same with much smaller building blocks.

Within this work, the essential building blocks are colloidal particles. Similar to LEGO® stones there exist a variety of nanoparticles of different material, shape, size, functionality or responsiveness. A single nanoparticle might be not impressing at first glance. When self-assembled at the air-water interface, these simple particles transform into highly crystalline, two dimensional colloidal arrangements. This process, first investigated by Pieranski<sup>[1]</sup> in 1980 is a powerful platform used by material scientists for a variety of applications, ranging from surface-patterning with nanoscale dimension,<sup>[2, 3]</sup> *via* photonic and opalescent structures that mimic the complex structural coloration found in nature,<sup>[4]</sup> to sophisticated bio-sensing architectures capable of detecting analyte molecules with astonishing sensitivity.<sup>[5-10]</sup> The isotropic self-assembly of nanoparticles at the air-water interface into hexagonal close-packed arrangements is well-understood on a micro- and also macroscopic scale. Several interacting forces like electrostatics, van der Waals or capillary forces are balanced at the air-water interface and enable the particles to self-assemble into two-

dimensional crystals with hexagonal symmetry, which is described in the theoretical considerations. But more detailed information about the local physico-chemical properties of single particles and the colloid's direct environment are very rare and hard to collect due to the small size of these building blocks.

The more detailed investigation of fundamental problems in colloidal interaction on the nano-scale is of great importance if we want to understand how to manipulate and control processes to our benefit. Anisotropic self-assembly of nanoparticles into more complex structures for instance is so far not really reproducible and not well-understood. To create more complex arrangements, experimentally difficult processes such as nanoscale templating or the design of nanoparticles with defined patches need to be employed.<sup>[11, 12]</sup> However, such materials promise the extension of properties towards materials with novel optical and physical properties. Alternatively, they can serve as masks with more complex geometries that find applications in lithographic approaches to create nano-structured arrays with outstanding optical and plasmonic properties.<sup>[7, 10, 13]</sup>

This work focuses on the investigation of physico-chemical properties of colloids, their self-assembled structures at the air-water interface and on the determination of characteristics of the colloid's environment with high local resolution.

The thesis is sub-divided into different chapters. First, a short overview is given about colloid self-assembly at the air-water interface and the involved stabilizing and destabilizing forces. Then different architectures that can be formed during the colloidal self-assembly process into two-dimensional monolayers are highlighted (chapter 4). Afterwards, a short introduction is given into the main characterization techniques used in this thesis (chapter 5).

The results and discussion chapter is divided into four sub-chapters. In the first part (chapter 6.1) colloids and their self-assembled structures are investigated in detail concerning their interfacial equilibrium position directly at the air-water interface by a novel gas phase induced interfacial polymerization technique. Thereby, contact angles of individual colloids of different size and composition at aqueous interfaces can be determined. Afterwards, the amphiphile-driven self-assembly process at the air-water interface of a Langmuir trough is introduced and the creation of more complex two-dimensional architectures such as chain-

like and pseudo square arrangements in a simple and reproducible way is demonstrated (chapter 6.2).

This first chapter is followed by the presentation of a functional binary colloidal monolayer with photo-responsive spatially separated nano-pixels which serves as a model system for optical data storage applications (chapter 6.3).

The last chapter is based on another fundamental question of nanoparticles and the environmental interaction. Here, stimuli responsive nanoparticles functionalized with a pH sensitive dye are used to record the pathway through a cell and the variance of the pH upon different transport processes of the particles inside the cell (chapter 6.4).

The results of each chapter are discussed, conclusions are drawn and also an outlook is given. The experimental details can be found in chapter 7.

## 4. Theoretical Considerations

### 4.1. Colloid Stability and Forces at the Air-Water Interface

Dispersed systems are widely known in our everyday life for instance in food industries such as milk, as paints for automotive industries or as pigments in dispersion, as well as in lotions and creams. An essential attribute of such systems is the stability of the containing of the dispersed phase, droplets or particles against flocculation or coagulation. The colloid stability in a continuous medium is a complex multi-body problem with multiple repulsive and attractive forces acting on an individual dispersed particle. To create a stable dispersion, attractive van der Waals forces need to be counterbalanced by repulsive electrostatic forces. This balance of forces is described by the DLVO theory. Repulsive electrostatic, steric and attractive van der Waals forces equilibrate to result an overall interaction potential which can be described by the DLVO theory. This theory was independently discovered by two groups in the 1940s, the Russian physicists **Derjaguin** and **Landau**<sup>[14, 15]</sup> and the Dutch chemists **Verwey** and **Overbeek**<sup>[16]</sup> who are eponym of the theory. The DLVO theory describes colloidal interactions in bulk dispersion. However, if placed at an interface, a colloid experiences another set of forces not present in bulk dispersion. But especially for self-organization of colloids or two-dimensional assembly of nanoparticles into densely packed crystals also interfacial forces such as capillary forces and dipole-dipole interactions at the air-water interface need to be taken into account.

In this chapter, the DLVO theory is described as well as the interplay of the forces affecting colloids at interfaces such as air-liquid or liquid-solid surfaces. This latter is essential to understand crystallization processes and the manipulation of self-organizing systems as they are presented in this work.

#### 4.1.1. Electrostatic Interactions

Colloids and especially nanoparticles are able to interact electrostatically if they carry charges on the particle surface. This interaction can be of attractive or repulsive nature depending on the charge of the individual particles. Considering the presence of equally charged colloids the electrostatic interaction is repulsive. In dispersions the colloids are

surrounded by an electric double layer which can be described using a combination of different models. Gouy-Chapman, Stern and Grahame approximate a colloid surface as a plane charged plate alike a plate capacitor.<sup>[17, 18]</sup> As it is presented in Figure 1 the electric double layer, which is created in an electrolyte environment, can be subdivided into different layers.

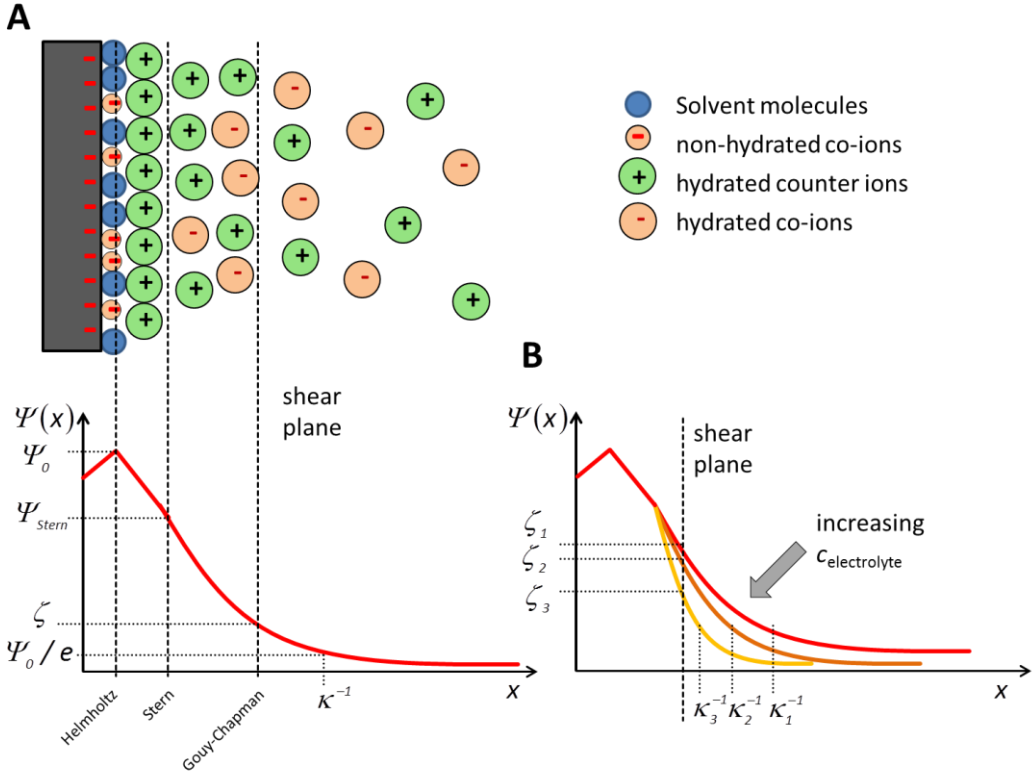


Figure 1 A) Scheme for the formation of an electrical double layer of a charged surface placed in an electrolyte solution correlated with the surface potential ( $\Psi(x)$ ) in dependence on the distance ( $x$ ) from the charged surface. B) The diagram displays the variation of the electrical double layer thickness labeled by the Debye length ( $\kappa^{-1}$ ) and the different zeta-potentials ( $\zeta$ ) with increasing electrolyte concentration.

The first plane is the so-called Stern layer with surface potential  $\Psi_{Stern}$  that can be divided into the inner and the outer Helmholtz layer. The inner Helmholtz plane includes water molecules and non-solvated co-ions equally charged as the charged surface that adsorb strongly on the particle surface. The presence of non-solvated like-charged ions results in an increased surface potential ( $\Psi_0$ ) compared to the charged surface itself. The outer Helmholtz plane consists of larger, completely hydrated counter ions in their closest distance to the

charged surface. The surface potential  $\psi(x)$  decreases linearly from the initial surface potential with increasing distance ( $x$ ) from the charged surface. Thermal motion leads to the formation of a diffuse disordered state of the double layer of different charged ions behind the outer Helmholtz plane. The surface potential at the outer Helmholtz plane represents the Stern potential ( $\psi_{\text{Stern}}$ ). Here, the surface potential decreases exponentially with increasing distance  $x$  following a Poisson-Boltzmann equation.<sup>[19]</sup> For electrical double layers with a potential  $< 25$  mV the surface potential can be expressed by the equation 1. At the so-called zeta-potential which is the electrokinetic potential of the diffuse double layer all ions between the charged surface and the shear plane remain near the particle surface although the colloids move through the dispersion. The Debye-Hückel theory describes the distribution of charged ions in a solution. Similar to atoms in a crystal lattice positive ions are surrounded by negative ones and *vice versa*. Due to thermal motion the ions are not fixed in their position and can move within the solution. But in the average state an ion is surrounded by a contrary charged ion cloud that shields the central ion. The value of this screening length is also called the Debye length  $\kappa^{-1}$  (eq. 2). It describes the thickness of the electrical double layer at which the surface potential has decayed to a value of  $\psi_0/e$ .

$$\Psi(x) = \Psi_0 \cdot \exp(-\kappa x) \quad (\text{eq. 1})^{[19]}$$

$$\kappa^{-1} = \sqrt{\frac{\varepsilon \varepsilon_0 k_B T}{2 N_A e^2 I}} \quad (\text{eq. 2})^{[20]}$$

Here,  $\varepsilon_0$  stands for the permittivity in vacuum,  $\varepsilon$  for the dielectric constant,  $k_B$  for the Boltzmann constant,  $T$  for the temperature in Kelvin,  $e$  for the elementary charge,  $N_A$  for the Avogadro constant and  $I$  for the ionic strength.<sup>[20]</sup> The electrolyte concentration has a drastic influence on the stability of the colloid dispersion. As can be seen in Figure 1 the surface potential decays faster with increasing electrolyte concentration. The diffuse layer is even more compressed at high salt concentrations which results in a lower potential at the shear plane. The valence of the electrolyte ions also controls the rate of the surface potential decay. Using for instance  $\text{Al}^{3+}$  instead of  $\text{Na}^+$  ions leads to a much faster coagulation which is described by Schulze-Hardy rule.

### 4.1.2. Van der Waals Interactions

Contrary to the repulsive electrostatic forces at large distances from the colloid surfaces at short distances strong attractive forces drive the colloids to coagulate. These short ranged forces are described by van der Waals attraction, which are based on molecular dipole-dipole interactions. Thereby, different attractive dipole interactions can occur between permanent dipoles (Keesom,  $V_{Keesom}$ ), permanent and induced dipoles (Debye,  $V_{Debye}$ ) or between completely induced dipoles (London,  $V_{London}$ ). All appearing forces are incorporated in the van der Waals potential ( $V_{vdW}$ ) which is inversely proportional to the colloid distance such as  $V_{vdW} \sim x^{-6}$  (eq. 3):

$$V_{vdW} = V_{Keesom} + V_{Debye} + V_{London} = \frac{C_{1,2}}{x^6} \quad (\text{eq. 3})$$

The constant  $C_{1,2}$  contains all important information about dipole moments, polarizability or ionization energies of the two particles as the van der Waals interactions are highly anisotropic and depend on the relative orientation of the dipoles. When macroscopic objects such as colloids and particles interact with each other the van der Waals force is integrated over the total volume of the spherical particle. For two spheres with radii  $r_1$  and  $r_2$  the van der Waals potential can be described by Derjaguin's approximation with the surface shape of the two approaching spheres as two plates with distance  $x$ .

$$V_{sphere-sphere} = -\frac{A_H}{6x} \cdot \frac{r_1 r_2}{(r_1 + r_2)} \quad (\text{eq. 4})$$

$$A_H = \pi^2 \cdot C_{1,2} \cdot \rho_1 \cdot \rho_2 \quad (\text{eq. 5})$$

Here,  $A_H$  stands for the Hamaker constant describing the power of two interacting particles and depends on the material, with the number of atoms per volume unit of the spheres ( $\rho_1$  and  $\rho_2$ ) as well as the surrounding dispersion medium. If  $r_1 = r_2 = R$  the van der Waals force can be described with Derjaguin's approximation as

$$V_{sphere-sphere} = -\frac{A_H R}{6x} \quad (\text{eq. 6})$$

### 4.1.3. DLVO Theory

The DLVO theory combines attractive and repulsive forces to an overall energy potential  $V_{DLVO}$  in dependency of the distance  $x$  of two approaching colloids as it is presented in Figure 2 and by equation:

$$V_{DLVO} = V_{Born} + \Psi(x) + V_{vdW} \quad (\text{eq. 7})$$

Additional to the already discussed attractive van der Waals ( $V_{vdW}$ ) and the repulsive electrostatic interactions ( $\Psi(x)$ ), the Born repulsion of two hard approaching spheres needs also to be considered for very short distances.

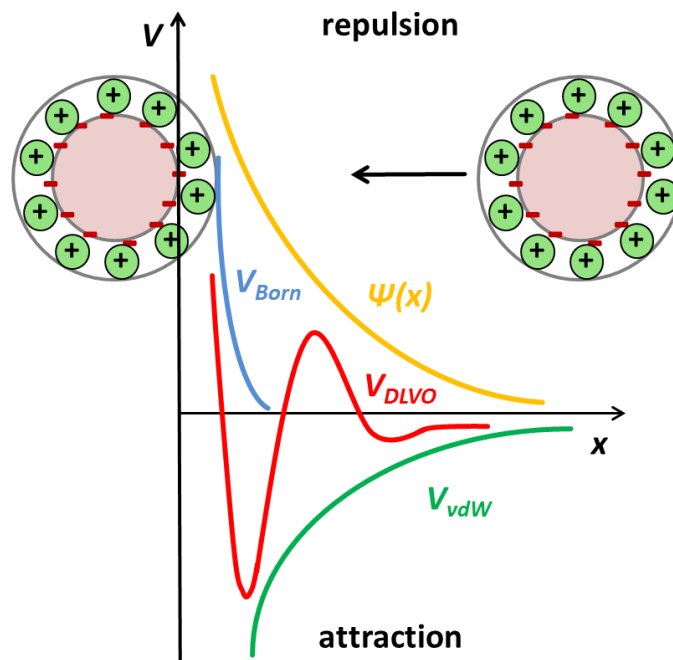


Figure 2 Scheme for the surface potential  $V_{DLVO}$  of two approaching charged colloids depending on the distance  $x$  and attending repulsive electrostatic interactions ( $\Psi(x)$ ), the Born repulsion of two hard spheres ( $V_{Born}$ ) and the attractive van der Waals forces ( $V_{vdW}$ ).

Here, two charged, hard spheres come closer which leads to an overlap of the surrounding ion clouds and a strong and sharp increase in the surface potential ( $V_{Born}$ ) as they are not able to approach more than their radii.

At large colloid distances ( $x$ ) the colloidal spheres are stabilized by electrostatic interactions and repulsion of their like-charged surrounding ion clouds. A small first energy minimum can

be formed where flocculation of the colloids can appear. In general such a flocculation is reversible and colloids can be redispersed by mild energy input such as shaking.

If the particles approach even more the surface potential increases and forms an energy barrier which is mainly characterized by the electrostatic repulsion between the particles. This energy barrier can be decreased by the addition of salts. As described before, the electric double layer is compressed and the particles can approach closer resulting in irreversible coagulation of the particles as the dominating forces are attractive van der Waals interactions at small distances. The coagulation is irreversible because of the strong energetic minimum. Destabilization of the colloidal systems is the consequence.

#### **4.1.4. Forces at the Air-Water Interface Not Considered in DLVO Theory**

Especially when working at interfaces such as air-liquid or liquid-liquid interfaces DLVO theory cannot exclusively explain all appearing phenomena. Nanoparticles with surface functionalities, such as polystyrene colloids copolymerized with acrylic acid in a typical surfactant-free emulsion polymerization,<sup>[21]</sup> carry statistically distributed carboxylic groups on the particle surface. These functional, charged groups stabilize the colloids electrostatically against coagulation. Due the minimization of surface energy the particles are trapped at the air-water interface.<sup>[1, 19]</sup> Geometrically, they are partly immersed into the water phase and act similar to an amphiphilic molecule or surfactant with a polar hydrophilic head group and a hydrophobic tail. The carboxylic groups of the immersed part of the colloid are dissociated extensively compared to the groups localized on the colloidal region protruding out of the water phase which is schematically shown in Figure 3.<sup>[22, 23]</sup>

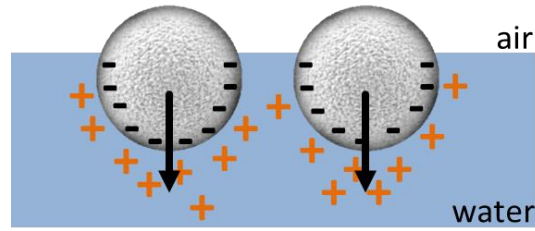


Figure 3 Orientation of repulsive dipole moments originating from heterogeneously distributed surface charges or asymmetric ion clouds for two colloids at the air-water interface.

Pieranski<sup>[1]</sup> proposed an additional electrostatic repulsion of the particles considering the formation of dipole moments directed perpendicular to the air-water interface which is represented by equation 8.

$$E_{dipole-dipole} = \frac{2(Q_x \kappa_x^{-1})^2}{\epsilon x^3} \quad (\text{eq. 8})$$

Here,  $x$  stands for the distance between the particle centers,  $Q_x$  for the charge of the dissociated functional groups in two-dimensions,  $\kappa_x^{-1}$  for the Debye length and  $\epsilon$  for the dielectric conductivity of the medium between the two particles.

### The Contact Angle of Particles at Interfaces and Capillary forces

The presence of colloids located at a liquid interface leads to a deformation of the water surface and of the creation of menisci depending on the properties of the liquid as well as the size, material and functionalization of the particles. The particles have distinct contact angles at the liquid interface which is schematically shown in Figure 4.

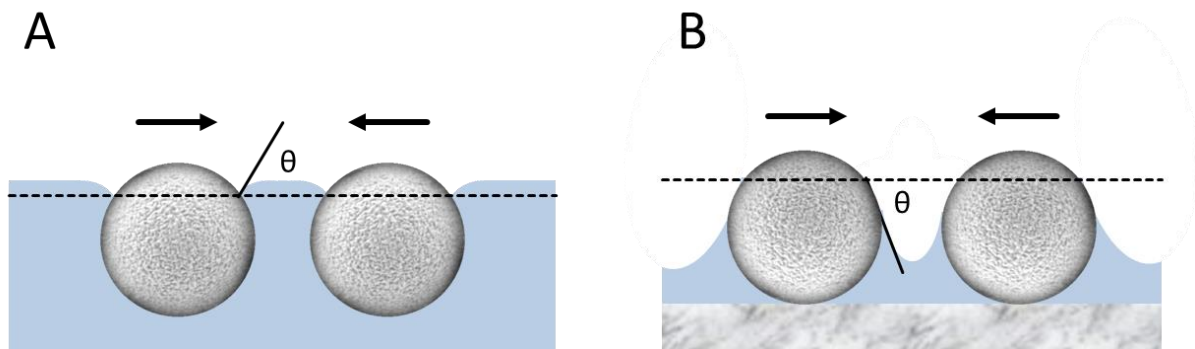


Figure 4 Capillary forces appearing between particles at a liquid interface induced by deformation of the interface and menisci formation, A) flotation force and B) immersion force.

At liquid interfaces hydrophobic nanoparticles typically have a contact angle  $\theta > 90^\circ$  and hydrophilic colloids  $\theta < 90^\circ$  with hydrophilic functionalization such as amines, hydroxyl, sulfate, phosphate or carboxylic groups, always depending on the liquid medium and the particle wettability.<sup>[24, 25]</sup> The appearing lateral capillary forces can either be of attractive or repulsive nature. So called flotation forces (Figure 4A) that deform the interface typically arise in the presence of heavy and large particles (diameter of several  $\mu\text{m}$ ) due to gravity and the buoyancy force.<sup>[25]</sup> When the particles are equal in size the flotation force can be described by a Bessel function  $K_1$ .<sup>[19]</sup>

$$F_{\text{Float}} \propto (R^6/\gamma)K_1(qL) \quad (\text{eq. 9})$$

Here,  $R$  stands for the particle radius,  $\gamma$  for the interfacial tension,  $L$  is the distance between the two particle centers and  $K_1$  represents the Bessel function depending on the radii of the three phase contact line and the capillary length  $q$ .

$$q^{-1} = \sqrt{\frac{\gamma}{\Delta\rho g}} \quad (\text{eq. 10})$$

The capillary length is described by the acceleration due to gravity ( $g$ ), the interfacial tension ( $\gamma$ ) and the density differences  $\Delta\rho$  of the media.

Immersion capillary forces (Figure 4B) usually appear between particles in thin films or on a substrate with a liquid contact line smaller than the particle diameter. Here, the contact line is deformed due to different wettability of the particles in the absence of gravitational forces. The immersion force for equally sized colloids can be described using:

$$F_{\text{Imm}} \propto R^2\gamma \cdot K_1(qL) \quad (\text{eq. 11})$$

The flotation force increases with decreasing interfacial tension and additionally, decreases stronger with smaller particle radius than the immersion force. Different wettability can be based for example on the material of the nanoparticle, heterogeneities of functional groups covering the particle surface, and the surface topography or particle roughness, respectively.

These differences can induce capillary multi-poles which can affect the stability of particle stabilized emulsions or foams as well as on the two-dimensional particle self-assembly at fluid interfaces.<sup>[26, 27]</sup> The long, normally attractive capillary forces are in the range of van der Waals interactions and can extend to several hundreds of nanometers. Thus, they are mostly responsible for the well-known two-dimensional crystallization of nanoparticles at the air-water interface into highly ordered hexagonal colloid packages.<sup>[26, 28]</sup>

### **Depletion Interactions**

Beside all afore mentioned interactions also attractive hydrophobic interactions known as bridging flocculation between polymeric chains of adsorbed amphiphilic molecules, surfactants or dissolved polymers in solution with colloids can occur.<sup>[29-32]</sup> Once the particle surface is fully covered with adsorbed or covalently bound polymeric chains the colloid is sterically stabilized. This kind of stabilization is based on the interactions of the polymeric chains if two covered particles approach. On the one hand, the entropy is lowered as the polymeric chains would have less possible configurations or degrees of freedom to rotate and move if there are other surrounding polymers. On the other hand, an osmotic pressure and solvent flow is generated if the polymeric chains approach as they displace dispersive medium which leads to a concentration imbalance.<sup>[33]</sup> Dissolved non-adsorbing polymers in the direct vicinity of colloids can also force the particles to mostly reversibly form clusters or aggregates also in two dimensions at an interface, which is also known as depletion interaction. Here, the system reduces its total energy by entropic effects and an increase of the polymer coil's degree of freedom by phase separating small polymers from the colloids.<sup>[31, 32]</sup>

## **4.2. Structure Control in Two-Dimensional Crystallization of Colloids**

The understanding of two-dimensional self-assembly of colloids into defined and well-ordered hierarchical structures is of great importance in science or technology and has been studied intensely during the last decades. The formation of colloidal crystals from simple building blocks such as polymeric nano- to micrometer sized spherical particles can be a

powerful tool for materials scientists. The following chapters will concentrate on the self-assembly process of nanoparticles at the air-water interface. The focus lies on how functionality of nanoparticles and structure control in the self-assembly process can be used to create novel devices and coatings with interesting physico-chemical properties that can be further used as a platform or template in nano-lithographic approaches.

#### **4.2.1. Hexagonal Close-Packed Colloidal Monolayers**

Typically, well-ordered hexagonal densely packed colloidal monolayers are formed when nanoparticles are self-assembled at an interface. Pieranski<sup>[1]</sup> first reported on colloid crystallization of polystyrene spheres at the air-water interface in 1980 and described how particles are strongly trapped at an air-water interface. Since the discovery of 2D colloidal crystals, various methods have been developed to create such assemblies. Such colloidal crystals can be easily obtained by various methods working or instance with direct assembly methods using solid substrates such as vertical,<sup>[34]</sup> horizontal,<sup>[35]</sup> or electrostatic deposition,<sup>[36]</sup> or spin-coating.<sup>[37, 38]</sup> Further, also interface-mediated assembly methods such as the Langmuir trough approach are well established to crystallize nanoparticles either at the air-water or liquid-liquid interface.<sup>[39]</sup> Several attempts have focused on further modifying the self-assembly process at the air-water interface to yield large-area defect-free colloidal crystals. Especially pH variation,<sup>[40]</sup> adjustment of the ionic strength by salt addition, or simple modification of the particle's spreading process at the interface<sup>[41, 42]</sup> can be used to obtain even better crystallization results. But also electric<sup>[43]</sup> and magnetic field<sup>[44]</sup> assisted self-assembly approaches are used to assemble functional particles loaded with magnetic entities that are able to orientate their dipoles in the direction of the applied electromagnetic force field.

Materials produced by self-organization of colloids find application in various research fields such as surface patterning,<sup>[2, 3]</sup> photonics in opalescent structures,<sup>[4]</sup> or bio-sensing.<sup>[45]</sup> Inspired by nature, particle-based microstructures can be used to produce biomimetic self-cleaning surfaces similar to the superhydrophobic surface of the lotus leaf.<sup>[46]</sup> The lotus plant can easily repel dust and water caused by sub-micrometer sized pillars as surface topography covered with a special hydrophobic wax, which is well known as the lotus

effect.<sup>[47-49]</sup> Furthermore, self-assembled colloidal structures can be used for instance for nanosphere lithography applications as it has been shown by van Duyne *et al.*<sup>[6]</sup> and others.<sup>[50, 51]</sup> The assembled nanoparticles can serve as masks for the creation of ordered arrays of metal nanostructures in the micro- and nanometer range after applying a metal evaporation or metal sputtering process. Such small metal structures support localized surface plasmon resonances applicable for enhancing Raman signals or to detect binding of biomolecules.<sup>[5, 9, 10, 13, 45, 52]</sup>

### 4.2.2. Binary Colloidal Monolayers

To meet the more and more challenging and complex requirements of science and technology it is of great importance to find solutions to create complexity from simple building blocks. For sure, common hexagonal monolayers provide a wide range of properties such as in the field of photonics and phononics. But also their functionality is somehow limited to simple geometries. To increase the versatility of achievable assembly structures, binary monolayers can provide more complex systems. They consist of a particle mixture of small colloids (S) and larger particles (L). The large particles form a hexagonal lattice, whereas the small colloids are localized in the interstitial sites of the monolayer. Depending on the size ratio of the colloids and on the number ratio of small to large particles different configurations are possible, usually denoted as  $LS_n$  which is schematically shown in Figure 5.

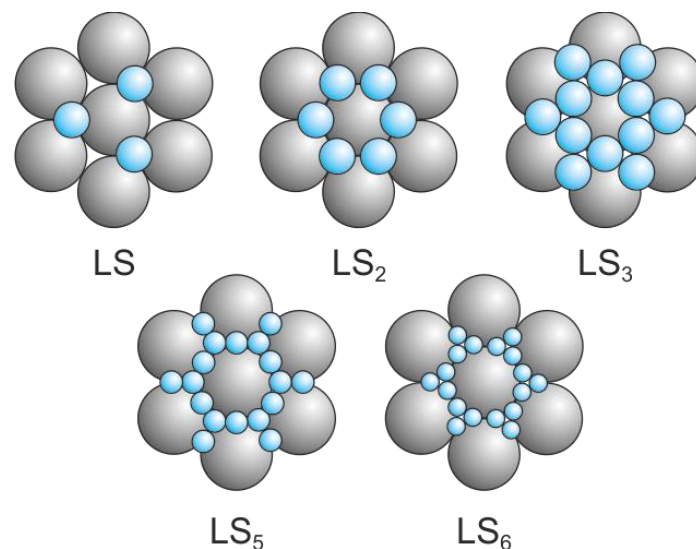


Figure 5 Examples for possible crystal structures in binary colloidal monolayers.

There are several possibilities how to self-assemble colloids in a binary crystal. The easiest way is a one-step process, where large and small colloids are mixed and co-self-assembled simultaneously at the air-water interface.<sup>[53, 54]</sup> Detrich *et al.*<sup>[55]</sup> introduced a Langmuir trough-based self-assembly of silica nanoparticles at the air-water interface but they were not able to gain a precise control over the stoichiometry. As published by Vogel *et al.*<sup>[56]</sup> in 2011, the crystal structure can be tailored more precisely by careful adjustment of the number ratio of large to small particles. They also used a Langmuir trough for the assembly but controlled the number ratio of small to large particles at the air-water interface. With high crystallinity over a large scale the binary colloidal crystals can serve as lithographic platform for the creation of more complex nanostructures applicable for instance in surface patterning and plasmonics.<sup>[3, 5, 6]</sup>

### **4.2.3. Non-Close-Packed Colloidal Monolayers**

During the last years the creation of even more sophisticated structures and lithographic masks has become increasingly important. Scientist investigated in more detail how anisotropic self-assembly of colloids can be controlled and how it can be realized to create new complex materials from the same building blocks that are widely used in nanolithography. There are several ways to control the self-assembly process of nanoparticles to form non-conventional architectures with potentially interesting physico-chemical properties for materials scientists and technology. In the research field of nanosphere lithography for instance even more sophisticated lithographic approaches exist to create highly symmetrical colloidal monolayers. Non-closed packed anisotropic structures can be obtained with individual particles separated spatially by applying an additional size reduction step. For instance a plasma etching process can be used after the self-assembly to decrease the particle size depending on the gas flow, the applied power and the etching time.<sup>[40]</sup> Following a similar approach, ordered arrays of metal nanoparticles can be created by incorporation of metal complexes into the nanoparticles. After size reduction and thermal annealing pure metal nanoparticles remain.<sup>[40]</sup> Here, the monolayers do not serve as templates for metal evaporation-mediated nanostructure formation as it is used in classical nanosphere lithography. The metal is already incorporated in the polymeric matrix<sup>[57, 58]</sup>

using less and cheaper source materials which is cost-saving and straight forward for instance applicable for data storage.

Another possibility for building new, non-conventional symmetries is the template assisted self-assembly of nanoparticles. By manipulating the surface topography of the substrates even common spherical particles can be organized into various interesting microstructures; for instance in lines with controllable line interspacing,<sup>[59-64]</sup> in holes as two-dimensional small, well-ordered clusters depending on the hole and particle size<sup>[60, 65-67]</sup> or on top of pillars.<sup>[56, 68]</sup> Such patterning methods provide the possibility to design future devices with well-defined functional regions with precisely assembled colloids. Also the attractive interaction of positive and negative charges of electrodes and particles can be used for a directed self-assembly as has been shown for instance by Tien *et al.*<sup>[69]</sup> or Fulda *et al.*<sup>[70]</sup> in the late 1990s.<sup>[71]</sup> Beside the physical or mechanical manipulation of the substrate, also chemical modification of either the substrate or the particles can be used to create binding affinity<sup>[72-74]</sup> or special binding patches of the particles on the substrate or between the particles themselves. A famous method for such a directed self-assembly is to employ preferred interactions between special molecules or functional groups such as the chemical modification with DNA strands.<sup>[75-78]</sup> Here, the idea is to functionalize the particles with a special DNA sequence and to modify the substrate with the matching counterpart of the DNA sequence. As the DNA strongly assembles by combining their nucleobases cytosine (C), guanine (G), adenine (A) and thymine (T) by base pairing A and T or C and G over strong hydrogen bonding, the modified particles assemble preferably on the treated patterns of the substrate. But there are rather more possibilities as has also been shown by Wang *et al.*<sup>[79]</sup>, Pine *et al.*<sup>[80]</sup> or Glotzer *et al.*<sup>[74, 81]</sup> to create so-called patchy particles with various heterogeneous surface modification of multiple materials.<sup>[74, 81-83]</sup> The colloidal particles are designed similarly to hybridized atomic orbitals, thus giving access to self-assembly into colloidal molecules of very defined and controllable structures.

## 5. Characterization Techniques

### 5.1. The Langmuir Trough

The preparation of monomolecular layers of amphiphiles floating at the air-water interface is well known from the beginning of the 20<sup>th</sup> century and were first systematically investigated by the Nobel prize winner Irving Langmuir and Katherine Blodgett.<sup>[84, 85]</sup> These films, also known as Langmuir films, mostly consist of amphiphilic molecules with a hydrophilic head group and a hydrophobic tail such as fatty acids, esters or alcohols and are spread in volatile organic solvents directly at the air-water interface. Using a poly(1,1,2,2-tetrafluoroethylene) (PTFE) Langmuir-Blodgett trough equipped with a film balance and with moveable barriers the monomolecular interfacial film can be compressed (Figure 6).

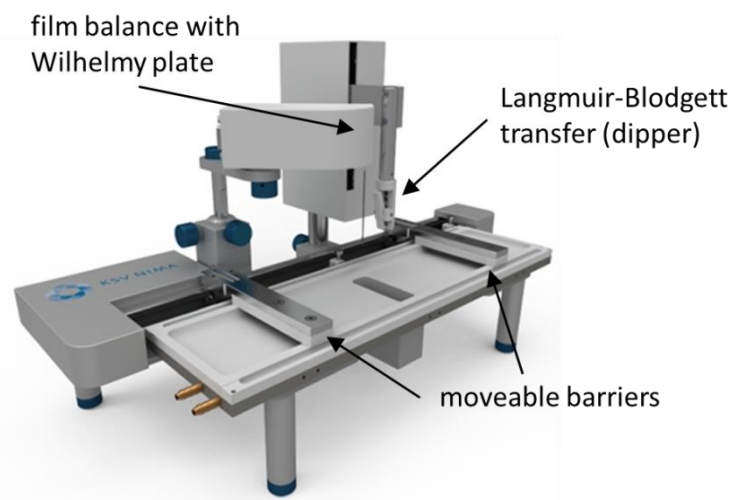


Figure 6 Langmuir trough from KSV Nima equipped with film balance and Wilhelmy plate, moveable barriers and dipper for Langmuir-Blodgett transfer.

Upon compression the molecules are forced to come closer together and interact with each other creating a surface pressure, dedicated as  $\pi$ . This pressure can be measured with the Wilhelmy plate method. Here, a filter paper Wilhelmy plate is partly immersed in the water subphase of the Langmuir trough (Figure 7).

The force difference ( $\Delta F$ ) of an ideal wettable Wilhelmy plate is measured between the pure water interface ( $\vec{F}_0$ ) and the interface which is covered with the amphiphilic monolayer ( $\vec{F}$ ) (eq. 12, 13).

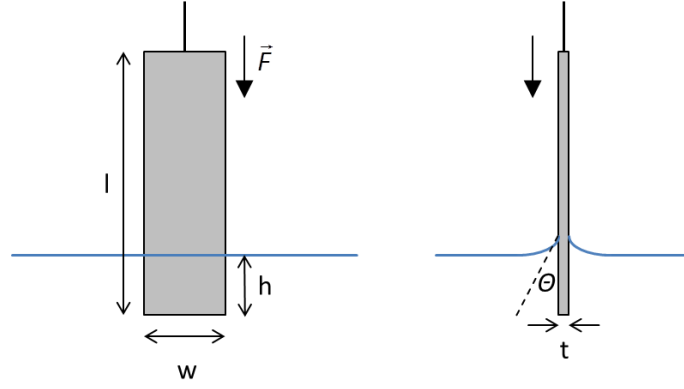


Figure 7 Scheme for a Wilhelmy plate with length  $l$ , width  $w$ , thickness  $t$ , immersion depth into the water subphase  $h$ , contact angle  $\Theta$  and force  $\vec{F}$  acting on the plate that is partly immersed in the water subphase.

$$\vec{F}_0 = \rho_1 g l t + 2\gamma_0 (w + t) \cos \Theta - \rho_2 g h w t \quad (\text{eq. 12})$$

$$\vec{F} = \rho_1 g l t + 2\gamma (w + t) \cos \Theta - \rho_2 g h w t \quad (\text{eq. 13})$$

Here,  $\rho_1$  stands for the density of the Wilhelmy plate,  $\rho_2$  for the density of the subphase,  $g$  stands for the weight,  $l$  for the length,  $t$  for the thickness,  $w$  for the width and  $h$  for the immersion depth of the Wilhelmy plate. Furthermore, the forces are characterized by the interfacial tension of pure water ( $\gamma_0$ ) and the surface covered with a Langmuir film ( $\gamma$ )

Assuming an ideal wettable Wilhelmy plate with a static contact angle of  $\Theta = 0^\circ$  and a constant immersion depth  $h$  the force difference can be calculated as it is shown:

$$\Delta F = \vec{F}_0 - \vec{F} = 2(\gamma_0 - \gamma)(w + t) \quad (\text{eq. 14})$$

The surface pressure ( $\Pi$ ) is defined as the difference between the surface tension of pure water ( $\gamma_0$ ) and the reduced surface tension in the presence of surface active species in the Langmuir film ( $\gamma$ ). The final expression for the surface pressure  $\Pi$  is shown in equation 15:

$$\Pi = \frac{\Delta \vec{F}}{2(w + t)} \quad (\text{eq. 15})$$

During compression  $\Pi$  increases and different phase transition states of the monolayer can be seen from surface pressure-area isotherms as well as the area covered by a single molecule (Figure 8).

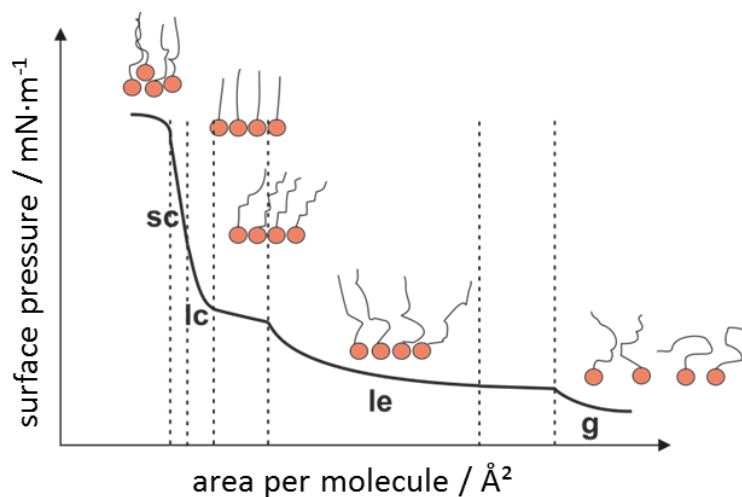


Figure 8 Exemplary surface pressure–area per molecule isotherm for the compression of an amphiphile at the air-water interface of a Langmuir trough with different phase transitions from gaseous (g), to liquid-expanded (le), liquid-condensed (lc) to solid-condensed (sc).

In early compression states the monolayer is characterized by a “gaseous-like” behavior (g). Here, the molecules are randomly distributed on the water subphase not interacting with each other except elastic collision similar as a three-dimensional ideal gas. Further compression leads to an increase in surface pressure and a “liquid-like” behavior where the molecules start to interact with each other and form a close package often called as “liquid-expanded” (le) where the hydrophobic chains stay flexible. When the interfacial film is compressed even further, the hydrophobic chains of the amphiphile start to align; only thermal movement is possible (lc). Once the hydrophobic chains of the molecules are straighten up completely a “solid-like” (sc) interfacial film is formed. If the interfacial film is compressed even further, the monolayer collapses irreversibly and multilayers are formed.<sup>[86, 87]</sup>

Usually, monolayer transfer to solid substrates takes place in the solid-condensed compression state of the interfacial film. There are different possibilities for the monolayer transfer onto solid substrates as it is shown in Figure 9.

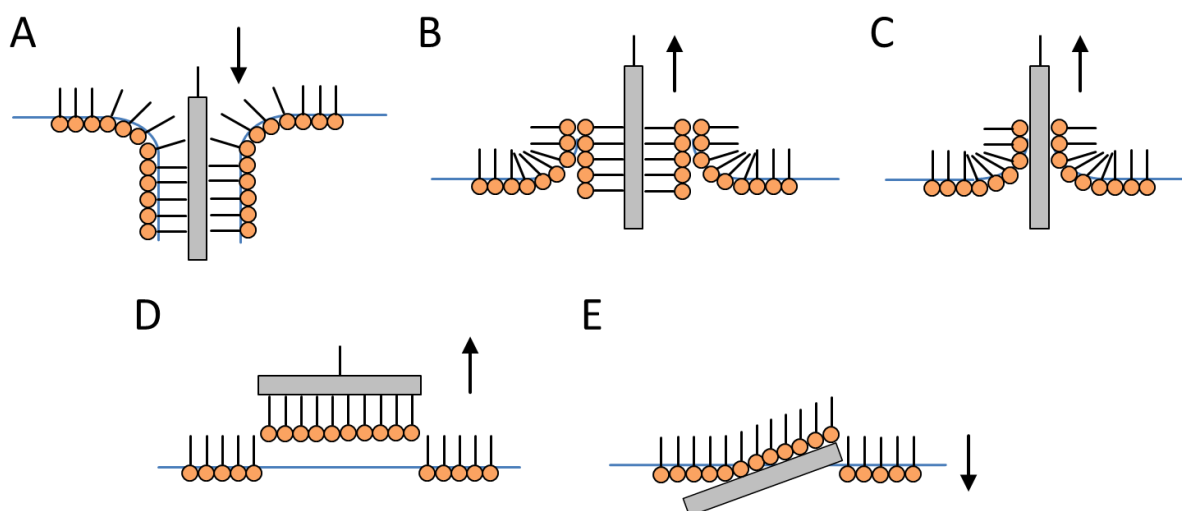


Figure 9 Different deposition methods for amphiphilic molecules self-assembled at the air-water interface of a Langmuir trough, A) Langmuir-Blodgett X-type deposition, B) Y-type deposition, C) Z-type deposition perpendicular to the air-water interface, D) Langmuir-Schaefer transfer parallel to the air-water interface and E) surface lowering transfer.

Different types of monolayer deposition were established using a Langmuir-Blodgett trough with or without a dipper. Hydrophobic substrates are typically transferred with the X-type deposition method. Here, the substrate is lowered into the subphase perpendicular to the air-water interface and covered with a single layer of molecules (Figure 9A). The Y-type deposition method is used for hydrophobic as well as for hydrophilic substrates. Generally, double layers of molecules are created because the substrate is covered during dipping into the subphase as well as during removal of the substrate as can be seen in Figure 9B. If the substrate is already immersed in the water subphase before compression of the interfacial film the transfer method is called the Z-type transfer resulting also a single layer of the film deposited on the substrate (Figure 9C).<sup>[85, 88]</sup> Moreover, the Langmuir-Schaefer transfer can be used for hydrophobic substrates (Figure 9D). Here, the substrate is lowered parallel to the interface and lifted after contact with the interfacial film.<sup>[89, 90]</sup> When working with a Langmuir trough without additional dipping equipment the monolayer can be transferred to a substrate by surface lowering transfer. Here, the interfacial film is lowered onto the solid substrate by careful pumping the subphase behind the barriers (Figure 9E).

This technique is not exclusively suitable for molecular self-assembly at the air-water interface. Also nanoparticles of different materials and shapes can easily be self-assembled

at the air-water interface using the Langmuir trough application. Well-ordered hexagonal arrangements of colloids or other structures can be created and transferred by different deposition methods to substrates of different material and surface texture.

## 5.2. Scanning Electron Microscopy

There are several microscopy techniques to investigate the surface topography of samples such as the common light microscopy, atomic force microscopy and electron microscopy. Modern light microscopes are working with light in the visible wavelength range of the electromagnetic spectrum between 400 and 700 nm. The resolution of light microscopy is defined by Abbe's resolution limit dedicated by the minimal distance ( $d$ ) between two points depending on the numerical aperture ( $NA$ ) and the wavelength ( $\lambda$ ) of the incident light (eq. 16):

$$d = \frac{\lambda}{2NA} \quad (\text{eq. 16})$$

Therefore, the maximum magnification is limited to about 1000x. Electron and scanning probe microscopy are reliable methods used when common light microscopy is inappropriate to image nanometer sized objects.

In scanning electron microscopy<sup>[91]</sup> cathode accelerated electrons are focused by magnetic coils and the resulting electron beam is scanned across the sample's surface. The electrons interact with the atoms in the sample (Figure 10) producing several detectable signals which carry information about composition and the surface topography.

Upon interaction with the electrons from the focused primary electron beam secondary electrons (SE) can be ejected from the sample as they are low energy electrons. These electrons are typically used for surface imaging as they can leave the sample only at very short distances from their place of generation and guarantee high lateral and depth resolution. Moreover, high-energy back-scattered electrons (BE) can appear upon elastic scattering with electrons in the atomic shell.

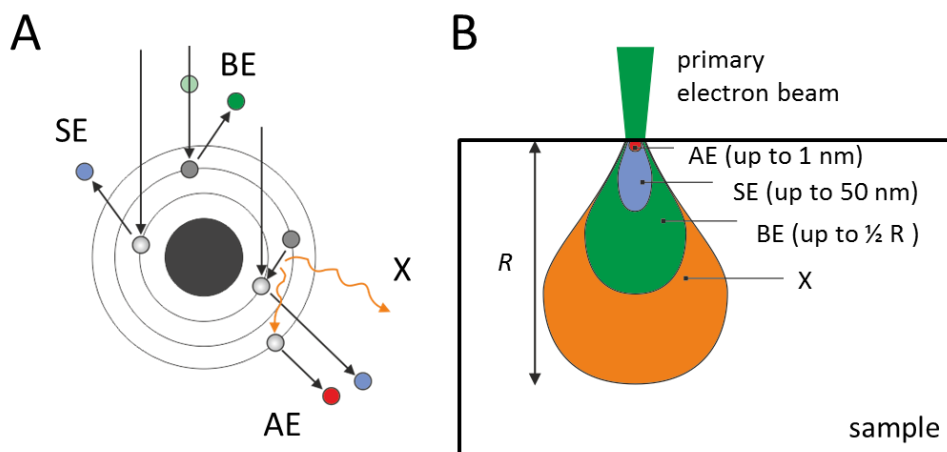


Figure 10 Schematic illustrations of electrons from a focused electron beam of a scanning electron microscope (A) interacting with atoms on the sample surface and (B) the penetration depth ( $R$ ).

As this method is very sensitive to the atomic number material contrasts can be generated and visualized. Elements with high atomic number produce more back-scattered electrons and appear brighter than materials with low atomic number. If an electron from an inner shell of the atom is removed by the beam electrons and the place refilled by an electron from lower energy orbitals, radiation is emitted known as x-rays. This effect is used in energy dispersive x-ray spectroscopy (EDX) for investigations of the crystallographic structure of the material. When the emitted x-ray energy is absorbed by electrons located in outer orbitals which are then ejected, these electrons are called Auger electrons (AE).

### 5.3. Atomic Force Microscopy

Atomic force microscopy (AFM)<sup>[19, 92]</sup> is a type of high-resolution scanning probe microscopy which uses a physical probe, to scan the sample surface. With the so called cantilever consisting of a flat spring and a sharp tip the surface topography of a sample can be imaged following the basic principle shown in Figure 11. A laser beam is focused on the cantilever tip which is reflected to a photodiode detector. The sample is placed on a piezo controlled table and moved line-wise in x- and y-direction underneath the AFM tip. Due to the surface topography of the sample the cantilever is deflected in the z-direction resulting in a shifted,

reflected laser beam on the photodiode detector that is converted into an electrical signal. Using different operation modes, various material types ranging from hard to soft or sticky can be investigated. In the contact mode or static mode, respectively the physical probe touches the specimen's surface directly. Here, the cantilever can either be regulated to scan with constant force across the surface (constant force mode) or it is set to a constant height on the surface (constant height mode) during scanning. This method can only be used for hard materials as the permanent contact of the tip and the high surface pressures may lead to deformation or even damage of the sample. Moreover, there are also dynamic modes such as the non-contact mode and the intermittent mode which are more suitable for soft and sticky surfaces. The cantilever oscillates near its resonance frequency and touches the surface only shortly without permanent contacting the sample surface. The interaction with the interface varying on the properties of the material and upcoming van der Waals, electrostatic or dipole-dipole interactions decreases the vibrational frequency of the cantilever which results in a phase shift. With this technique not only height images of the surface topography can be gained but also information about mechanical and adhesive properties of the material.

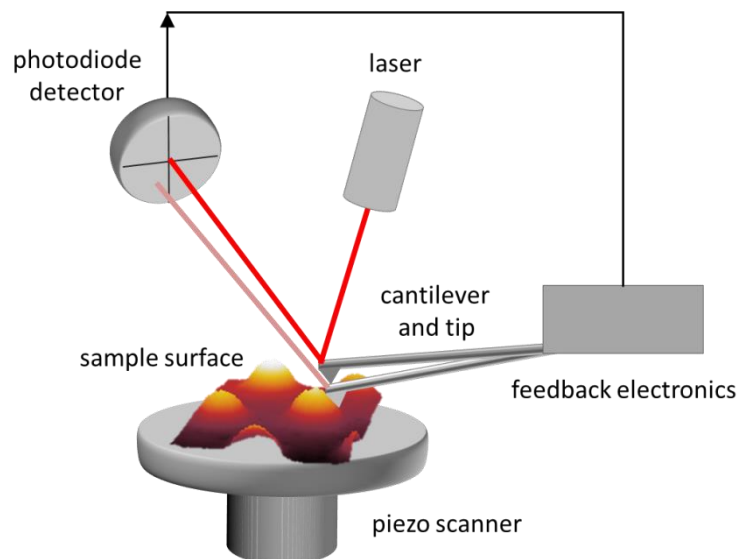


Figure 11 Schematic illustration of an atomic force microscope. A laser beam is focused on the cantilever and reflected to a four quadrant photodiode detector. The deflections of the cantilever, which are caused by the surface topography of the sample result in a deflection of the reflected laser beam on the photodiode detector. With the piezo scanner the sample can be moved laterally and vertically.

## 6. Results and Discussion

The results and discussion chapter is divided into four sub-chapters. The first part (chapter 6.1) investigates colloids and their self-assembled structures concerning their interfacial equilibrium position directly at the air-water interface. A novel gas phase induced interfacial polymerization technique is presented to determine contact angles of individual colloids of different size and composition at aqueous interfaces.

Afterwards, the amphiphile-driven self-assembly of nanoparticles into complex two-dimensional architectures such as chain-like and pseudo square arrangements at the air-water interface of a Langmuir trough is demonstrated (chapter 6.2).

These chapters are followed by the presentation of a model system for optical data storage applications based on a functional binary colloidal monolayer with photo-responsive spatially separated nano-pixels (chapter 6.3).

The last part (chapter 6.4) is based on another fundamental question of how nanoparticles interact with their environment. Here, it is described how stimuli responsive pH-sensitive nanoparticles were functionalized with a pH sensitive dye are used to record the pathway through a cell and the variance of the pH upon different transport processes of the particles inside the cell (chapter 6.4).

### 6.1. Direct Visualization of the Interfacial Position of Colloidal Particles and their Assemblies

This section is partly based on the publication “Direct Visualization of the interfacial position of colloidal particles and their assemblies” by N. Vogel, J. Ally, K. Bley, M. Kappl, K. Landfester and C. K. Weiss published 2014 in *Nanoscale*, volume 6 on pages 6879 – 6885 (Ref. c4nr00401a). The publication is reprinted by permission from The Royal Society of Chemistry.<sup>[93]</sup>

First, the vapor phase induced interfacial polymerization technique is introduced which allows direct visualization of nanoparticles in their equilibrium position at the air-water interface using AFM and SEM techniques. Kinetic studies were done to investigate the film

formation process and to validate that the interfacial positions of the colloids at the interface remain unaffected during the polymerization. The entrapment of different nanoparticles such as soft core-shell or polymeric particles in hexagonal arrangements and the measurement of the contact angles with colloidal probe atomic force microscopy were done by [REDACTED] and [REDACTED]

To investigate and understand colloidal self-assembly at the air-water interface is of major importance even in the description of a variety of everyday problems such as food industries and cosmetics or stain-resistant surfaces<sup>[94]</sup>. Science and technology are reliant on the understanding of how colloids interact at interfaces *e.g.* in drug delivery<sup>[95]</sup>, emulsion stability<sup>[96]</sup>, particles assisted wetting<sup>[97, 98]</sup> and colloidal self-assembly at air-water interfaces.<sup>[99, 100]</sup> The self-organization of colloids at the air-water interface into highly ordered two-dimensional crystals has been recognized as an important and convenient technology to fabricate functional surface patterns at the nanoscale applicable in diverse research fields and technologies such as photonics<sup>[101-103]</sup>, data storage<sup>[103-106]</sup>, control of liquid wetting and repellency<sup>[107-109]</sup>, antireflective coatings<sup>[108, 110]</sup>, plasmonic sensing<sup>[111-113]</sup>, or light management in solar cells.<sup>[114, 115]</sup> Cooperative properties can be induced in single-particle layers by using the advantage of binary colloidal crystals to study the effects of nanoscale confinement<sup>[116, 117]</sup>, to explore complex assembly structures using structured particles<sup>[118]</sup>, or to investigate the behavior of individual colloids at interfaces for a better understanding of fundamental self-ordering processes.<sup>[119]</sup>

Optical microscopy methods are a powerful tool to directly visualize self-organization processes on a single particle level taking place at interfaces<sup>[119, 120]</sup> but it is inherently limited to particles with sizes in the micrometer range and thus not suitable for processes exploiting nanoscale colloids. Another approach uses the electron microscopy imaging technique of particles trapped at the air-water interface after either solidifying the media for instance by gel trapping technique upon addition of polysaccharides<sup>[121]</sup> or jet-freezing an oil/water/particle system and a subsequent freeze-fracture and metal shadowing process.<sup>[122, 123]</sup> Additionally, an experimentally simple, easy to implement, and robust method for the direct visualization of colloids at the air-water interface independent of the size or the material of the colloids is introduced.

This technique for entrapping nanoparticles at their interfacial position at the air-water interface is inspired by the gel trapping technique, established by Paunov<sup>[121, 124, 125]</sup> and the fingerprinting method with cyanoacrylate fuming.<sup>[126]</sup> Nanoparticles floating at the water/air interface can be easily entrapped by interfacial polymerization of butyl cyanoacrylate (BCA), also known as Super Glue<sup>®</sup>, which can be introduced *via* gas phase (Figure 12). This ensures that the interface is not mechanically perturbed. The polymerization is initiated by nucleophiles<sup>[127-129]</sup> (Figure 12E) and proceeds in the presence of water, thus the monomer has to diffuse through the growing polymer membrane. The presence of functional groups on the particle surface such as amino or hydroxyl groups leads to the formation of a thin poly(butyl cyanoacrylate) (PBCA) film as the functional groups also serve as polymerization initiating nucleophiles. In the presence of acids or Lewis acids the polymerization is inhibited.<sup>[128-130]</sup> Therefore, the film thickness of the PBCA-colloid hybrid film can be not only controlled by the amount of BCA supplied *via* the gas phase but also by the pH regulation of the subphase as the addition of base or other nucleophiles accelerates the BCA polymerization, whereas the addition of acid has a retarding effect. The polymerization process can be described as follows. When the butyl cyanoacrylate is evaporated and is in contact with water, the anionic polymerization is initiated for instance by OH<sup>-</sup> ions of the water. Therefore, the polymerization at the interstices of the colloid monolayer at the air-water interface and also the nucleophiles on the particle surface initiate BCA polymerization (Figure 12B and C). Thus, a thin layer is formed covering the water surface and the cap of the particles reaching out of the air-water interface (Figure 12D). From intermittent-contact atomic force microscopy (AFM) both, height images and phase images can be obtained providing an idea of how much of the particles sticks out of the PBCA layer at the air-water level and therefore, also the contact angle can be determined.

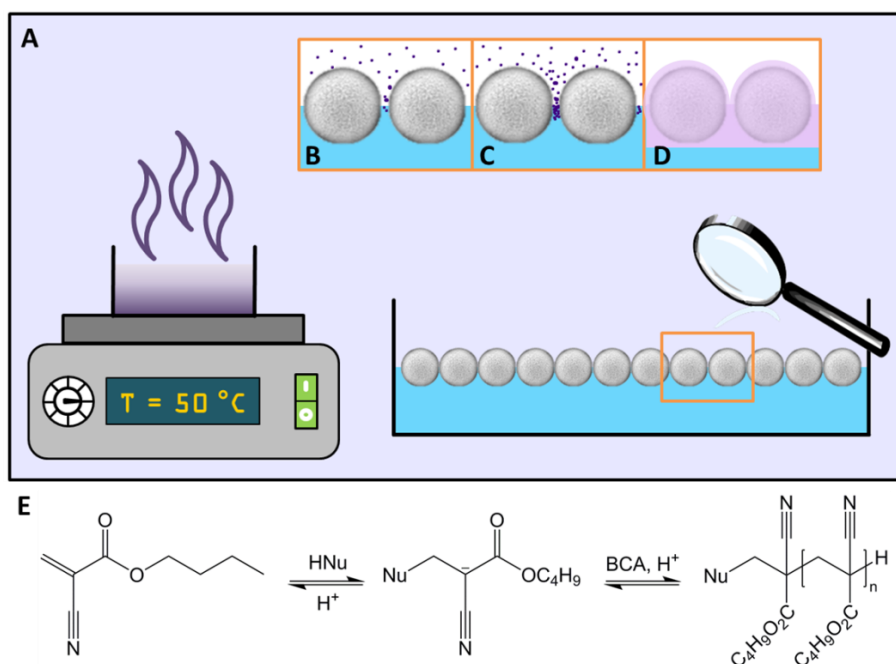


Figure 12 Scheme for the interfacial colloidal entrapping process with gas phase supplied BCA polymerization. (A) Butyl cyanoacrylate is placed in an aluminum dish on a hot-plate. In a crystallization dish the colloids are spread at the air-water interface and both vessels are placed in a closed container. The monomer (BCA) evaporates and polymerizes at the colloid containing air-water interface. (B) The polymerization of BCA is initiated by nucleophiles in the water subphase; a polymer film starts to grow. (C-D) More monomer diffuses through the already formed thin polymeric membrane and polymerization continues until the particles if functional nucleophilic groups are present are fully covered. (E) Reaction scheme of the anionic polymerization of butyl cyanoacrylate initiated by nucleophiles such as OH<sup>-</sup> of the water molecules.

More detailed information about the topography and the surface properties of the film are provided by the phase images. The response time of the oscillating cantilever in interaction with the film surface gives for instance information about the adhesion, friction and elasticity of the film. The response of the cantilevers oscillation while imaging in tapping mode is called “phase”. Figure 13A-B show the height and phase images of a monolayer of plain carboxylated polystyrene spheres ( $D = 1063$  nm) self-assembled at the air-water interface at pH 7.0 and deposited on a Si-wafer. Figure 13C-D present the height and phase images of the colloids embedded in a PBCA layer deposited on Si-wafer after interfacial polymerization with BCA. Compared to the plain monolayer one can clearly see the stiff PBCA layer covering the particles, as the surface of the caps sticking out of the PBCA plane is even rougher and larger agglomerates of PBCA were generated on the surface. The PBCA layer can be clearly seen in the area in between the particles.

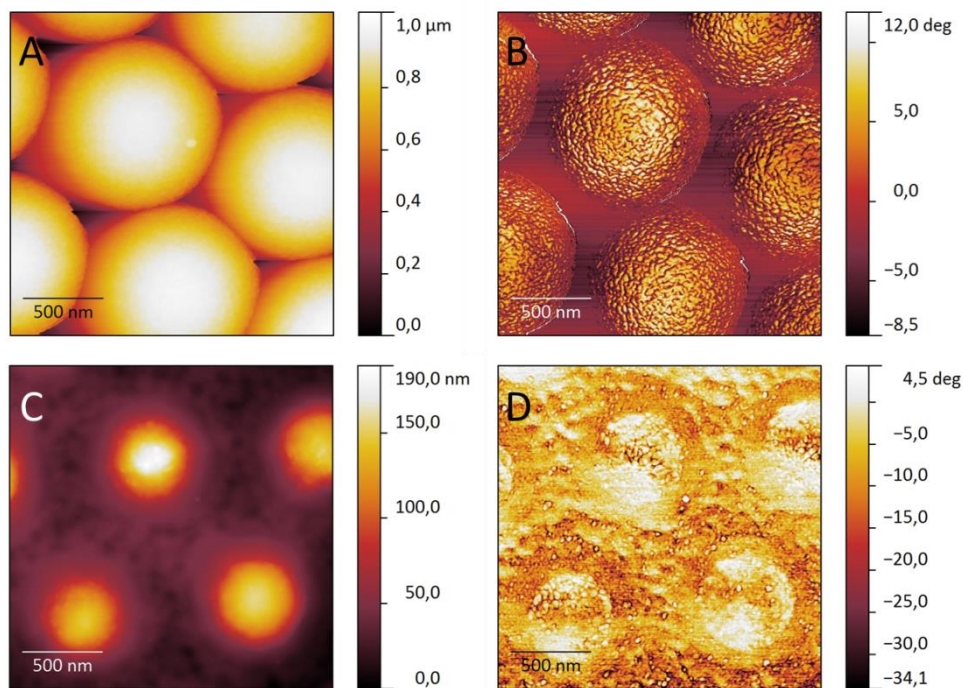


Figure 13 AFM images of polystyrene particles (1063 nm) deposited on silicon wafer after compression of self-assembled monolayers at the water interface of a Langmuir trough. Height image (A) and phase image (B) of colloids not embedded in PBCA. Hybrid film of colloids after interfacial polymerization of BCA (C) shows the height image and (D) the phase image of the hybrid film.

The gradual growth of the PBCA layer can be easily visualized using side view scanning electron micrographs as the polymerization can only proceed in the presence of water, the BCA molecules need to pass the already formed polymeric membrane. This is the reason why the PBCA film only grows into the direction of the subphase (Figure 14A-F). Depending on the amount of BCA added via the gas phase the film thickness can be regulated resulting in partly embedded colloids (Figure 14A-D) or in a hybrid film mostly consisting of PBCA (Figure 14E-F). From the side view scanning electron micrographs it is obvious that the film thickness has no or just minor effects on the contact angle or the particles self-assembled architectures.

The membrane, which is formed, features a smooth interface on the side facing the air phase while being coarser at the growth front directed into the water phase, reflecting individual nucleation and growth sites occurring during the polymerization.

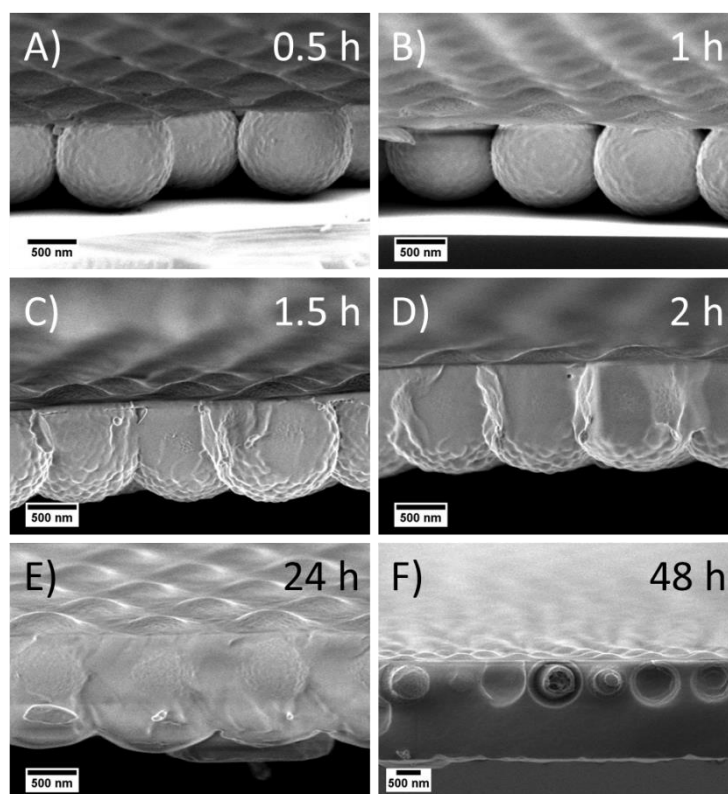


Figure 14 Side view scanning electron microscopy images of polystyrene spheres ( $D = 1063$  nm) in a monolayer embedded in PBCA. The process of PBCA film formation is visualized by SEM from transferred hybrid films after given time intervals of permanent monomer addition *via* the gas phase. The micrographs show the embedded colloidal monolayers after A) 0.5 h, B) 1 h, C) 1.5 h, D) 2 h, E) 24 h and F) after 48 h of monomer exposure. Long exposure times show that the film growth is exclusively into the subphase direction and the colloids' positions at the interface as well as the shape and morphology of the polymer surface remain unaltered by the continuing polymerization reaction.

The hybrid colloid-PBCA films can be easily transferred to a solid substrate and investigated by electron microscopy. Advantageously, this method proceeds without mechanical perturbation of the interface and the necessity of additives present in the subphase which may have an influence on the contact angle of the colloids. Moreover, it provides a possibility to easily visualize self-assembly of colloids at the interface in a current “frozen” state, whereupon mechanical disturbances or drying effects on the self-assembled structures of the colloids during the transfer can be suppressed.

### 6.1.1. The Contact Angle of Nanoparticles in Hexagonal Closed-Packed Arrangements

The process of entrapping colloidal particles at their interfacial position by polymerization of butyl cyanoacrylate is suitable for various materials independently on the particle size as can be seen in Figure 15. Here, hexagonal arrangements of nanoparticles consisting of polystyrene (Figure 15A, 1063 nm), poly(methyl methacrylate) (Figure 15B, 350 nm), silica (Figure 15C, 590 nm) or even very soft and deformable core-shell particles with a gold core and a poly(*N*-isopropylacrylamide) hydrogel shell (Au@PNiPAAm, Figure 15D, 300 nm) were fixed at their interfacial position with this method.

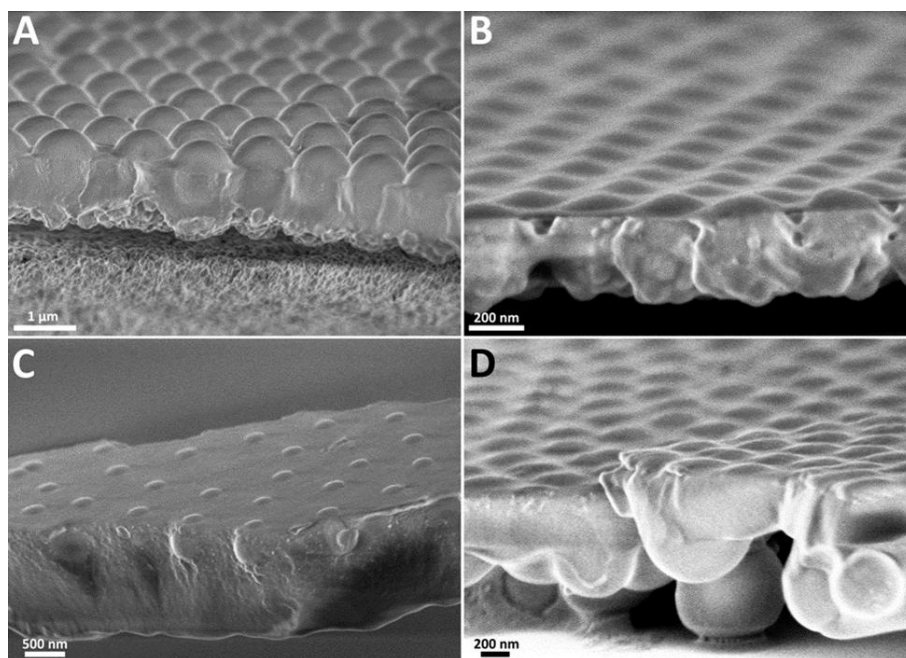


Figure 15 Scanning electron micrographs, side view on colloidal particles of different sizes and materials embedded at their interfacial position with PBCA, (A) polystyrene (1063 nm), (B) poly(methyl methacrylate) (350 nm), (C) silica (590 nm) and Au@PNiPAAm (300 nm). The figure was taken from Vogel *et al.* <sup>[93]</sup> with permission from the Royal Society of Chemistry.

All particles used for entrapment were self-assembled at the air-water interface in a crystallization dish following the procedure described in the experimental details (chapter 7). The particles arrange themselves in a hexagonally closed packed lattice forming 2D-crystalline and very stable structures. The large polystyrene particles (Figure 15A) were self-assembled at pH = 6 and completely embedded in a thick PBCA film. The poly(methyl

methacrylate) (PMMA) colloids where fixed with a very thin film of about 20 nm of PBCA (Figure 15B). The silica particles (Figure 15C) show a very small water contact angle which is caused by the high hydrophilicity of the particles due to the presence of a high amount of hydroxyl groups on the particles surface. Further, the silica particles did not form a densely packed hexagonal structure, but voids and packing defects are visible in the monolayer. This indicates that by introduction of the BCA monomer to the interface and the interfacial polymerization the colloids are not forced to form a hexagonal close-packed arrangement and induce colloid crystallization. It rather allows the visualization of the current situation or process with no or minor disturbances. Such a “frozen” state as snap-shot is getting more important for the creation of more complex hierarchical colloid arrangements, which are thermodynamically not favored such as square and chain-like arrangements, which is described in chapter 6.2. It provides a more accurate picture of colloidal self-assembly processes as systematic errors arising from transfer and drying can be excluded.

The contact angle of the colloids can be determined from scanning electron micrographs by two techniques. First, appropriate tangents can be fitted in the side view images and the angle is extracted from the image. But the evaluation of a statistically relevant number of nanoparticles is exhausting as only few particles are located on the edge of the film. The second method provides more proper statistical evaluation by investigating top-view images of the PBCA-colloid hybrid films. The contact angle can be analyzed with the software ImageJ and the aid of a geometric model (Figure 16).

After measuring the diameter of the nanoparticles cap protruding from the polymeric film equation 17 can be used to calculate the contact angle.

$$\Theta = 90^\circ - \arccos\left(\frac{r_{top} - d_{PBCA}}{r}\right) \quad (\text{eq. 17})$$

The colloids are covered with a thin PBCA layer which needs to be considered in the geometric model. From side view images the thickness of this layer was estimated to be approximately  $d_{PBCA} = 200$  nm. The diameter obtained from the top view images was corrected by this value ( $d_{PBCA}$ ).

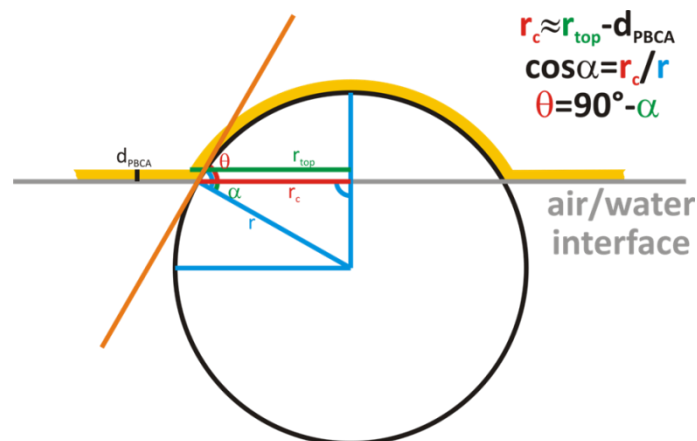


Figure 16 Sketch of a colloid at the air-water interface and the derivation of the equation to assess the contact angle from top-view diameters.  $r_c$ : radius of the colloid caps ( $r_{top}$ ) corrected by the thickness of the PBCA layer ( $d_{PBCA} = 200$  nm). The image is reprinted with permission from the Royal Society of Chemistry.<sup>[93]</sup>

To assess the capabilities of the proposed method and to extract quantitative information, the contact angle of carboxylic acid functionalized PS particles was determined at different pH values and compared to results obtained by colloidal probe atomic force microscopy realized by J. Ally as alternative method. For this method a single colloidal particle is glued to the end of a tipless AFM cantilever and particle interactions with a surface or interface can be studied in detail.<sup>[131, 132]</sup> From force measurements the contact angle can be determined as the particle is brought into contact with a fluid-liquid interface.<sup>[133]</sup> This method is limited to colloids of sizes larger than 3  $\mu\text{m}$ . For the assembly of colloidal probes the particles must be manipulated under an optical microscope which is not possible using smaller particles. The interfacial visualization with PBCA hybrid films is not limited to micron sized particles but could equally be used to investigate and quantify contact angles of smaller, nano-scaled colloids. For this reason commercially available, carboxylated PS colloids with a nominal diameter of 5  $\mu\text{m}$  were chosen for comparative evaluation using the colloidal probe AFM technique. The results of the air-water-colloid contact angle by both the established colloidal probe AFM and the interfacial polymerization visualization method are summarized in Table 1.

The 5  $\mu\text{m}$  PS colloids used for the experiments have a carboxylated surface, thus the surface charge and hydrophilicity can be adjusted by the pH of the subphase. At low pH, the particles are relatively hydrophobic as the surface charge is reduced by protonation of the carboxylic acid functions.<sup>[56]</sup> In contrast, at high pH values the carboxylic acid is

deprotonated which leads to a higher amount of surface charges and increased hydrophilicity of the colloids. The submersion depth of the colloids is directly related to the charge on the particle surface and therefore also to the hydrophobicity. A lower hydrophilicity leads to decreased contact angles and higher hydrophobicity to increased contact angles of the particles at the air-water interface vice versa. Poly(acrylic acid), serving as reference for the surface bound carboxylic acid groups, has  $pK_a = 4 - 4.5$ <sup>[134]</sup>, so the transition from fully protonated acid function to deprotonated acid should appear between pH = 4 and pH = 5. Thus the colloids were investigated at pH = 4, pH = 6 and pH = 9. In basic conditions the contact angle should be significantly lower, as the majority of the acidic groups are deprotonated and therefore, the hydrophobicity should be decreased.

Table 1 Contact angles obtained from atomic force microscopy (AFM) measurements and the visual evaluation of scanning electron micrographs of interfacial trapped colloids.

<b>Contact angle <math>\theta</math> / °</b>					
<b>pH</b>	<b>Charge density</b>	<b>AFM: advancing</b>	<b>AFM: receding</b>	<b>Visual: side</b>	<b>Visual: top</b>
<b>4</b>	1.4	23.1, 45.9, 44.6	19.6	35	40 ± 7
<b>6</b>	2.1	17.7, 40.4, 40.6	14.2	30	26 ± 4
<b>9</b>	2.9	13.5, 38.9, 40.5	10.9	20	23 ± 5

As the results show, there are large variations in the contact angles obtained by the individual colloidal force measurements. One set of measurements gave quite low values (13.5 to 23.1°) with a difference of ca. 10° between pH 4 and pH 9, whereas the other measurements result a contact angle of approximately 40° with only small differences among pH values, Determining contact angles via embedding the particles in a solid polymer film and subsequent SEM image analysis yields more statistically relevant data since a large number of colloids can be assessed with ease. A significant distribution of the values of the contact angles corroborating the large scatter in colloidal force data. The values of the contact angles range from 28 to 48° at pH 4, from 18 to 32° at pH 6 and from 13 to 26° at pH 9. In comparison to the standard deviation of the colloids used within the experiment ( $D = 4890 \pm 97$  nm), the distribution cannot only be explained by the variation of the particles diameter. The results support the recent findings of Isa *et al.*<sup>[122]</sup>, who reported a

distinct distribution of contact angles of colloids trapped at an oil-water interface. This single particle approach showed that colloids do not only feature a size distribution but also differ significantly in their surface properties. The origin of these inhomogeneous surface properties is not yet completely understood. It has been proposed that possibly a surficial or topographic inhomogeneity can arise from synthetic process or particle treatment such as washing, centrifugation or the addition of spreading solvent.<sup>[135, 136]</sup> Moreover, fluctuation of contact position can be founded on Brownian motion, which is potentially resolved when visualizing individual particles.<sup>[122]</sup>

### **6.1.2. Conclusion and Outlook for Section 6.1**

To summarize, an experimentally simple, fast and versatile technique was presented to trap colloids of a wide size range and arbitrary composition at the air-water interface by embedding them in a poly(butyl cyanoacrylate) film. Interface and position of the colloids remain unaffected as the monomer is introduced *via* the gas phase and polymerizes upon contact with the aqueous subphase. Thus, the method enables visualizing colloids of a variety of materials and sizes, including polymer and inorganic materials as well as very soft materials at their equilibrium position directly at the air-water interface. Quantitatively, this technique can be used to determine contact angles of individual particles at liquid interfaces revealing a contact angle distribution what has also been shown by Isa *et al.*<sup>[122]</sup> for particles at liquid-oil interfaces. Furthermore, this technique allows entrapping non-equilibrium particle arrangements directly at the interface and can be used to take a snap-shot of particle arrangements at any stage of the self-assembly process.

## 6.2. Architecture control in Two-Dimensional Colloidal Self-Assembly at the Air-Water Interface

In the previous chapter the interfacial equilibrium position of colloids at the air-water interface was investigated using the gas phase induced polymerization technique. This technique enables to visualize nanoparticles and self-assembled colloidal monolayers directly at the air-water interface. Typically, the interfacial self-assembly of colloids results hexagonal close-packed colloidal monolayers which is the thermodynamically favored structure. In this chapter the amphiphile-driven self-assembly of nanoparticles into network and pseudo square structures is introduced. The amphiphiles force the colloids to assemble into non-equilibrium arrangements. The influence of amphiphile concentration, electrostatic shielding by pH variation and salt addition are investigated in detail.

Creating hexagonal densely packed colloidal monolayers of high quality is well investigated and well established. Several methods can be used to achieve large two-dimensional colloidal crystals. But the controlled preparation of more complex structures such as square or chain-like architectures was so far not possible by only using the colloidal self-assembly without any additional equipment or templates. Such unconventional colloidal architectures, often called anisotropic<sup>[137]</sup> or meso-structures<sup>[138]</sup>, were rather produced randomly than really in a controllable and defined way. Simulations and experiments have predicted that polymer grafted nanoparticles can easily form such anisotropic structures in bulk in the presence of a polymer matrix<sup>[137]</sup> or in thin films.<sup>[139]</sup> But the controllable two-dimensional self-assembly at the air-water interface is so far not accessible. Ghezzi *et al.*<sup>[138, 140]</sup> discovered that sulfate functionalized polystyrene particles spontaneously form complex ring structures, loops or lattice-like architectures at the air-water interface. Chen *et al.*<sup>[141]</sup> and Fernández-Toledano *et al.*<sup>[142]</sup> observed similar loosely bound ordered aggregates, chains and loops of similar particles at the air-water interface. Both groups propose the existence of a second minimum in the interaction potential between approaching colloids, whereupon the particles are energetically trapped. Stamou *et al.*<sup>[27]</sup> propose prevailing long-ranged attractive capillary forces driving the particles to come closer together due to the presence of an irregular meniscus of non-uniformly wetted colloids at the air-water interface. However, Fernández-Toledo *et al.*<sup>[142]</sup> discovered that the formation of meso-structures is caused due to the contamination of colloidal monolayers by silicone oil.

Poly(dimethylsiloxane) oils are often used as coatings for needles and syringes used to spread the particle dispersion at the air–water interface. As this simple example shows, contaminations in colloidal dispersion can have an immense effect on the colloidal monolayer formation. Therefore, proper preparation of the colloid dispersion is of major importance if well-ordered hexagonal densely-packed colloidal monolayers shall be formed. Besides working with clean contaminant-free equipment, the cleaning of the nanoparticle dispersion is also very important. The procedure typically includes several steps such as dialyzing, washing and centrifugation-redispersion cycles to remove additives, stabilizers or monomer residues in the dispersion that can hinder the colloids at the air-water interface to crystallize in well-defined hexagonal arrangements. In the present system, the only “additives” or interfering molecules in the colloid dispersion are undefined low molecular weight copolymers, which are produced *in situ* during the emulsion copolymerization of styrene with acrylic acid.<sup>[21, 143, 144]</sup> In the first step of a radical polymerization process in emulsion, the initiator (a peroxodisulfate) is thermally cleaved forming radicals. A radical reacts with acrylic acid and to a lower extent with styrene molecules present in low concentration in the aqueous dispersive medium. The polymerization of such water soluble oligo-radicals proceeds until a distinct molecular weight is achieved, typically 5-7 monomer units for polystyrene.<sup>[145]</sup> These amphiphilic oligo-radicals start to precipitate and form small agglomerates or micelles serving as nucleation sites for polymerization, respectively. Further, styrene molecules diffuse into the micelles and continue the polymerization until the monomer is completely consumed.

Hexagonal densely-packed crystals of as prepared colloidal particles can be generated at the air-water interface of the Langmuir trough but the presence of the amphiphilic copolymers influences the interaction of colloidal particles and hinders the perfect particle arrangement. Even when the colloidal dispersion has been dialyzed and washed extensively, equilibrium is established due to a concentration gradient of adsorbed low molecular weight species on the colloid surface and free molecules in the continuous aqueous phase.

Figure 17 shows the surface pressure ( $\Pi$ ) vs. area ( $A$ ) isotherms of colloidal dispersions spread and compressed at the air-water interface of a Langmuir trough after given equilibration times. Here, a particle dispersion ( $D = 1150$  nm,  $c = 5$  mg·mL) was left for equilibration in MilliQ water after dialyzing and several washing steps and was spread at the

air-water interface after given time intervals (1 h, 24 h equilibration time in MilliQ water). The surface pressure–area isotherm for a clean colloid dispersion spread at the air-water interface instantaneously after cleaning (compact line) shows the typical steep curve. Already after an equilibration time of 1 h, the shape of the isotherm has changed. This can easily be seen from the shallow part of the isotherm (dashed line) between  $\Pi = 3.3 \text{ mN}\cdot\text{m}^{-1}$  and  $\Pi = 11.7 \text{ mN}\cdot\text{m}^{-1}$  ( $\Delta\Pi = 8.4 \text{ mN}\cdot\text{m}^{-1}$ ) and an area of  $1520 \text{ mm}^2$ .

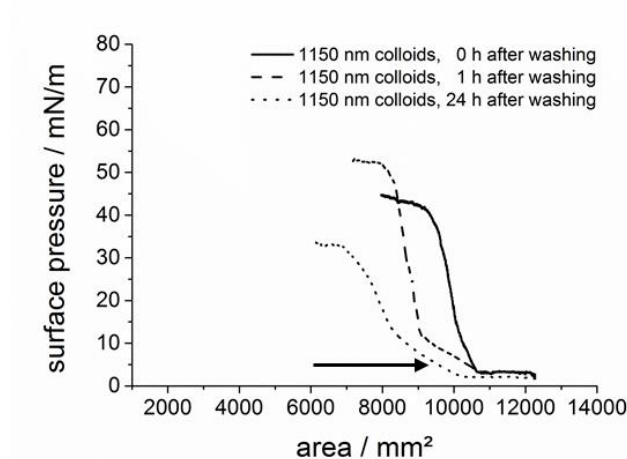


Figure 17 Surface pressure–area isotherms of 1150 nm carboxylated polystyrene colloids. Colloids spread instantaneously after several washing steps (black compact line), after 1 h of equilibration in MilliQ water (black long dashed line) and after 24 h of equilibration in water (black short dashed line) at pH = 7.

During 1 h the above mentioned low molecular weight amphiphilic copolymers desorb from the particle surface due to the depletion of stabilizing molecules in the surrounding medium after washing. After 24 h of equilibration (dotted line) the shallow part of the isotherm is even larger  $\Delta\Pi = 10.1 \text{ mN}\cdot\text{m}^{-1}$  and  $1890 \text{ mm}^2$  in size. This equates to 52.9% of the interfacial area after 1 h and 53.4% after 24 h of equilibration. The isotherm recorded after 24 h of equilibration time indicates the presence of a more flexible film rather than the typical stiff colloid film. From scanning electron microscopy imaging non-hexagonal arrangements can be seen very often if the isotherm for the compression of such a flexible interfacial film looks similar as shown in Figure 17. Mainly additional interactions of desorbed molecules and colloids are responsible for the formation of anisotropic non-hexagonal structures. But these structures are produced more “accidentally” and in a rather uncontrollable way.

Here, the interactions of colloids and distinct, well-defined copolymers or amphiphilic molecules in general might be used to create such structures from colloidal particles without using templates or other time or cost consuming methods. Without any additional equipment or functionalization of the particles as mentioned earlier more complex colloidal structures can be prepared by a self-assembly process in a reproducible and controlled way.

### **6.2.1.1. Amphiphilic Copolymers and their Effect on Colloidal Self-Assembly**

Amphiphilic molecules in general are molecules with both hydrophobic and hydrophilic properties. The most common representatives of amphiphiles are surfactants, which tend to segregate at the air-water interface and alter surface properties. They consist of a hydrophobic part that mostly contains long hydrocarbon chains and a polar hydrophilic part. There are several surfactants with ionic groups such as the negatively charged sodium dodecylsulfate (SDS) or the positively charged cetyltrimethyl ammonium bromide (CTAB) and also non-ionic surfactants such as poly(ethylene oxide) alkyl ether (Lutensol) or polyglycerol polyricinoleate (PGPR).

Using additives such as surfactants influences the properties of the air-water interface and consequently the self-assembly process of colloids by additional steric and electrostatic interactions. As the self-assembly process proceeds at the air-water interface and not in bulk, the detailed analysis of all influencing factors is very challenging. In bulk typically the DLVO theory (chapter 4.1.3) gives an explicit representation of the interplay of van-der-Waals attraction and electrostatic repulsion. Working at the air-water interface on a Langmuir trough causes a far more complex situation, as additional forces such as attractive capillary forces and dipole-dipole interactions appear. Mechanical compression of the colloids and amphiphiles at the interface interferes with the equilibrium situation and forces the components to new (non) equilibrium positions.

Amphiphiles and colloids are both located at the air-water interface. If particles and amphiphiles are both similarly charged the electrostatic repulsion during the compression can be theoretically increased depending on the amount of amphiphiles added as well as the

charge density of the molecules. Hydrophobic attractive interactions can also be increased as well as steric repulsive interactions. Figure 18A shows a scheme for the concept of how particle block-copolymer mixtures can assemble on the surface of a Langmuir trough and the resulting architectures, which were obtained throughout the experiments varying from square (Figure 18B) to chain-like particle assemblies (Figure 18C). Here, depending on the copolymer composition and the concentration of the amphiphile present at the interface, different structures are accessible after compression of the interfacial film.

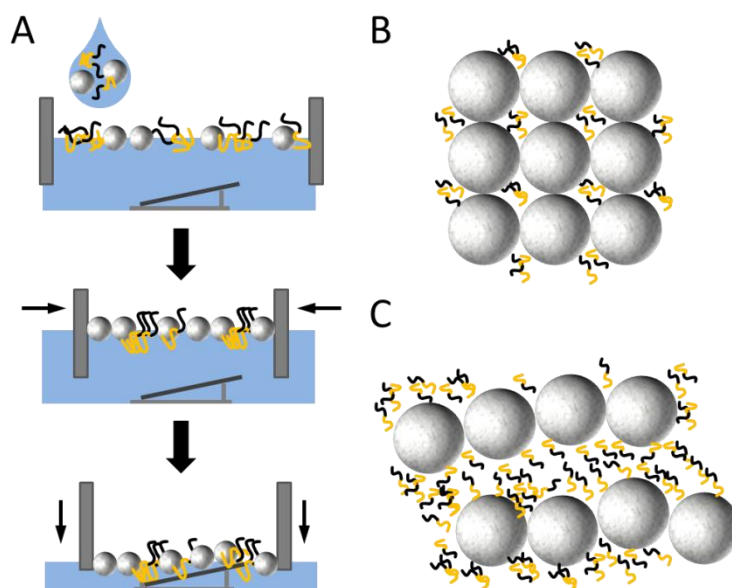


Figure 18 A) Scheme for the preparation of colloid-copolymer hybrid monolayers at the air-water interface of a Langmuir trough starting with spreading, followed by compression and surface lowering transfer (from top to bottom). B and C represent the resulting particle structures such as square (B) and chain-like arrangements (C) that were created by co-self-assembly of colloids and block-copolymers.

As mentioned before, there are different types of surfactants, which can be used to control the particle self-assembly at the air-water interface. Reynaert *et al.* [135, 146] have demonstrated at a decane-water interface of a Langmuir trough that the addition of sodium dodecyl sulfate into the water subphase drives 3  $\mu\text{m}$  sulfate functionalized particles into chain-like aggregates. Different results can be obtained at the air-water interface as Vogel *et al.* [40] have discovered for instance. The presence of negatively charged SDS molecules supports the two-dimensional crystallization process of negatively charged carboxyl functionalized polystyrene particles at the air-water interface creating well-ordered

hexagonal densely-packed monolayers. Figure 19 illustrates the difference in the surface-pressure isothermes for colloids ( $D = 1150$  nm carboxylated PS colloids) spread at the air-water interface and colloids spread onto SDS solution ( $c_{SDS} = 0.1$  mmol·L<sup>-1</sup>) using the Langmuir technique to create closed packed colloidal monolayers. As can be concluded from Figure 19A the surface pressure-area isotherm of the monolayer is much steeper in the presence of SDS (grey compact line), whereas the isotherm from pure MilliQ water (black compact line) shows a more shallow increase in surface pressure during compression indicating the presence of a more flexible film at the air-water interface. The corresponding SEM images of the deposited colloidal monolayers on silica wafers (Figure 19B and C) show as well the difference in packing quality of the colloidal monolayers. The structural unity of the colloids and the two-dimensional hexagonal densely-packed crystal domain size is increased in the presence of SDS.

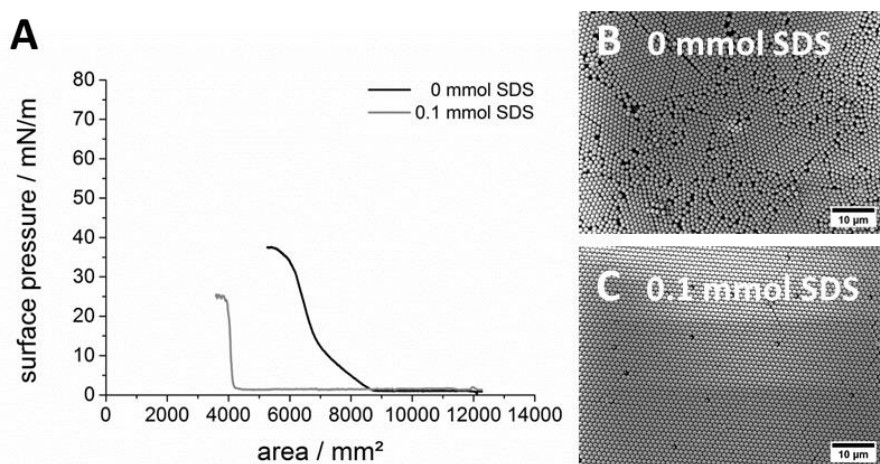


Figure 19 A) Surface pressure – area isotherms of carboxylated polystyrene colloids (1150 nm,  $c = 5$  mg·mL<sup>-1</sup>) with (grey compact line) and without (black compact line) the addition of 0.1 mmol·L<sup>-1</sup> SDS in the subphase and B,C) the corresponding SEM images of the resulting monolayers after deposition.

Obviously, low molecular weight ( $M$ ) molecules, especially amphiphiles such as SDS ( $M = 288.4$  g·mol<sup>-1</sup>) interact with the colloidal particles and influence their structure formation at the interface. They alter the surface tension and affect the electrostatic and steric interactions. However, the formation of more complex architectures such as square crystals or particle chain-like networks cannot be obtained in the presence of such low

molecular weight amphiphiles, at least not in the system used here. Contrary to the results of Reynaert *et al.* at an oil-water interface using negatively charged sulfate functionalized polystyrene particles<sup>[135, 146]</sup>, the addition of SDS does not lead to chain-like aggregates of negatively charged carboxylated polystyrene colloids at the air-water interface. For this reason, other surface active agents with higher molecular weight were tested for their activity at the interface and their interaction with colloids at the air-water interface. As an example for additional mainly steric repulsion between the particles the triblock-copolymer Pluronic P103 was chosen. Further, poly(acrylic acid)-poly(methyl methacrylate) diblock-copolymers were used to manipulate also the electrostatic interactions additional to the steric interactions between the colloids at the air-water interface. First, the interfacial activity of the molecules was investigated using the Langmuir technique. Figure 20A shows the structures of the amphiphilic molecules chosen for architecture control.

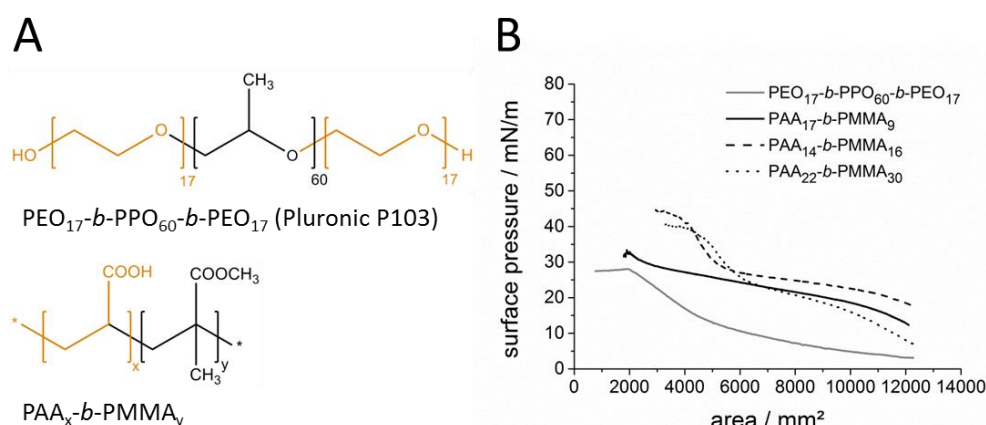


Figure 20 A) Molecular structure of the triblock-copolymer Pluronic P103 and the diblock-copolymer consisting of poly(acrylic acid) and poly(methyl methacrylate). The hydrophilic part is highlighted in orange color and the hydrophobic part in black. B) Shows the surface pressure – area isotherms of the different molecules (Pluronic P103 grey, PAA<sub>17</sub>-b-PMMA<sub>9</sub> compact black, PAA<sub>14</sub>-b-PMMA<sub>16</sub> black dashed, PAA<sub>22</sub>-b-PMMA<sub>30</sub> black dotted line) at the air-water interface at pH = 7.

The commercial non-ionic triblock-copolymer Pluronic P103 consisting of hydrophilic poly(ethylene oxide) (Figure 20A in orange) and poly(propylene oxide) blocks (Figure 20A in black) was used as it is well-known for its high surface activity<sup>[147-149]</sup> and as an example for predominating mechanical or steric interactions between the particles and the surfactant at

the air-water interface. Zhou *et al.*<sup>[150]</sup> discovered that the addition of triblock-copolymers consisting of poly(ethylene oxide) and poly(propylene oxide) blocks forces silica particles in bulk to form chains and networks depending on the concentration of the block-copolymer added. But also Wang *et al.*<sup>[151]</sup> have shown for titanium oxide nanoparticles an anisotropic self-assembly in aqueous phase by adding the triblock-copolymer Pluronic F127 (PEO<sub>100</sub>-*b*-PPO<sub>65</sub>-*b*-PEO<sub>100</sub>), which is promising for the self-assembly at the interface. The surfactant was spread at the air-water interface of a Langmuir trough and surface pressure *versus* area isotherms were recorded during compression of the interface. As can be seen in Figure 20B (grey compact line) the Pluronic P103 monolayer shows a very shallow increase in surface pressure with decreasing available area. This interfacial behavior is typical for flexible molecules at the air-water interface such as stearic acid or oleic acid.<sup>[89, 152-154]</sup> In early compression states the molecules are completely free without contact to each other. This can be described as “gaseous-like” state. When the monolayer is compressed further the molecules start to interact with each other, which is represented by a small increase in surface pressure and the situation can be described as “liquid-like”. The hydrophobic chains start to reorient at the interface. The surface pressure-area isotherm of amphiphiles, such as fatty acid salts, shows a steep part of the isotherm at low area per molecule. This represents a completely covered interface and a stiff film with aligned molecules that cannot be compressed further. This part is not observed in the compression isotherm of Pluronic P103.

Anionic block-copolymers consisting of a hydrophilic poly(acrylic acid) (Figure 20A in orange) and a hydrophobic poly(methyl methacrylate) block (Figure 20A in black) were used<sup>[155, 156]</sup> as they should not only show mechanical interactions but additional electrostatic forces between the colloids at the air-water interface. Here, different low molecular weight copolymers (ca. 1,200-5,000 g·mol<sup>-1</sup>) with varying block lengths were chosen to influence colloidal self-assembly. The block-copolymers used have either an excess of the hydrophilic block (PAA<sub>17</sub>-*b*-PMMA<sub>9</sub>, 1,200 g·mol<sup>-1</sup>), a similar length for both hydrophilic as well as hydrophobic blocks (PAA<sub>14</sub>-*b*-PMMA<sub>16</sub>, 3,000 g·mol<sup>-1</sup>) and or an excess of the hydrophobic block (PAA<sub>22</sub>-*b*-PMMA<sub>30</sub>, 5,000 g·mol<sup>-1</sup>). The concentration of the block-copolymer solutions spread as a 50 vol.% solution at the air-water interface (pH = 7) was  $c = 0.1 \text{ mg}\cdot\text{mL}^{-1}$  for the Pluronic P103 and  $c = 2.5 \text{ mg}\cdot\text{mL}^{-1}$  for the PAA<sub>*x*</sub>-*b*-PMMA<sub>*y*</sub> copolymers. The isotherms for all the block-copolymers are characterized by a very shallow increase of the surface pressure

during compression (Figure 20). The Pluronic P103 surface pressure-area isotherm increases slightly with decreasing area and shows no steep part for a stiff film as it is widely known for amphiphiles. The isotherm of the block-copolymer PAA<sub>17</sub>-*b*-PMMA<sub>9</sub> (Figure 20 black compact line) is characterized mainly by a very slight increase in surface pressure during compression, which is reasonable. The swollen hydrophilic PAA block points into the subphase as water is a better solvent than the air-phase. The PMMA block probably exists as a collapsed coil and stays as hydrophobic block of the copolymer at the air-water interface. But the biggest part of this copolymer is located inside the water subphase. When the interface is completely covered with a molecular monolayer the hydrophobic chains reaching out of the water surface reorient and straighten up upon further compression. Low molecular weight copolymers such as PAA<sub>17</sub>-*b*-PMMA<sub>9</sub> have a too short hydrophobic chain with only 9 methyl methacrylate units to interfere with other surrounding alkyl chains which in general lead to an increased surface pressure.<sup>[152]</sup> The surface pressure isotherm of the block-copolymer PAA<sub>14</sub>-*b*-PMMA<sub>16</sub> (Figure 20B, black dashed line) shows again the slight increase in surface pressure upon compression until the surface is completely covered. The sharp increase in surface pressure indicates the presence of a stiff film where the alkyl chains of the block-copolymer reaching out of the subphase straighten up. Similar behavior is observed for the block-copolymer PAA<sub>22</sub>-*b*-PMMA<sub>30</sub> (Figure 20B, black dotted line) which is characterized by a larger hydrophobic block length and higher molecular weight. The surface pressure - area isotherms presented in Figure 20 (black compact, striped and dotted lines) indicate that the block-copolymers PAA<sub>*x*</sub>-*b*-PMMA<sub>*y*</sub> act in a similar way as the non-ionic Pluronic P103 at the air-water interface except the steeper part of the isotherm at late compression states which can be identified as the region where the hydrophobic PMMA blocks noticeably interact sterically with each other. As can be seen from Figure 20B for the copolymers with a larger hydrophobic block such as PAA<sub>22</sub>-*b*-PMMA<sub>30</sub> the steep region of the isotherm is more pronounced than for the PAA<sub>17</sub>-*b*-PMMA<sub>9</sub>.

After characterizing the interfacial behavior of the copolymers the interaction of copolymer and colloids was analyzed in detail. Therefore, colloid-copolymer mixtures with different copolymer concentrations and 1150 nm carboxyl functionalized polystyrene spheres were spread at the air-water interface as a 67 vol.% ethanolic dispersion. Figure 21A-G present the  $\Pi$ -*A* isotherms of the 1150 nm colloid-Pluronic P103 mixture with different Pluronic P103

concentrations (Figure 21A) and the corresponding SEM images of the monolayers deposited on silica wafers at high surface pressures near the collapse points (Figure 21B-G).

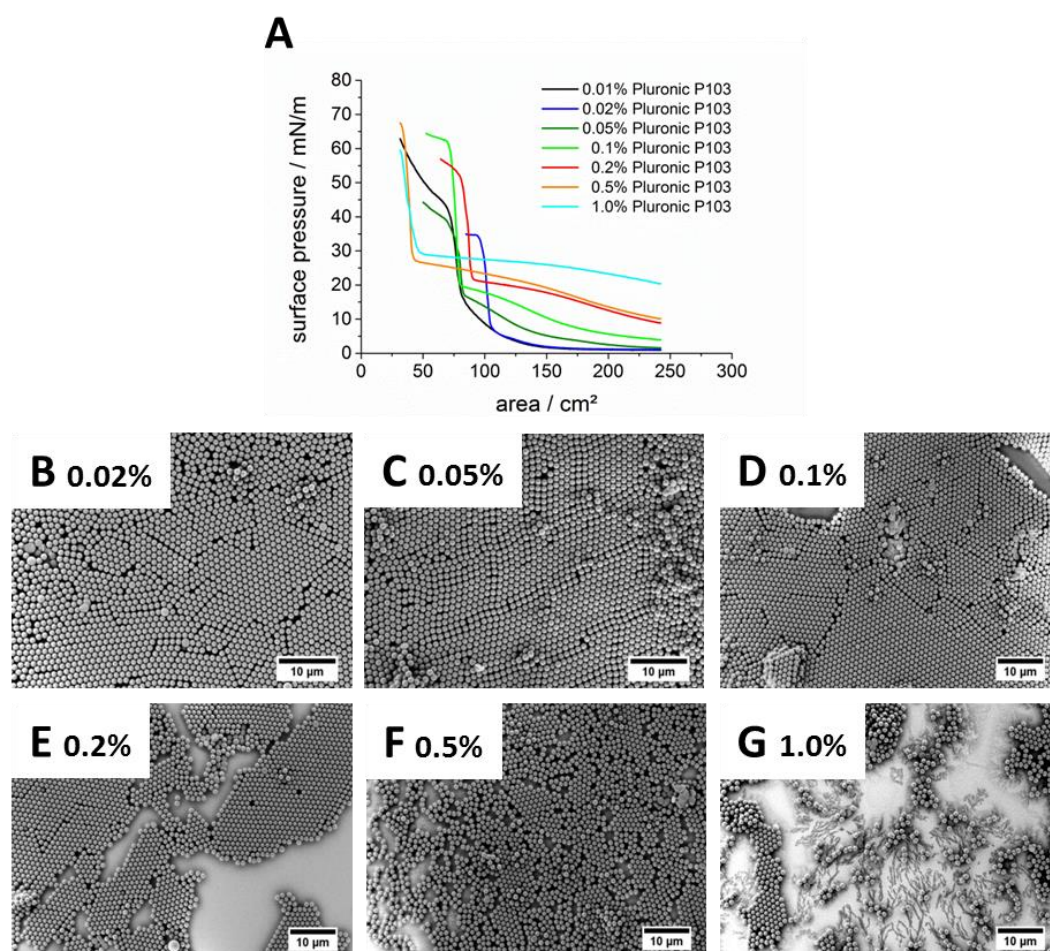


Figure 21 A) Surface pressure – area isotherms of 1150 nm carboxylated polystyrene colloids ( $c = 1.7 \text{ mg}\cdot\text{mL}^{-1}$ ) mixed with different concentrations of Pluronic P103 and spread at the air-water interface of a Langmuir trough at  $\text{pH} = 7$ . B-G) SEM images of the corresponding deposited monolayers near the collapse point.

From surface pressure–area isotherms the characteristic points such as the transition from a flexible to a rigid film ( $\Pi_{\text{stiff}}$ ) and defined areas ( $\Delta A_{\text{tot}}$ ,  $\Delta A_{\text{flex}}$ ) can be easily analyzed as it is exemplified in Figure 22. Simplified, the isotherm can be divided into three parts. The important point of where the molecules and colloids start interacting (A), the transition of a flexible into rigid colloid-copolymer hybrid film (B) and the collapse point (C) can be easily analyzed by extrapolating the single parts of the isotherm with their different slopes (red lines).

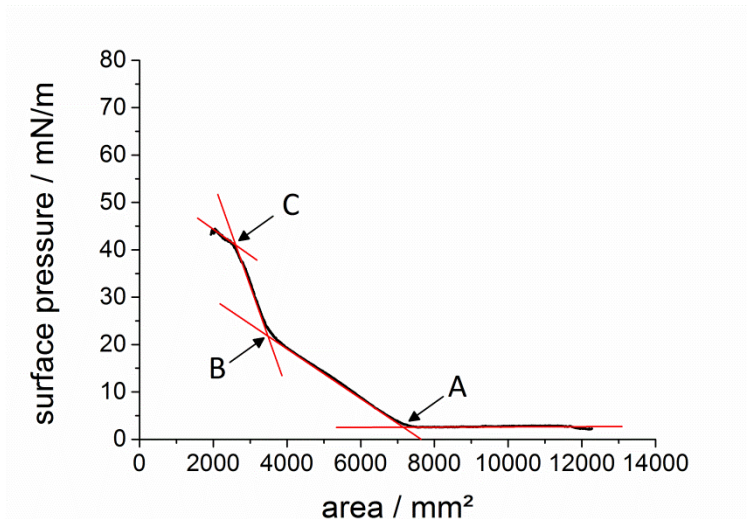


Figure 22 Exemplary surface pressure – area isotherm for a mixture of 1150 nm polystyrene colloids and 0.1 wt.% PAA<sub>14</sub>-*b*-PMMA<sub>16</sub> (black compact line) with tangents (red lines) at the different sections of the isotherm. At point A the components start to interact with each other. Further compression leads to surface pressure increase indicating colloid assembly and copolymer chain alignment. The value for the surface pressure at point B indicates the transition from a flexible to a stiff film ( $\Pi_{stiff}$ ) and point C represents the collapse point of the monolayer where multilayer formation begins.

The intersections represent the above mentioned points. The total area ( $\Delta A_{tot}$ ) is characterized by the area between zero and point A in the surface pressure – area isotherm. Here, the section of copolymer chain alignment and colloid orientation during compression ( $\Delta A_{flex}$ , area limited by A and B) as well as the rigid densely-packed part of the monolayers is included (area between A and C). The point B indicates the transition of the flexible film into a more rigid monolayer at the bend of the isotherm and therefore the moment of completed copolymer chain orientation ( $\Pi_{stiff}$ ).

Table 2 summarizes the characteristic points of the surface pressure–area isotherms for the different mixtures of colloids with varying amounts of Pluronic P103. As can be seen in Table 2, there is an increase of the surface pressure at the bend of the isotherm ( $\Pi_{stiff}$ ) with increasing amount of Pluronic P103 what can be expected as the Pluronic molecules also contribute to the total interfacial surface pressure. During compression the shallow part of the isotherm ( $\Delta A_{flex}$ ) represents the regions where the chains and blocks of the triblock-copolymer start to orient at the interface until, at the bend of the isotherm, a stiff colloid-copolymer monolayer is formed. A rough trend of slight increase of the area and the surface

pressure ( $\Pi_{\text{stiff}}$ ) with larger amount of copolymer in the mixture can be seen. Scanning electron microscopy images taken after deposition (Figure 21B-C) confirm that the Pluronic P103 has just a minor influence on the particle self-assembly, which was predicted from the isotherms. The monolayer features a hexagonal, but not very well ordered, particle arrangement. At higher concentrations of block-copolymer additive (0.1 – 0.5 wt.%) phase separation starts to appear between the colloids and the copolymer (Figure 21D-F). The corresponding isotherms (Figure 21A, 0.1-0.5 wt.%) indicate that at early compression states the interfacial film behaves more copolymer-like. The more block-copolymer is present at the interface the lower the interfacial tension and the larger the initial surface pressure of the monolayer. At high concentrations of Pluronic P103 (>1.0 wt.%) the poly(ethylene oxide)-poly(propylene oxid) block-copolymer tend to crystallize visible in between the particle islands (Figure 21G).

Table 2 Characteristic values obtained from the isotherm of a mixture of 1150 nm polystyrene colloids and different concentrations of the triblock-copolymer Pluronic P103.

$c_{\text{copolymer}} / \text{wt.}\%$	$\Delta A_{\text{tot}} / \text{cm}^2$	$\Delta A_{\text{flex}} / \text{cm}^2$	$\Delta A_{\text{flex}} / \%$	$\Pi_{\text{stiff}} / \text{mN}\cdot\text{m}^{-1}$
<b>0.01</b>	171.8	91.5	53.3	9.8
<b>0.02</b>	174.3	66.4	38.1	5.6
<b>0.05</b>	242.0	159.2	65.8	17.0
<b>0.1</b>	242.0	162.1	67.0	19.8
<b>0.2</b>	242.0	151.8	62.7	21.6
<b>0.5</b>	242.0	200.7	82.9	27.3
<b>1.0</b>	242.0	196.9	81.4	29.4

The isotherms of the dispersion with minute copolymer addition (Figure 21A, 0.01 - 0.05 wt.%) indicate minor influence of the additive on the assembly as the isotherm is of similar shape as the one of the pure colloids (Figure 19).

From the previous results, it can be deduced that mere mechanical/steric interactions of colloids with non-ionic block-copolymer molecules such as Pluronic P103 do not force the colloids to create complex chain-like or square arrangements of particles at the air-water interface as it has been described for instance by Zhou *et al.* in bulk.<sup>[150]</sup> The influence of

electrostatic interactions should be also taken into account. Therefore, like charged diblock-copolymers consisting of a hydrophilic poly(acrylic acid) block and a hydrophobic poly(methyl methacrylate) block were used to manipulate the electrostatic interactions beside the steric interactions. Due to the mechanical force during the compression of the interfacial monolayer, both, negatively charged copolymers as well as negative carboxylated colloids are pushed closer together, whereas the electrostatic repulsion of the like-charged components is increased drastically and additional dipole-dipole interactions can occur. Such short ranged dipole interactions can lead to particle alignment as theoretical considerations of Schmidle *et al.*<sup>[157]</sup> have shown.

First, the interaction of PAA<sub>17</sub>-*b*-PMMA<sub>9</sub> with 1150 nm colloids was studied using different concentrations of the copolymer. Figure 23A shows the surface-pressure-area isotherm of the hybrid film during compression and Figure 23B-F the corresponding scanning electron microscopy images. The characteristic details of the isotherm were analyzed and summarized in Table 3.

Table 3 Characteristic data from the isotherms of a mixture of 1150 nm polystyrene colloids and different concentrations of the diblock-copolymer ( $c_{\text{copolymer}}$ ) PAA<sub>17</sub>-*b*-PMMA<sub>9</sub>.

$c_{\text{copolymer}} / \text{wt.}\%$	$\Delta A_{\text{tot}} / \text{cm}^2$	$\Delta A_{\text{flex}} / \text{cm}^2$	$\Delta A_{\text{flex}} / \%$	$\Pi_{\text{stiff}} / \text{mN}\cdot\text{m}^{-1}$
<b>0.01</b>	147.6	78.0	52.8	20.9
<b>0.02</b>	162.9	61.0	57.7	18.4
<b>0.05</b>	150.2	94	40.6	24.3
<b>0.1</b>	173.6	70.3	40.5	20.1
<b>0.2</b>	203.7	156.8	77.0	27.9

In early states of the isotherm at large areas the colloids and copolymer molecules behave as described as “gaseous-like”, which corresponds to the constant surface pressure. At smaller surface areas, at the point where the interface is completely covered with colloids and copolymer molecules, the surface pressure increases slightly as it is typical for simple amphiphiles, which are still flexible regarding their orientation of the hydrophobic chains.

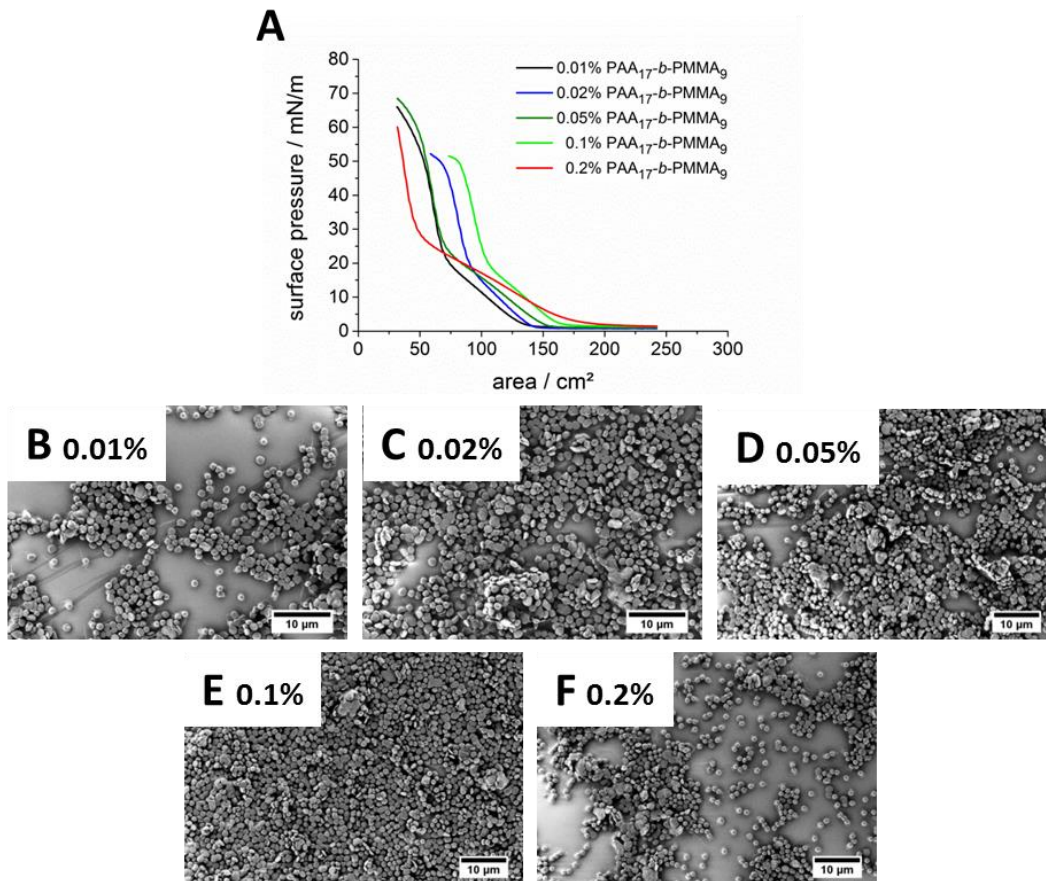


Figure 23 A) Surface pressure – area isotherms of 1150 nm carboxylated polystyrene colloids ( $c = 1.7 \text{ mg}\cdot\text{mL}^{-1}$ ) mixed with different concentrations of PAA<sub>17</sub>-b-PMMA<sub>9</sub> at pH = 7 and B-F) SEM images of the corresponding monolayers deposited near the collapse point.

When the compression proceeds there is an abrupt rise of the isotherm indicating the presence of a stiff interfacial film ( $\Pi_{\text{stiff}}$ ). Table 3 shows that with larger amount of copolymer in the colloid-copolymer mixture  $\Pi_{\text{stiff}}$  slightly increases but still it follows just a rough trend. The interfacial area of the more “copolymer-like” behavior ( $\Delta A_{\text{flex}}$ ) where the copolymer chains, especially the hydrophobic parts, begin to align at the interface is mainly > 50% of the entire area ( $\Delta A_{\text{tot}}$ ).

From scanning electron microscopy images (Figure 23B-E) it is obvious that the mechanical compression of the colloid-copolymer mixture with low molecular weight copolymer containing a larger amount of PAA than PMMA leads to agglomeration of the copolymer on the particle surface (see also Figure 24) and destroys the overall ordering. It can be concluded that this kind of copolymer is not useful for further experiments and the investigation of copolymer-colloid interactions at the air-water interface.

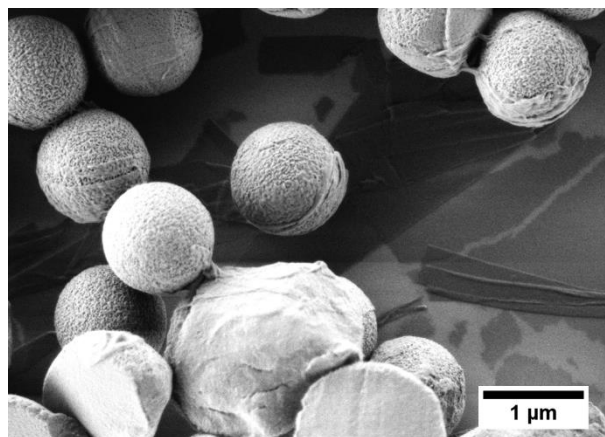


Figure 24 Copolymer molecules ( $\text{PAA}_{17}\text{-}b\text{-PMMA}_9$ ) adsorbed on 1150 nm carboxylated polystyrene colloids ( $c = 1.7 \text{ mg}\cdot\text{mL}^{-1}$ ) during simultaneous self-assembly at the air-water interface of a Langmuir trough at pH = 7.

Moreover, a copolymer with similar block lengths of hydrophilic and hydrophobic blocks ( $\text{PAA}_{14}\text{-}b\text{-PMMA}_{16}$ ) was used as additive. As can be seen from Figure 25A the isotherms for the different additive concentrations look similar as described before.

At the beginning of monitoring the surface pressure-area isotherm, there is a shallow increase in surface pressure upon compression indicating that particles and block-copolymer molecules are still flexible but start to interact sterically and electrostatically with each other. The provided area for the colloid-copolymer mixture, where the surface pressure only slightly rises during compression ( $\Delta A_{\text{flex}}$ ), becomes larger with increasing block-copolymer concentration ( $c_{\text{copolymer}}$ ) with an overall percentage of > 55% of the whole area ( $\Delta A_{\text{tot}}$ ). The data of the detailed characterization of the surface pressure–area isotherms can be seen in Table 4. For block-copolymer concentrations of 0.01-0.1 wt.% the colloids arrange in chain-like or network structures. The monolayer at the air-water interface is a stiff film, which is characterized by the sharp increase in surface pressure at about  $\Pi_{\text{stiff}} = 22\text{-}23 \text{ mN}\cdot\text{m}^{-1}$ . The shape of the isotherms for dispersions with higher copolymer concentrations (> 0.1 wt.%) closer resembles the isotherm of the pure copolymer (Figure 20B,  $\Pi_{\text{stiff}} = 30.9 \text{ mN}\cdot\text{m}^{-1}$ ). The corresponding surface pressures at the bend of the isotherm are higher than with smaller amounts of block-copolymer ( $\Pi_{\text{stiff}} = 26.8 \text{ mN}\cdot\text{m}^{-1}$  for 0.2 wt.% and  $\Pi_{\text{stiff}} = 31.7 \text{ mN}\cdot\text{m}^{-1}$  for  $c_{\text{copolymer}} = 0.5 \text{ wt.}\%$ ) and follow a precise trend.

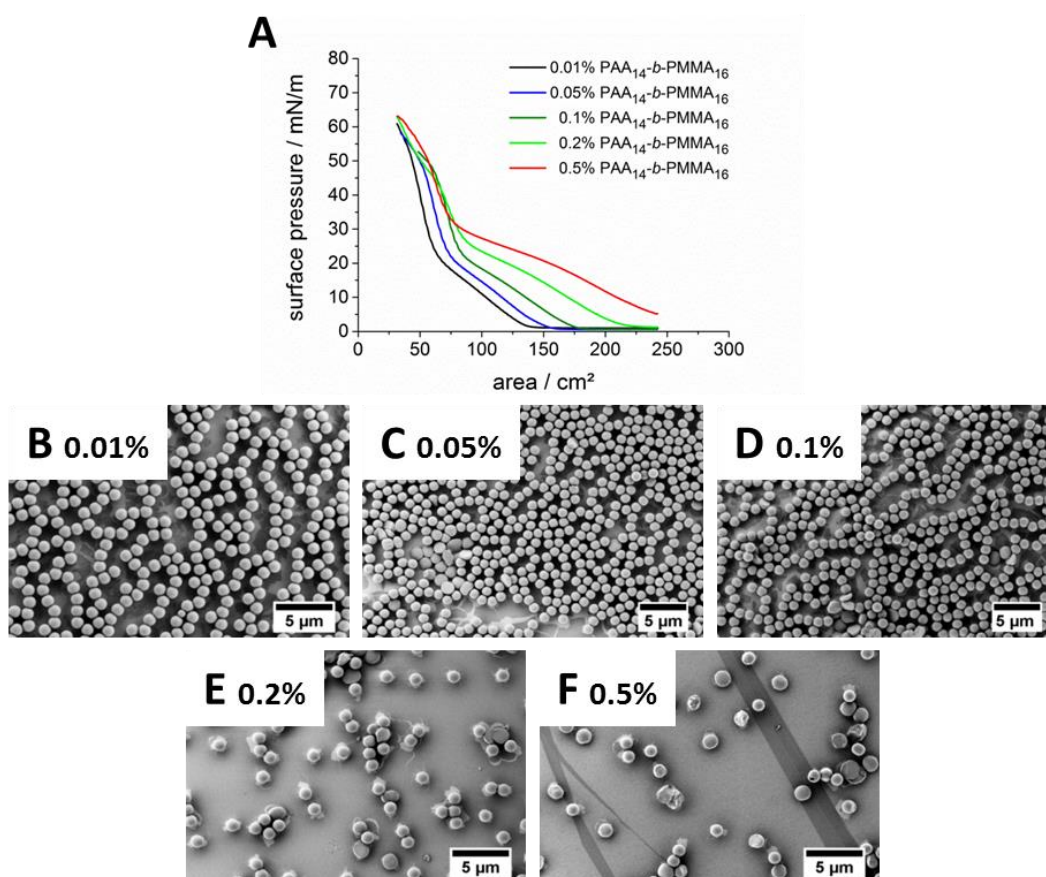


Figure 25 A) Surface pressure – area isotherms of 1150 nm carboxylated polystyrene colloids ( $c = 1.7 \text{ mg}\cdot\text{mL}^{-1}$ ) mixed with different concentrations of  $\text{PAA}_{14}\text{-}b\text{-PMMA}_{16}$  at spread at the air-water interface of a Langmuir trough at  $\text{pH} = 7$  and B-F) SEM images of the corresponding deposited monolayers.

Table 4 Characteristic data from the isotherms of a mixture of 1150 nm polystyrene colloids and different concentrations of the diblock-copolymer  $\text{PAA}_{14}\text{-}b\text{-PMMA}_{16}$ .

$c_{\text{copolymer}} / \text{wt.}\%$	$\Delta A_{\text{tot}} / \text{cm}^2$	$\Delta A_{\text{flex}} / \text{cm}^2$	$\Delta A_{\text{flex}} / \%$	$\Pi_{\text{stiff}} / \text{mN}\cdot\text{m}^{-1}$
<b>0.01</b>	147.3	84.1	57.1	21.8
<b>0.05</b>	161.8	89.7	55.4	22.5
<b>0.1</b>	184.2	103.8	56.4	22.9
<b>0.2</b>	229.3	146.2	63.8	26.8
<b>0.5</b>	242	168.1	69.5	31.7

As can be seen from the images of the deposited monolayers, only very small amounts of 0.01 to 0.1 wt.% of  $\text{PAA}_{14}\text{-}b\text{-PMMA}_{16}$  are sufficient to change the assembled structures from

hexagonal to chains and network-like structures. Furthermore, Figure 25E and F clearly show a copolymer monolayer with single particles, rather than a colloid monolayer as can be estimated also from the surface pressure area isotherms (Figure 25A, light green and red compact lines). Probably, the particles sink into the subphase as the copolymer adsorbs on the particle surface, increasing the hydrophilicity and decreasing the contact angle of the particles at the air-water interface.

The last candidate for manipulating colloid self-assembly is the low molecular weight diblock-copolymer with a larger hydrophobic than a hydrophilic block ( $\text{PAA}_{22}\text{-}b\text{-PMMA}_{30}$ ). The surface pressure-area isotherm of the colloid-copolymer mixture is shown in Figure 26A. Table 5 summarizes the characteristic details of the isotherms.

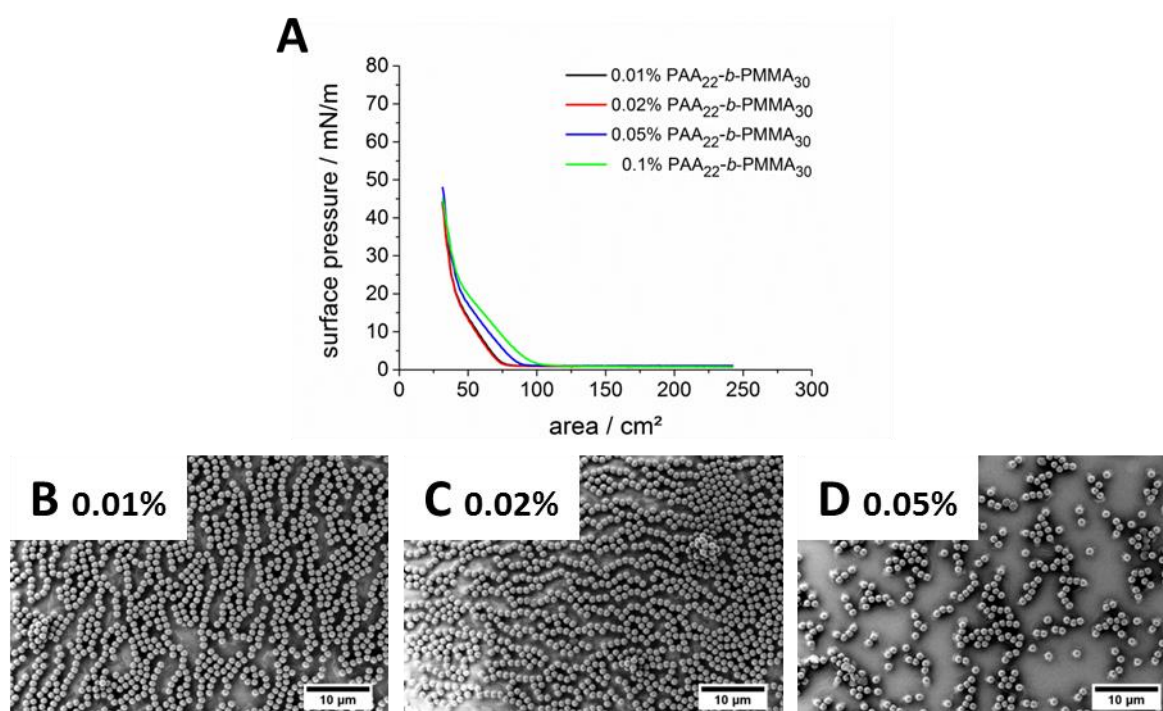


Figure 26 A) Surface pressure – area isotherms of 1150 nm carboxylated polystyrene colloids ( $c = 1.7 \text{ mg}\cdot\text{mL}^{-1}$ ) mixed with different concentrations of  $\text{PAA}_{22}\text{-}b\text{-PMMA}_{30}$  at pH = 7 and B-D) SEM images of the corresponding deposited monolayers.

Again, the surface pressure – area isotherms for the self-assembly of the colloid -  $\text{PAA}_{22}\text{-}b\text{-PMMA}_{30}$  mixture with different copolymer concentrations (Figure 26A) look alike the other isotherms of above presented mixtures of colloids and copolymers. The shallow part of the

isotherm includes much smaller total areas but the percentage of the shallow part compared to the steep part of the isotherm is similar ( $\Delta A_{\text{flex}} > 50\%$ ). The part of the isotherm with smooth increase in surface pressure is also followed by an abrupt increase in surface pressure and the formation of a very stiff film. Here, also a clear trend can be observed concerning the increase of the surface pressure at the bend of the isotherm ( $\Pi_{\text{stiff}}$ ) with increasing copolymer concentration.

Table 5 Characteristic data from the isotherms of 1150 nm polystyrene colloids and different concentrations of the diblock-copolymer PAA<sub>22</sub>-*b*-PMMA<sub>30</sub>.

$c_{\text{copolymer}} / \text{wt.}\%$	$\Delta A_{\text{tot}} / \text{cm}^2$	$\Delta A_{\text{flex}} / \text{cm}^2$	$\Delta A_{\text{flex}} / \%$	$\Pi_{\text{stiff}} / \text{mN}\cdot\text{m}^{-1}$
<b>0.01</b>	80.6	40.8	50.6	19.2
<b>0.02</b>	80.6	40.8	50.6	19.2
<b>0.05</b>	93.4	51.4	55.0	20.6
<b>0.1</b>	103.7	62.1	60.0	23.2

Scanning electron microscopy images (Figure 26B-D) show that the architecture of the colloid-copolymer monolayers is of chain-like or network character. This geometry can be formed using very small amounts of the block-copolymer (0.01-0.02 wt.%). At concentrations of about  $c_{\text{copolymer}} = 0.05 \text{ wt.}\%$  the colloidal self-assembly is suppressed and the block-copolymer is mainly present at the interface which is confirmed by SEM pictures (Figure 26D). Using higher concentrations than 0.02 wt.% has the same effect as described before, the colloids disappear from the interface and sink into the subphase or agglomerate with the copolymer due to the simultaneous compression at the air-water interface.

For further experiments the block-copolymer PAA<sub>14</sub>-*b*-PMMA<sub>16</sub> was used as it shows the most promising results for tunable colloidal self-assembly of the polymeric nanoparticles.

### 6.2.1.2. The Effect of Additives in the Water Subphase on the Amphiphile-Driven Self-Assembly of Carboxylated Polystyrene Particles

As described before, the hydrophilicity and therefore the contact angle of polymeric nanoparticles such as the negatively charged carboxylated polystyrene particles used throughout this work can be easily tuned by variation of the pH in the subphase. Additionally, the block-copolymers show different behavior at the air-water interface as it is shown in Figure 27A and B and they interact with the colloidal particles.

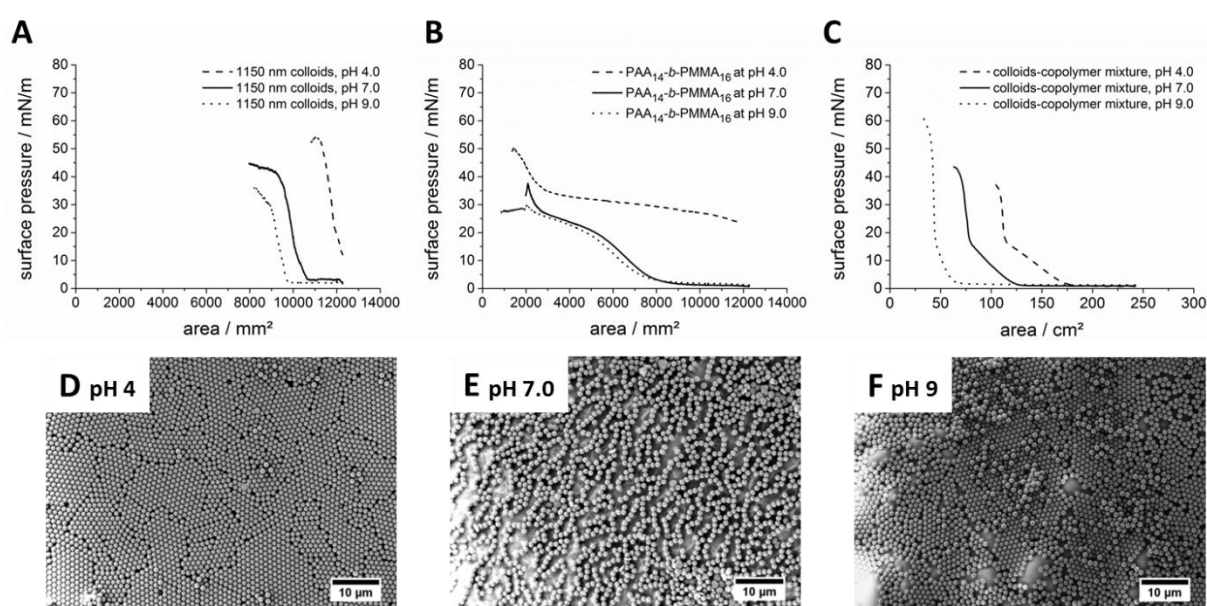


Figure 27 A) Surface pressure – area isotherm of carboxylated 1150 nm polystyrene colloids ( $c = 5 \text{ mg}\cdot\text{mL}^{-1}$ ), B) surface pressure – area isotherms of the diblock-copolymer PAA<sub>14</sub>-*b*-PMMA<sub>16</sub> and C) surface pressure – area isotherms of a colloid copolymer mixture ( $c_{\text{colloid}} = 1.7 \text{ mg}\cdot\text{mL}^{-1}$ ,  $c_{\text{copolymer}} = 0.1 \text{ wt.}\%$ ) at different pH values. D) SEM images of the colloid-copolymer mixture (C) at different pH values deposited on silicon wafers after compression at the air-water interface near the collapse point.

Compression isotherms of the pure 1150 nm polystyrene particles at different pH values show the same step slope independently on the pH. Only the initial surface tension is reduced and therefore the surface pressure increased with lower pH, as expected. The contact angle of the particles can be increased and the hydrophilicity decreased if the carboxyl functions at the particles surface are protonated at pH 4.0 ( $\text{pK}_s 5.5$ ).<sup>[134]</sup> The

interfacial properties of the block-copolymers can be also tuned by variation of the pH. The respective isotherms are presented in Figure 27B. Here, the change in hydrophilicity can be easily visualized following the surface pressure - area isotherm during compression. At high pH values ( $\text{pH} > 7$ ) all the carboxylic functions of the poly(acrylic acid) are deprotonated creating the maximum available number of negative charges. Therefore, the hydrophilicity is maximized and the isotherm is probably predominantly characterized by the surface properties of the PMMA block as most likely, the PAA blocks are swollen and directed into the subphase as has been shown by Niwa *et al.* [158] for a similar system of block-copolymers of polystyrene and poly(acrylic acid) [158]. The hydrophobicity of the block-copolymer is maximized by decreasing the pH to pH 4.0. Here, all of the acidic functions are protonated and therefore, the PAA block requires more space at the air-water interface due to the higher surface activity, which is indicated by the much higher initial surface pressure of  $\Pi = 27.7 \text{ mN}\cdot\text{m}^{-1}$  rather than  $\Pi = 1.3 \text{ mN}\cdot\text{m}^{-1}$  at pH 9. The carboxylic functions are deprotonated at high pH values, which results in an increased electrostatic repulsion of the PAA chains and, because of conformational changes, expanding of the PAA into the water subphase.

The pH of the subphase affects the colloidal properties as well as the copolymer properties at the air-water interface. Figure 27C shows the effect of different pH values of the subphase on a colloid-copolymer mixture of 1150 nm carboxylated polystyrene particles mixed with 0.1 wt.% of the diblock-copolymer PAA<sub>14</sub>-*b*-PMMA<sub>16</sub>. For better comparison the same amount of colloid-copolymer mixture was spread at the air-water interface of the Langmuir trough at different pH values. As can be clearly seen (Figure 27C) the isotherm at pH 4 and pH 7 have the same shape but at pH 7 the increase of surface pressure by compression of the interface is shifted to smaller areas. This has also been shown for the single components; colloids and copolymer molecules alone (Figure 19A and Figure 20B). The effect is based on the protonation or deprotonation of the carboxylic functions of the colloids and the copolymer molecules resulting a decrease of surficial area of copolymer and a smaller contact angle for the colloids from pH 4 to 7. [93] The direct application method of the colloid-copolymer mixture has the disadvantage that components with high hydrophilicity, at high pH for instance, tend to sink into the subphase instead of self-assembling at the air-water interface. This may also be a reason for less material located at the air-water interface.

Moreover, the surface coverage of particles and copolymer molecules for the chosen system of 1150 nm polystyrene colloids mixed with 0.1 wt.% PAA<sub>14</sub>-*b*-PMMA<sub>16</sub> was calculated. First, the area available for all copolymer molecules ( $A_{\text{tot, copo}}$ ) was determined from the surface pressure – area isotherm of PAA<sub>14</sub>-*b*-PMMA<sub>16</sub> at pH 7 (Figure 27A) by extrapolating the steep part of the isotherm to the  $x$ -axis. The area per molecule ( $A_{\text{mol, copo}}$ ) was calculated as follows:

$$N_{\text{copo}} = N_A \cdot \frac{c_{\text{copo}} \cdot V_{\text{app}}}{M} \quad (\text{eq. 18})$$

$$A_{\text{mol, copo}} = \frac{A_{\text{tot, copo}}}{N_{\text{copo}}} \quad (\text{eq. 19})$$

Here,  $N_{\text{copo}}$  stands for the number of copolymer molecules at the air-water interface,  $N_A$  for the Avogadro constant ( $N_A = 6.022 \cdot 10^{23}$ ),  $V_{\text{app}}$  for the volume of the copolymer solution spread at the air-water interface ( $V_{\text{app}} = 25 \mu\text{L}$ ) with a molecular weight ( $M = 2,900 \text{ g}\cdot\text{mol}^{-1}$ ) for the copolymer and a distinct concentration ( $c_{\text{copo}} = 2.5 \text{ mg}\cdot\text{mL}^{-1}$ ). The number of molecules located at the interface was found to be  $N_{\text{copo}} = 1.3 \cdot 10^{16}$  (molar concentration of  $n_{\text{copo}} = 2.2 \cdot 10^{-8} \text{ mol}$ ). The overall available area for the copolymer ( $A_{\text{tot, copo}} = 35.9 \text{ cm}^2$ ) obtained from surface pressure isotherm (Figure 20A) divided by the number of molecules ( $N_{\text{copo}}$ ) results in the area of a single PAA<sub>14</sub>-*b*-PMMA<sub>16</sub> molecule ( $A_{\text{mol, copo}}$ ) after compression at the interface.

For the copolymer PAA<sub>14</sub>-*b*-PMMA<sub>16</sub> the molecular area of a single copolymer chain was found to be  $A_{\text{mol, copo}} = 0.3 \text{ nm}^2$ . Afterwards, the mass ( $m_{\text{colloid, copo}}$ ) and volume ( $V_{\text{colloid, copo}}$ ) for a colloid with radius  $R = 575 \text{ nm}$  as well as for the copolymer was calculated using the following equations.

$$m = V \cdot \rho = \left( \frac{4}{3} \pi \cdot R^3 \right) \cdot \rho \quad (\text{eq. 20})$$

The density of the polystyrene colloid is  $\rho_{\text{colloid}} = 1.05 \text{ g}\cdot\text{cm}^{-3}$ <sup>[159]</sup> and the density of the copolymer was estimated to be approximately  $\rho_{\text{copo}} = 1.2 \text{ g}\cdot\text{cm}^{-3}$  as the PMMA block of the copolymer is major present at the interface with a density of  $\rho_{\text{PMMA}} = 1.18 \text{ g}\cdot\text{cm}^{-3}$ <sup>[159]</sup>, whereas the PAA block ( $\rho_{\text{PAA}} = 1.4 \text{ g}\cdot\text{cm}^{-3}$ )<sup>[159]</sup> is more directed into the water subphase. As the colloids have a spherical shape, the volume can be easily calculated. But as the real

structure of the copolymer is unclear the shape of the copolymer during compression is predicted to resemble to a random coil<sup>[158]</sup> which can also be roughly seen as a sphere with radius  $R$ . Therefore, the radius of the coil at the interface was calculated from the area per molecule as a circular area resulting  $R = 0.3$  nm as the coil radius.

$$A = \pi \cdot R^2 \quad (\text{eq. 21})$$

$$R = \sqrt{\frac{A}{\pi}} = 0.3 \text{ nm} \quad (\text{eq. 22})$$

Using only theoretical considerations for polymer chain statistics for a random coil<sup>[160]</sup> the calculation gives different results for the mean square end-to-end vector ( $\langle r \rangle^2$ ) depending on the assumptions and the chosen limitations. It can have a large effect on the calculation if only the PMMA block of the copolymer or if also the PAA block occupies space at the interface. Equations 23 and 24 represent how the mean square end-to-end distance can be calculated. One possibility for the calculation of the chain end-to-end distance ( $\langle r \rangle$ ) as the square root of the mean square end-to-end distance is based on the typical freely jointed chain (eq. 23). The other model considers also the rotation of the chains with a fixed bond angle of  $\theta = 109.5^\circ$  (eq. 24).

$$\langle r \rangle^2 = N_{bond} \cdot l^2 \quad (\text{eq. 23})$$

$$\langle r \rangle^2 = N_{bond} \cdot l^2 \cdot \frac{(1 - \langle \cos \theta \rangle)}{(1 + \langle \cos \theta \rangle)} \quad (\text{eq. 24})$$

Here,  $l$  is the C-C bond length ( $l = 0.154$  nm) between two carbon atoms and  $N_{bond}$  is the number of bonds in the polymer chain. The results for the calculation exemplary for the copolymer PAA<sub>14-b</sub>-PMMA<sub>16</sub> are summarized in Table 6. The experimentally determined radius of a single block-copolymer chain at the air-water interface is smaller with  $R = 0.3$  nm than the theoretical calculated mean square end-to-end distances  $\langle r \rangle^2$  in all cases. Considering that only the PMMA block is present at the air-water interface and using the freely jointed chain model, the calculated end-to-end distance of the polymer chain ( $\langle r \rangle^2 = 0.7$  nm) is a good approximation to the experimentally found size of the polymer coil at the interface.

Table 6 Results of the calculation for the mean chain end-to-end distance of the block-copolymer PAA<sub>14</sub>-*b*-PMMA<sub>16</sub> based on the freely jointed chain and the freely rotating chain model.

	freely jointed chain		freely rotating chain	
limitation	N <sub>bond</sub>	$\langle r \rangle^2 / \text{nm}^2$	N <sub>bond</sub>	$\langle r \rangle^2 / \text{nm}^2$
only PMMA present at interface	16	0.4	16	0.8
PMMA and PAA present at interface	30	0.7	30	0.9

The model of the freely rotating chain might be useful in polymer solutions but at the air-water interface in the absence of good solvents the polymer rather exists as a collapsed coil than a free swollen coil. Moreover, for such low molecular weight copolymers only very small surface areas per molecules are found as Niwa *et al.*<sup>[158]</sup> have also shown for PS<sub>14</sub>-*b*-PAA<sub>7</sub> copolymers. With a PS block length of 14 units the surface area per molecule was found to be about  $A = 1.1 \text{ nm}^2$ . They predict the hydrophobic block to stand straight perpendicular to the water surface at high surface pressures. Another reason for the deviation of experimentally detected and theoretical calculated results might also lie in the assumption that all block-copolymer molecules are located at the air-water interface. Probably, due to the preparation of the copolymer solution or the spreading method an undefined amount of molecules might be dissolved in the water subphase instead of being located at the air-water interface.

Equation 25 shows the calculation of the area which is covered only by the colloids ( $A_{\text{tot, colloid}}$ ) with total colloid number ( $N_{\text{colloid}}$ ) and only by copolymer chains ( $A_{\text{tot, copo}}$ ) with total molecule number ( $N_{\text{copo}}$ ) supposed that the interfacial fraction of both colloids and copolymer molecules is 100%.

$$A_{\text{tot}} = N \cdot A = \frac{m_{\text{tot}}}{m} \cdot \pi \cdot R^2 \quad (\text{eq. 25})$$

For a mixture of colloids (total mass  $m_{\text{tot, colloid}} = 5 \text{ mg}$ ) and copolymer (total mass  $m_{\text{tot, copo}} = 5 \cdot 10^{-3} \text{ mg}$ ) which were mixed and spread at the air-water interface the area covered by colloids was calculated to be  $A_{\text{tot, colloid}} = 62.1 \text{ cm}^2$  whereas the area occupied by the copolymer molecules is about  $A_{\text{tot, copo}} = 105.3 \text{ cm}^2$ . As can be seen, the self-assembled block-copolymers need 1.7 times more of the area which is covered by the colloids themselves. But from surface pressure – area isotherm (Figure 27) the area for the mixture at the interface was identified to be  $A_{\text{real, tot (mix)}} = 45.1 \text{ cm}^2$ . Compared to the area of the mixture that is covered under theoretical considerations ( $A_{\text{theory, tot (mix)}} = 167.4 \text{ cm}^2$ ) roughly 27% of the available interfacial area is occupied by the mixture. Probably, this indicates, as assumed before, that the copolymer molecules adsorb on the particle surface and do not only cover the air-water interface. As molecules adsorb on the colloids also hydrophilicity of the particles is increased resulting in the subsidence into the subphase. This is supported by the observation that direct application with a pipette leads to submersion of material during application. However, the structure of the fraction of the mixture remaining at the interface can be controlled.

Further, at pH 9 (Figure 27C, dotted line) the shallow part of the isotherm is not that well pronounced as it was found for low pH values (Figure 27C, dashed line). But still the bend of the isotherm indicating the transition from a more flexible film into a stiff film is visible at a surface pressure of about  $\Pi = 17.0 \text{ mN} \cdot \text{m}^{-1}$  for all different pH values. Moreover, SEM images after deposition near the collapse point show (Figure 27D-F) the dramatic influence of the pH variation in the subphase on the geometry of the resulting monolayers. At pH 4 hexagonal dense packing of the colloids is predominantly present (Figure 27D), whereas at pH 7 the chain-like or colloidal network orientation is favored (Figure 27E). At pH 9 the colloid-copolymer mixture tends to form aggregates or multilayers and the overall hexagonal ordering is disturbed with more defects (Figure 27F). Probably, the repulsive forces of the colloids overcome the copolymer forces at low pH and the additional electrostatic repulsion induced by the acidic groups of the PAA<sub>14</sub>-*b*-PMMA<sub>16</sub> block-copolymer are not sufficient enough to drive the particle self-assembly in another than hexagonal orientation. The electrostatic interactions are maximized at pH 9 as all functional groups of colloids and copolymers are deprotonated.<sup>[134]</sup> One could expect that particles and copolymer should be somehow equilibrated at the interface and that they are statistically distributed all over the

interface. But, the real shape and the interfacial behavior of the single blocks of the PAA-*b*-PMMA stay unknown.<sup>[158]</sup> Probably, the PAA block swells noticeably more than the hydrophobic PMMA block and the chains are more elongated into the subphase. This interfacial behavior might cause a reduced electrostatic influence on the particles and among the block-copolymer molecules. As the molecular weight of the copolymer is quite low the steric repulsion between copolymer and colloids should play a minor role at high pH. At low pH, more material is present at the interface, whereupon steric repulsion is increased. Moreover, if exclusively mechanical interactions have nearly no influence on the self-assembly as it was shown for the surfactant Pluronic P103 it is obvious that the resulting particle arrangements show hexagonal orientation as it is the general and thermodynamically most stable case for particle self-assembly.

Another possibility to control colloidal and copolymer interactions, especially the electrostatic interactions, is the addition of salts<sup>[161, 162]</sup> such as the monovalent sodium chloride (NaCl) to the subphase. The ions in the salt solution shield the surface charges. This shielding results in a reduced electrostatic repulsion between the particles. Park and Reynaert *et al.*<sup>[135, 146]</sup> showed that the addition of salt into the subphase drives sulfate functionalized polystyrene particles to aggregate at an oil-water interface and network-like structures are observed instead of hexagonal densely-packed monolayers. In contrast to Reynaert's observations a carboxyl colloid-copolymer mixture at the air-water interface behaves completely different (Figure 28). Probably, hydrogen bonding between interacting copolymer molecules and colloids is crucial for the manipulation of the colloidal self-assembly at the air-water interface. Figure 28 presents the impact of small salt concentrations in the subphase on the self-assembly of a colloid-copolymer mixture of 1150 nm colloids and 0.1 wt.% PAA<sub>14</sub>-*b*-PMMA<sub>16</sub>. The surface pressure–area isotherms for different NaCl concentrations (Figure 28A) are presented as well as the corresponding SEM images of the resulting deposited monolayers (Figure 28B-E). The salt concentrations were varied from  $c = 0 \text{ mmol}\cdot\text{L}^{-1}$  up to  $c = 100 \text{ mmol}\cdot\text{L}^{-1}$ . The colloid-copolymer mixture was spread at the salt solution and compressed. As can be seen from Figure 28A to E salt addition effects the self-assembly behavior of the colloid-copolymer mixture immensely. In the presence of  $1 \text{ mmol}\cdot\text{L}^{-1}$  NaCl (Figure 28C) the colloids arrange no longer in chains as they do in the absence of salt (Figure 28B).

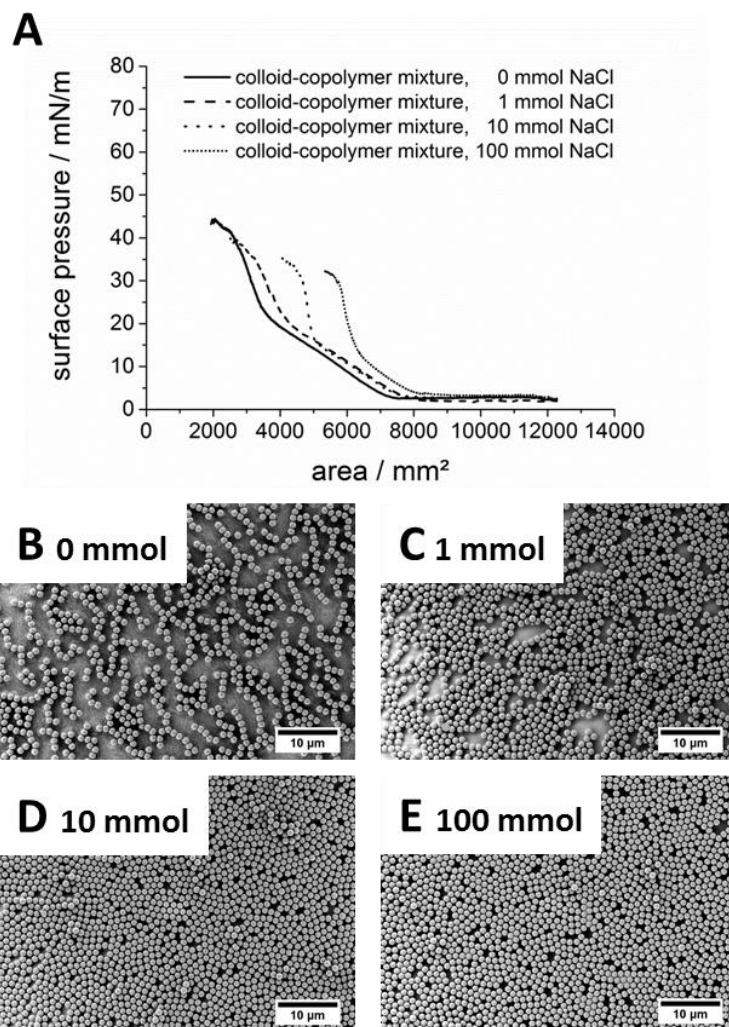


Figure 28 Surface pressure – area isotherms of a colloid-copolymer mixture consisting of 1150 nm carboxylated polystyrene colloids and 0.1 wt.% PAA<sub>14</sub>-*b*-PMMA<sub>16</sub> with different salt concentrations ( $c_{\text{NaCl}} = 0$  to 100 mmol·L<sup>-1</sup>) in the subphase at pH 7, B-E) SEM images of the resulting monolayers after deposition at the collapse point.

The particles start to organize partially in hexagonal arrangements, but there are lots of defects and voids visible. The corresponding isotherms (Figure 28A, compact and long dashed line) have nearly the same shape, a typical area with shallow increase of the surface pressure during compression followed by a sharp increase when colloids and copolymer form a very stiff film. The detailed characterization of the surface pressure – area isotherms is summarized in Table 7.

Table 7 Characteristic data from the isotherms of a mixture of 1150 nm polystyrene colloids and 0.1 wt.% of the diblock-copolymer PAA<sub>14</sub><sup>-</sup>*b*-PMMA<sub>16</sub> with different NaCl concentrations in the subphase at pH 7.

$c_{\text{NaCl}} / \text{mmol}\cdot\text{L}^{-1}$	$\Delta A_{\text{tot}} / \text{cm}^2$	$\Delta A_{\text{flex}} / \text{cm}^2$	$\Delta A_{\text{flex}} / \%$	$\Pi_{\text{stiff}} / \text{mN}\cdot\text{m}^{-1}$
<b>0</b>	74.3	39.0	52.5	22.1
<b>1</b>	78.3	37.0	47.3	20.7
<b>10</b>	80.51	30.0	37.3	16.0
<b>100</b>	85.4	22.5	26.3	12.4

The maximum surface pressure at the collapse point where multilayers are formed is reduced from  $\Pi = 43.9 \text{ mN}\cdot\text{m}^{-1}$  to  $\Pi = 40.5 \text{ mN}\cdot\text{m}^{-1}$ . At higher salt concentrations such as  $c_{\text{NaCl}} = 10 \text{ mmol}\cdot\text{L}^{-1}$  and  $c_{\text{NaCl}} = 100 \text{ mmol}\cdot\text{L}^{-1}$  a non-network structures and larger islands of hexagonal arranged colloids (Figure 28D and E) are visible. The colloids come closer together. The maximum surface pressure just before the collapse point of the monolayer is reduced from  $\Pi = 34.4 \text{ mN}\cdot\text{m}^{-1}$  for  $10 \text{ mmol}\cdot\text{L}^{-1}$  to  $\Pi = 32.0 \text{ mN}\cdot\text{m}^{-1}$  for  $c_{\text{NaCl}} = 100 \text{ mmol}\cdot\text{L}^{-1}$  (Figure 28A, dotted lines with short and longer distance). With increasing amount of salt in the subphase also  $\Pi_{\text{stiff}}$  is decreased from  $\Pi_{\text{stiff}} = 22.1 \text{ mN}\cdot\text{m}^{-1}$  to  $\Pi_{\text{stiff}} = 12.4 \text{ mN}\cdot\text{m}^{-1}$  at  $c_{\text{NaCl}} = 100 \text{ mmol}\cdot\text{L}^{-1}$ . But not only the surface pressure has been decreased, also the total area ( $\Delta A_{\text{tot}}$ ) for the monolayer formation and the part of the isotherm where the copolymer chains are adjusted during compression ( $\Delta A_{\text{flex}}$ ) is reduced upon increasing salt addition. The electrostatic repulsion of the copolymer chains is reduced upon charge shielding due to the presence of counter ions. Therefore, the electrostatic repulsive interaction of the swollen PAA block directly situated underneath the interface with the like-charged colloids is reduced and the particles can come closer together. The same is valid for the copolymer-copolymer chain interaction.

The results underline that the architecture of the colloid assemblies can be manipulated by variation of the electrostatic environment of colloids mixed with block-copolymers. This can either be done by variation of the pH or by the addition of salt. Further investigations on the interactions of the block-copolymer with the colloids, the interfacial shape and the behavior of the block-copolymer molecules are necessary for deeper understanding. Here, simulations can help to investigate the block-copolymer structure and the interactions of colloids with copolymer molecules under consideration of the forces at the interface.

### 6.2.1.3. Investigation of the Elastic Properties of the Colloid-Copolymer Hybrid Film

The colloid-copolymer film (1150 nm carboxyl functionalized polystyrene particles and 0.1 wt.% PAA<sub>14</sub>-*b*-PMMA<sub>16</sub>) in its final configuration as it has been prepared during this work seems to be a very stable monolayer. The particles stay aligned in chains and networks even after transfer to a substrate. But, as this configuration is presumably not the thermodynamically favored one, relaxation of the film followed by another compression may lead to particle rearrangement resulting in different particle assemblies. The elastic behavior of the colloid copolymer film consisting of 1150 nm colloids and 0.1 wt.% of PAA<sub>14</sub>-*b*-PMMA<sub>16</sub> was investigated by spreading the colloid-copolymer mixture at the air-water interface at pH = 7 and subsequent compression cycles. The monolayer was compressed near the collapse point at  $\Pi_1 = 43.7 \text{ mN}\cdot\text{m}^{-1}$  followed by relaxation, thus moving the barriers apart. Afterwards, the film was compressed again to a surface pressure of  $\Pi_2 = 46.7 \text{ mN}\cdot\text{m}^{-1}$ , completely relaxed and compressed one more time to  $\Pi_3 = 46.5 \text{ mN}\cdot\text{m}^{-1}$ . The resulting monolayer was transferred to a silicon substrate near the collapse point and investigated by scanning electron microscopy. Figure 29A shows the surface pressure – area isotherm of the monolayer which has been subjected to 3 compression-relaxation cycles. The SEM pictures of the monolayers after compression cycle I and cycle III are shown in Figure 29B-C.

The shape of the surface pressure–area isotherm is the same as has been described more detailed above. The typical characteristics of the isotherm such as the value for the area of the colloid-copolymer mixture compressed into a very flexible film ( $\Delta A_{\text{flex}}$ ), the entire area of the whole film formation ( $\Delta A_{\text{tot}}$ ) and the surface pressure  $\Pi_{\text{stiff}}$  at the bend of the isotherm have been listed in Table 8.

As can be seen from the isotherm in Figure 29A and from Table 8, the surface pressure  $\Pi_{\text{stiff}}$  is decreased with increasing compression-relaxation cycling number. The area of the more flexible colloid-copolymer film however, is decreasing with increasing cycle number. This can be caused by colloids and copolymer molecules that submerge into the water phase during compression especially near the collapse point and therefore they do not longer contribute to the surface pressure after relaxation and recompression. Probably, also the copolymers tend to reorganize forming a more densely package upon repeated compression.

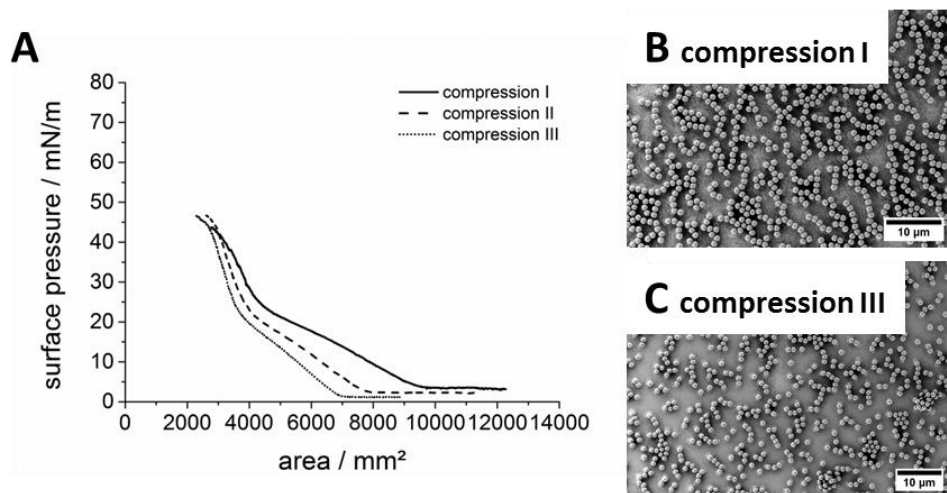


Figure 29 A) Surface pressure–area isotherm for three sequent compression – relaxation cycles of a mixture containing 1150 nm polystyrene colloids and 0.1 wt.% PAA<sub>14</sub>-*b*-PMMA<sub>16</sub> spread at pH 7 at the air-water interface, B-C) SEM images of the resulting deposited monolayers near the collapse point after being compressed once (B) and three times (C).

The monolayer at the interface is compressed to form densely patches of colloids and copolymer. These pre-formed structures of particles and copolymer molecules are quite stable and when thinking about densely packed colloidal monolayers the hexagonal arranged particles stay in their thermodynamic stable position surrounded by other colloids, even when the monolayer is carefully relaxed. Here, the copolymer molecules are also partly located in between the colloids and hinder them to crystallize in a perfect hexagonal lattice. After relaxation of the already formed densely packed monolayer (Figure 29A, compact black line) followed by another compression-relaxation cycle the chain-like arrangement of particles is not destroyed completely as can be seen in Figure 29C.

Table 8 Characteristic data from the isotherms of a mixture of 1150 nm polystyrene colloids and 0.1 wt.% of the diblock-copolymer PAA<sub>14</sub>-*b*-PMMA<sub>16</sub> resulting from successive compression-relaxation cycles of the same interfacial film.

cycle #	$\Delta A_{\text{tot}} / \text{cm}^2$	$\Delta A_{\text{flex}} / \text{cm}^2$	$\Delta A_{\text{flex}} / \%$	$\pi_{\text{stiff}} / \text{mN}\cdot\text{m}^{-1}$
I	93.8	51.7	55.1	24.7
II	77.7	38.8	49.9	22.9
III	69.8	33.2	47.6	21.6

Obviously, the network has been fragmented into shorter particle chains and also single particles surrounded by a copolymer film, thus, forming more statistically and equally distributed particle arrangements. Such equally distributed particle structures with an equilibrium distance are known for instance for silica particles grafted with PMMA brushes<sup>[163]</sup> or as described by Spatz *et al.*<sup>[164]</sup> for gold nanoparticles with polystyrene-block-poly(2-vinylpyridine) on the surface.

#### 6.2.1.4. From Particle Chains to Square Arrangements– Architecture Prediction

With small amounts of low molecular weight block-copolymers such as PAA<sub>14</sub>-*b*-PMMA<sub>16</sub> ( $c_{\text{copolymer}} = 0.01 \text{ wt.}\%$ ) different structures of self-assembled nanoparticles can be obtained. Particles align not exclusively in network-like architectures. It is also possible to create square structures with small concentrations of block-copolymer. Figure 30A presents the surface pressure - area isotherm of 1150 nm carboxylated polystyrene colloids mixed with 0.01 wt.% of the diblock-copolymer PAA<sub>14</sub>-*b*-PMMA<sub>16</sub> and spread as an 67 vol.% ethanolic dispersion at the air-water interface of a Langmuir trough. The created self-assembled structures were deposited on silicon wafers at different surface pressures and analyzed using scanning electron microscopy. Figure 30B-G represent electron microscopy images of the deposited monolayers at distinct surface pressures labeled with arrows and letters in Figure 30A. As it is shown in Figure 30A the shape of the surface pressure – area isotherm is similar as described above. First, the surface pressure of the colloid-copolymer mixture at the interface only slightly increases (Figure 30A, region between points B-D) upon compression with decreasing area before it rises sharply at  $\Pi = 23.1 \text{ mN}\cdot\text{m}^{-1}$ . Further compression forces the particle chains to arrange even closer until large-scale square polymeric crystals are constructed (Figure 30A, region between points E-G).

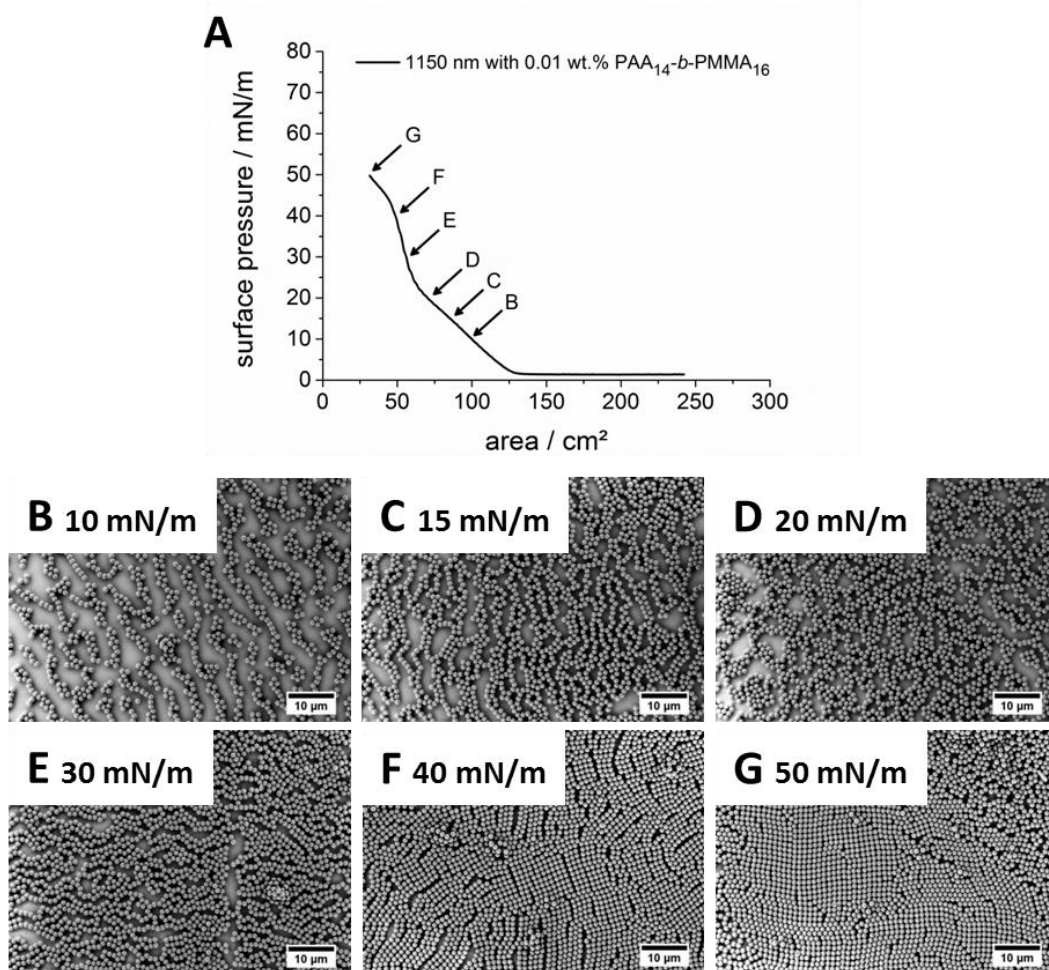


Figure 30 A) Surface pressure – area isotherm of a mixture containing 1150 nm carboxylated polystyrene colloids and 0.01 wt.% PAA<sub>14</sub>-*b*-PMMA<sub>16</sub>, B-G) SEM images of the resulting monolayers deposited at distinct surface pressures.

Figure 30B-D show the formation of network-like particle arrangements obtained when the barriers of the trough are held in the shallow part of the surface pressure–area isotherm during compression between  $\Pi = 1.5 - 23.0 \text{ mN}\cdot\text{m}^{-1}$ . Here, even at low pressures such as  $\Pi = 10 \text{ mN}\cdot\text{m}^{-1}$  (Figure 30B) the particles are arranged in chains with intersections to form a network architecture across the whole interfacial area. Near the collapse point (Figure 30A, point F,  $\Pi = 40 \text{ mN}\cdot\text{m}^{-1}$ ) large areas are visible with colloids assembled from closely oriented chains into closer packed squares. Only very small amounts such as 0.01 wt.% or even less of the diblock-copolymer PAA<sub>14</sub>-*b*-PMMA<sub>16</sub> are sufficient to control the particle self-assembly and the construction of square crystals instead of typical hexagonal arrangements. Working with higher concentrations of copolymer in the colloids-copolymer mixture as described earlier does not result in square crystal formation. There, the network-like arrangement is favored.

### 6.2.2. Conclusion and Outlook of Section 6.2

To summarize, the colloidal self-assembly can be easily controlled directly at the air-water interface of a Langmuir trough without using any special additional equipment or template substrates, only by adding amphiphilic copolymers to the dispersion. As has been presented the simultaneous arrangement of negatively charged carboxylated polystyrene colloids together with like-charged low-molecular weight copolymers such as PAA<sub>14</sub>-*b*-PMMA<sub>16</sub>, copolymers can be used to control the colloidal self-assembly at the air-water interface. The addition of polymers such as Pluronic P103, which are exclusively interacting sterically does not induce the formation of more complex architectures at the air-water interface. Chain-like and square architectures are formed depending on the composition and concentration of the copolymer molecules added as well as by the surface pressure at which the monolayer compression is stopped. Moreover, the interfacial behavior either of copolymers or colloids can be manipulated by additives in the water subphase. The addition of monovalent salts such as NaCl to the subphase affects the self-assembly by reducing the electrostatic repulsion between particles and copolymers by shielding of the charges originating from deprotonating of the carboxylic groups on the particle surface as well as in the copolymer poly(acrylic acid) block. A network-like or square structure was not obtained by addition of salt to the subphase. Another possibility to control the electrostatic repulsion between the particles and the copolymer molecules is to alter the pH of the subphase. At lower pH values than pH = 4 the carboxylic groups on the particle surface as well as the copolymer poly(acrylic acid) block are completely protonated, which increases the hydrophobicity and simultaneously reduces the electrostatic repulsion due to the decreased number of negative charges. Therefore, the particles arrange preferably in hexagonal densely packed monolayers. At higher pH values such as pH = 9 all the carboxylic functions are deprotonated, increasing surface charge and therefore also electrostatic repulsion between the components. But neither at pH = 4 nor at pH = 9 chain-like structures or square arranged colloidal crystals are visible. Only at pH = 7 the additional forces originating from copolymers seem to support other than hexagonal orientation. Mainly electrostatic interactions seem to be the key feature for controlling interfacial assemblies rather than introducing only additional steric interactions. Potentially, additional dipole-dipole interactions,<sup>[157]</sup> which are created during mechanical compression of the interfacial hybrid

colloid-copolymer film force the particles to align in chains and networks. The statistical distribution of the copolymer molecules between the colloids creates an inhomogeneity of charge distribution. The negatively charged PAA blocks of the copolymer are squeezed against the carboxylic groups of the colloids upon compression and cause an additional repulsive electrostatic force which is not homogeneous across the interface but localized at distinct patches of the colloidal surface. Polymer grafted colloids are already predicted to behave sometimes more than patchy particles due to inhomogeneous polymer brush deviation across the particle surface.<sup>[165, 166]</sup> Patchy particles have preferred interaction sites and are well known to align in chains and network structures as not only diverse simulations have shown.<sup>[11, 12, 72, 74]</sup>

What has been shown for block-copolymers such as PAA-*b*-PMMA should also apply for other statistically composed copolymers. Therefore, polymers can be produced exemplary composed of polystyrene and poly(acrylic acid) and *co*-assembled with particles at the air-water interface. As most of the forces correlate with particle size such as van-der-Waals or capillary forces more detailed investigation has to be done to evaluate the influence of the particle size. So far only 1150 nm polystyrene particles were used to create more complex structures than hexagonal arrangements. Probably, the amphiphile mediated self-assembly of smaller particles leads to a different behavior under the same conditions used in hybrid system with large particles. Potentially, with smaller amounts of copolymers the forces between colloids and copolymer molecules can be manipulated more efficiently as the repulsive and attractive forces are reduced with decreased particle diameter. Moreover, simulations can be performed explaining in detail the behavior of the copolymer molecules at the interface and their interaction with the colloids to clarify what really happens directly at the interface. To confirm that the observed structures do not result from drying effects, but on manipulated force equilibrium directly at the interface the, colloid-copolymer mixtures can be embedded in PBCA *via* gas phase mediated interfacial polymerization as it has been described before. Additionally, the self-assembly of colloids in the presence of copolymer molecules can be visualized directly at the interface using a special Langmuir microscopy trough equipped with a sapphire window for upright and inverted microscopy. Here, the self-assembly can be easily followed directly and live at the interface. Therefore, also the events in the early stages of surface compression are accessible.

### **6.3. Controlling Local Optical Properties in Colloidal Monolayers**

This section is based on the publication “Switching light with light – advanced functional colloidal monolayers” by K. Bley, N. Sinatra, N. Vogel, K. Landfester and C. K. Weiss published 2014 in *Nanoscale*, volume 6 on pages 492 (Ref. c3nr04897g). The publication is reprinted by permission from The Royal Society of Chemistry.<sup>[103]</sup>

In the previous chapter the interactions of nanoparticles with amphiphilic molecules at the air-water interface were investigated in detail. Amphiphiles were used to manipulate the electrostatic environment of the nanoparticles to form non-hexagonal complex structures such as network and pseudo square arrangements. Another possibility to create more complex architectures and functional coatings is the formation of binary crystals by co-assembly of two different colloid sizes at the air-water interface. Here, small particles are located at the interstitial sites of larger template particles arranged in a hexagonal densely packed lattice. The interstices of the binary colloidal crystal serve as a platform to create advanced coatings with locally confined functionality in the nanometer scale. This chapter presents the creation of light responsive nano-pixels using light-switchable nanoparticles situated at the interstices of large template particles. On the one hand, this chapter focusses on the production and the investigation of the physico-chemical properties of small light responsive nanoparticles. The influence of dye concentration, polymeric material on the light switching process and the persistence of the distinct switching states were investigated in detail. On the other hand, the particles were self-assembled into binary crystals and investigated with fluorescence microscopy and SEM.

#### **6.3.1. Concept of Photoswitchable Colloidal Pixels in Monolayers**

The concept for the creation of photoswitchable polymeric colloidal monolayers as a model for data storage application or light erasable barcoding is shown in Figure 31. Here, a special dye system consisting of a fluorophore and a photochrome is encapsulated in a polymeric environment in defined ratios for the production of photoswitchable colloids.<sup>[167]</sup> Thus, miniemulsion polymerization is the appropriate technique for encapsulation of various materials such as dyes in a controllable way.<sup>[58, 168, 169]</sup> The different isomerization states of

the photochromic dye CMTE were obtained by irradiation with UV and visible (VIS) light, respectively. The resulting polystyrene (PS) and poly(butyl acrylate) (PBA) based colloids were covered with an additional rigid shell of PS by seeded emulsion polymerization as protection for low glass temperature ( $T_g$ ) polymers such as PBA and to narrow the size distribution of the colloids.<sup>[170, 171]</sup> The seeded colloids can be self-assembled for the creation of functional photoswitchable and highly ordered colloidal monolayers.

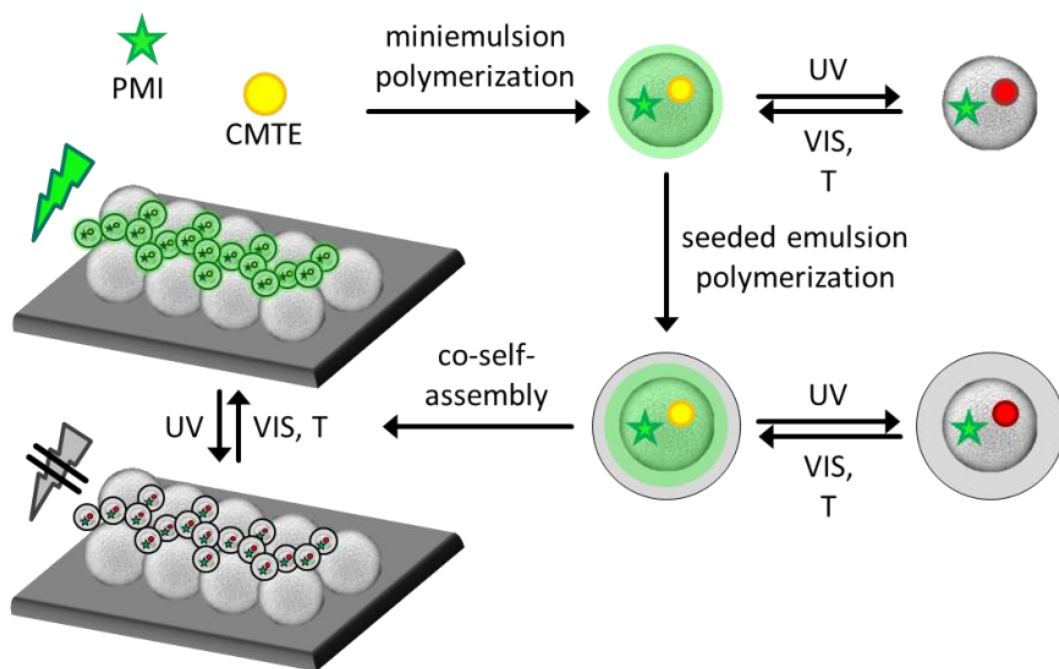


Figure 31 Concept for the production of photoswitchable nano-pixels in colloidal monolayers with binary superstructure.<sup>[103]</sup>

To produce functional photoswitchable colloidal monolayers a dye system based on a bis-thienyl photochrome (*cis*-1,2-dicyano-1,2-bis-(2,4,5-trimethyl-3-thienyl) ethene, CMTE) and a perylene based fluorophore (*N*-(2,6-diisopropylphenyl)-perylene-3,4-dicarboximide, PMI) was used (Figure 32A). Upon irradiation with UV or VIS-light the CMTE molecule undergoes a ring-closing or ring-opening cyclization (Figure 32), respectively which can be detected by UV-VIS absorption spectroscopy.

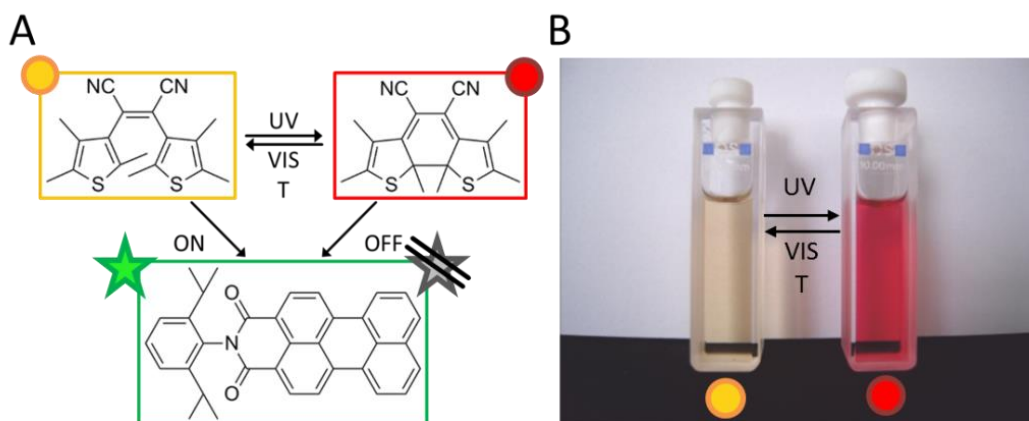


Figure 32 (A) Dye system consisting of the photochrome CMTE in the ring-opened ground state (yellow, left) and in the ring-closed excited state (red, right) obtained by irradiation with light of different wavelengths or temperature induced isomerization in relation to the fluorescent dye PMI (green, lower part), (B) quartz cuvettes with solutions of the photochromic dye in styrene after VIS-light irradiation (yellow, left) and after UV-light irradiation (red, right).<sup>[103]</sup>

In contrast to the ring-open isomer (yellow solution, Figure 32B, left), the ring-closed excited isomer of the CMTE shows a broad absorption maximum at  $\lambda = 520$  nm (red solution, Figure 32B, right) and is able to absorb PMI's emission between  $500 \text{ nm} < \lambda < 620 \text{ nm}$  (Figure 33). The emission of PMI is switched off. After VIS-light irradiation the emission can be switched on again. The dashed black part of PMI's emission spectra (Figure 33) is the residual fluorescence emission which is not absorbed by the photochromic dye. Although the isomerization from the ring-closed into the ring-open state is thermodynamically favored, excellent thermal stability has been reported giving the photochrome a kind of "memory" ability.<sup>[172]</sup> The excited, ring-closed state thermally relaxes into the ring-open state due to the thermodynamically unfavorable strained ring configuration and the loss of aromaticity of the thiophene rings (Figure 32A).<sup>[173]</sup> Investigation of the thermal stability of CMTE in the monomers styrene and butyl acrylate showed that the half-life ( $t_{1/2}$ ) of the ring-closed CMTE is about  $t_{1/2} = 5.2$  min in solutions of styrene and  $t_{1/2} = 6.8$  min in butyl acrylate, respectively. The rate constants were calculated from the linear decay fit (eqn. 26 and 27).

$$y = mx + n \quad (\text{eq. 26})$$

$$k = -m \quad (\text{eq. 27})$$

Here,  $y$  stands for the measured fluorescence emission,  $x$  is the time,  $n$  the intercept on the  $y$ -axis, and  $m$  is the slope from which the rate constant  $k$  is calculated (eq. 26, 27). As expected, the rate constants show that the thermally activated ring opening reaction of CMTE proceeds with almost similar reaction rates in both monomers. The solvents do not seem to restrict conformational changes during isomerization. This should differ when CMTE is embedded in a polymeric matrix. In this environment, the stiffness or flexibility of the polymer, expressed by the glass transition temperature ( $T_g$ ), is expected to have a bigger influence on the geometry and conformational changes during cyclization and therefore on the switching process.

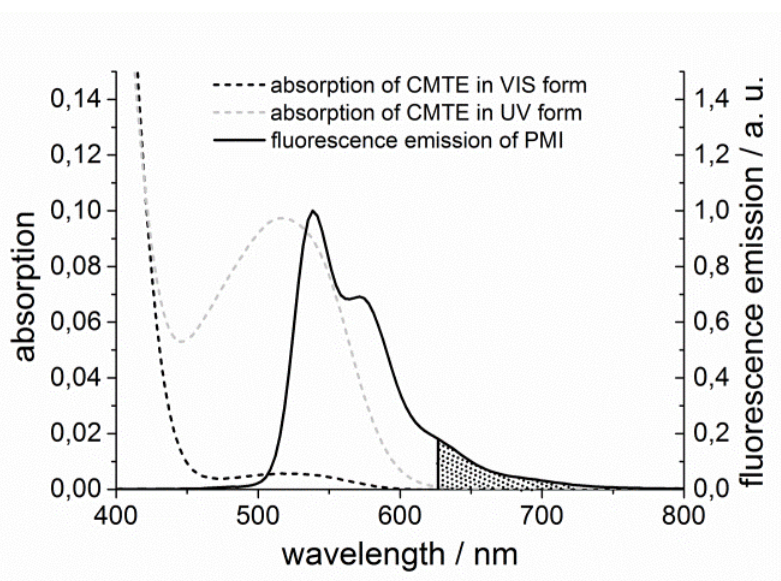


Figure 33 Absorption and emission spectra showing the spectral overlap of the fluorophore's emission (PMI, black compact line) and the photochrome's absorption maximum (CMTE, ground state black dashed line, excited state light grey dashed line) in styrene.<sup>[103]</sup>

In solutions and even in polymer films the molecules can easily diffuse thus compromise the addressability of a defined spatial storage "pixel" of information or readout. However, when incorporated into spatially confined colloidal particles, which are subsequently assembled into a two-dimensional array, diffusion of dye is effectively suppressed and individual pixels with resolution defined by the size of the colloids are obtained. The stability of the dye system can be increased by embedding the dyes into a polymeric matrix to prevent the thermally induced ring-opening cyclization that will compromise the storage of information

over longer periods of time is obtained. Moreover, addressable units of this dye system are necessary for a defined system of high addressability and easy readout. Therefore, small entities of the dyes were encapsulated in polymeric colloids using the miniemulsion technique.<sup>[58, 168]</sup> Such colloids can be used later in a self-assembly process to create colloidal pixels. As the polymeric matrix can affect the switching process of the dye because of geometric restrictions the influence of the polymeric environment was investigated using poly(butyl acrylate) (PBA) as a soft polymer with low glass transition temperature  $T_g$  ( $T_g \ll$  room temperature [RT]) and polystyrene as a rigid polymer ( $T_g \gg$  RT). Polymers with low  $T_g$  such as PBA are not suited for a subsequent assembly of the formed colloids into a colloidal monolayer because they immediately fuse together and form a film. To prevent film formation and to allow the application of soft PBA colloids in self-assembly, a seeded emulsion polymerization approach was used to generate a rigid shell around the PBA colloids for protection.<sup>[171, 174]</sup> Another advantage of the seeded emulsion polymerization is the adjustment of size and reduction of size distribution,<sup>[174]</sup> which promotes the formation of monolayers with higher order during the self-assembly process. The size distribution plays an important role in the creation of densely packed colloidal monolayers. The highest overall ordering quality can be obtained using particles of uniform size, whereas colloids of broader size distribution reduce the ordering quality at the air–water interface. The photoswitchable colloids were self-assembled into ordered complex binary monolayers. With some geometric models the particle size range for the small particles which can be co-crystallized can be determined.<sup>[175]</sup> The binary monolayers prepared by the co-crystallization method are of high crystallinity and ordering degree because the interstices tolerate a broad range of sizes for the smaller colloids without disturbance of the larger particles self-assembly.

### **6.3.2. Photo-Physical Properties of Nanoparticles with Photoswitchable Emission**

The miniemulsion polymerization is the appropriate technique to encapsulate multiple compounds in defined ratios in a variety of different polymeric materials. Therefore, a quantitative encapsulation of the dye system for switching fluorescence emission with adjustable ratios in the used polymers (PS and PBA), is guaranteed. To investigate whether

the polymeric matrix restricts the switching process styrene and butyl acrylate (BA) were used as monomers for the miniemulsion approach. The particle size was measured by photon cross correlation spectroscopy resulting a particle diameter ( $D$ ) of  $D = 90$  nm (standard deviation of  $\sigma = \pm 14$  nm or  $\pm 17\%$ ) for the PS particles and  $D = 155$  nm ( $\sigma = \pm 20$  to  $30$  nm or  $\pm 13$  to  $19\%$ ) for the PBA colloids (Table 9).

Table 9 Physicochemical characterization of the nanoparticles prepared by miniemulsion polymerization and seeded emulsion polymerization

sample	polymer	PMI:CMTE	$D$ / nm	$\sigma$ / nm	distribution	$T_g$ / °C
<b>KB111213A</b>	PS	1:18	84	14	17	71
<b>KB111213B</b>	PS	1:37	94	16	17	72
<b>KB111213C</b>	PBA	1:18	159	20	13	-56
<b>KB111213D</b>	PBA	1:37	155	30	19	-49
<b>KB120621A</b>	PS-PS	1:18	191	17	9	88
<b>KB120621B</b>	PBA-PS	1:18	260	31	12	93

Figure 34A and B show scanning electron micrographs of the prepared photoswitchable colloids by miniemulsion technique. The small polystyrene particles are rigid round shaped spheres whereby the PBA colloids flew on the silicon wafer due to their low  $T_g$ . Therefore, the creation of a protective shell, especially for low  $T_g$  polymers such as PBA is essential for further self-assembly and deposition approaches. The formation of a PS shell around the functional colloids, however, does not only serve a protective purpose. The size distribution of the colloids can also be narrowed by the process<sup>[174]</sup> as mentioned before. The particle size was also determined by photon cross correlation spectroscopy resulting a diameter of  $D = 191$  nm (standard deviation of  $\sigma = \pm 17$  nm or  $\pm 9\%$ ) for the PS covered polystyrene colloids (PS-PS) and  $D = 260$  nm ( $\sigma = \pm 31$  nm or  $\pm 12\%$ ) for the PS covered poly(butyl acrylate) colloids (PBA-PS). The optical properties of these colloids have also been investigated. The data were summarized in chapter 6.3.2.1.

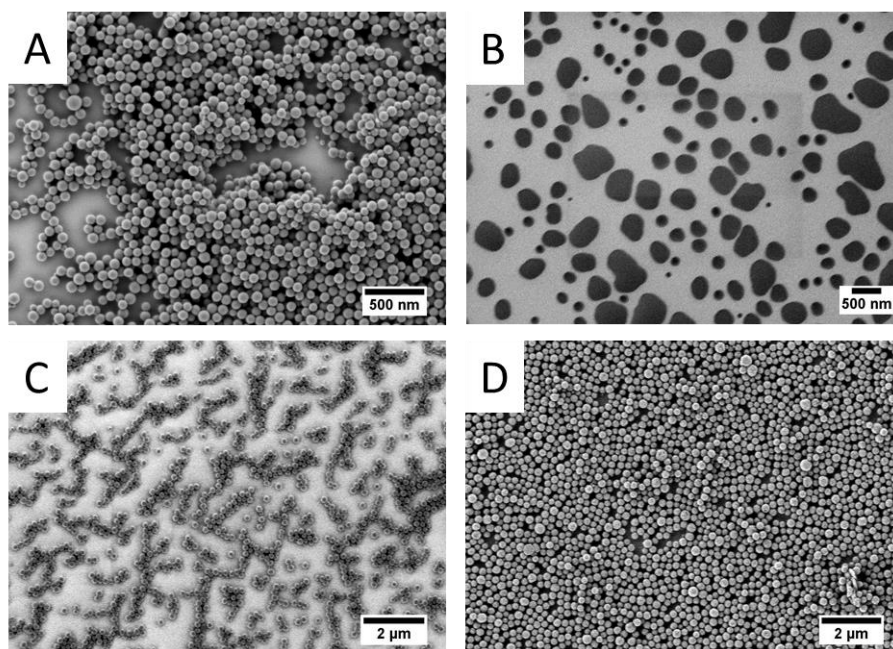


Figure 34 Scanning electron microscopy images of colloids prepared by miniemulsion polymerization A) poly(styrene) (PS,  $D = 84 \pm 14$  nm), B) poly(butyl acrylate) (PBA,  $D = 159 \pm 20$  nm) and colloids produced by seeded emulsion polymerization of the smaller colloids from miniemulsion C) PS-PS ( $D = 191 \pm 17$  nm) and D) PBA-PS ( $D = 260 \pm 31$  nm) on silicon wafer substrates.<sup>[103]</sup>

The glass transition temperature of polystyrene is lowered compared to pure PS ( $T_g = 100$  °C)<sup>[176]</sup> resulting in a value of  $T_g \approx 72$  °C due to the encapsulation of hexadecane and the dye molecules (Table 9). The rigidity of polystyrene may lead to conformational restrictions for the geometric changes of the CMTE molecules during the irradiation process. Poly(butyl acrylate) is a “soft” polymer with  $T_g \approx -50$  °C.<sup>[176]</sup> Photoswitching is expected to occur faster in a softer and more flexible polymeric environment, which means that the emission intensity of the fluorescent dye should be reduced with higher rate constants in PBA than in PS. The irradiation experiments with UV and VIS-light of the different polymeric colloids with varying amounts of photochromic dye were described in the following chapters.

### 6.3.2.1. UV-light Induced Photocyclization Reaction in Colloids Prepared by Miniemulsion Polymerization

The absorption of PMI's fluorescence emission can be described as intercomponent energy transfer between the fluorophore and the photochrome. Thus, the distance between the CMTE and the PMI molecules, which is determined by the concentration, affects the efficiency of the absorption of PMI's emission. The efficiency of the energy transfer decreases with increasing molecule distance. Thus, the influence of varying amounts of photochromic dye on the energy transfer or on the switching process, respectively, was investigated in different polymeric environments. The development of the fluorescence intensity of the PMI during the irradiation was followed by fluorescence spectroscopy as the emission maximum at a wavelength of  $\lambda_{em} = 561$  nm changes with time due to the formation of the ring-closed or ring-open state of CMTE and, therefore, varying concentrations of molecules absorbing the fluorescence intensity of PMI. Emission spectra were recorded after given intervals of UV-light irradiation until no further increase of the emission signal was visible. Figure 35A shows the time dependent decrease of the emission of the fluorescent dye PMI in a colloidal system of polystyrene and poly(butyl acrylate) in the presence of the photochromic dye CMTE (ratios of PMI to CMTE such as 1:18 and 1:37). After about 3–4 min of UV-irradiation no further decay of fluorescence is visible, indicating that the entire CMTE has isomerized into the ring-closed form.

From the data, the rate constants for the fluorescence intensity decrease at the maximum at  $\lambda_{em} = 561$  nm were calculated with an exponential fit (eq. 28, 29).

$$y = A \cdot \exp(-x/t) + y_0 \quad (\text{eq. 28})$$

$$k = t^{-1} \quad (\text{eq. 29})$$

The variable  $y$  is the measured emission,  $x$  is the time,  $A$  the amplitude of the exponential fit,  $y_0$  is the offset, and  $t$  is the time constant from which the rate constant  $k$  is calculated. The rate constants for all particles during irradiation and thermally induced recovery were summarized in Figure 36.

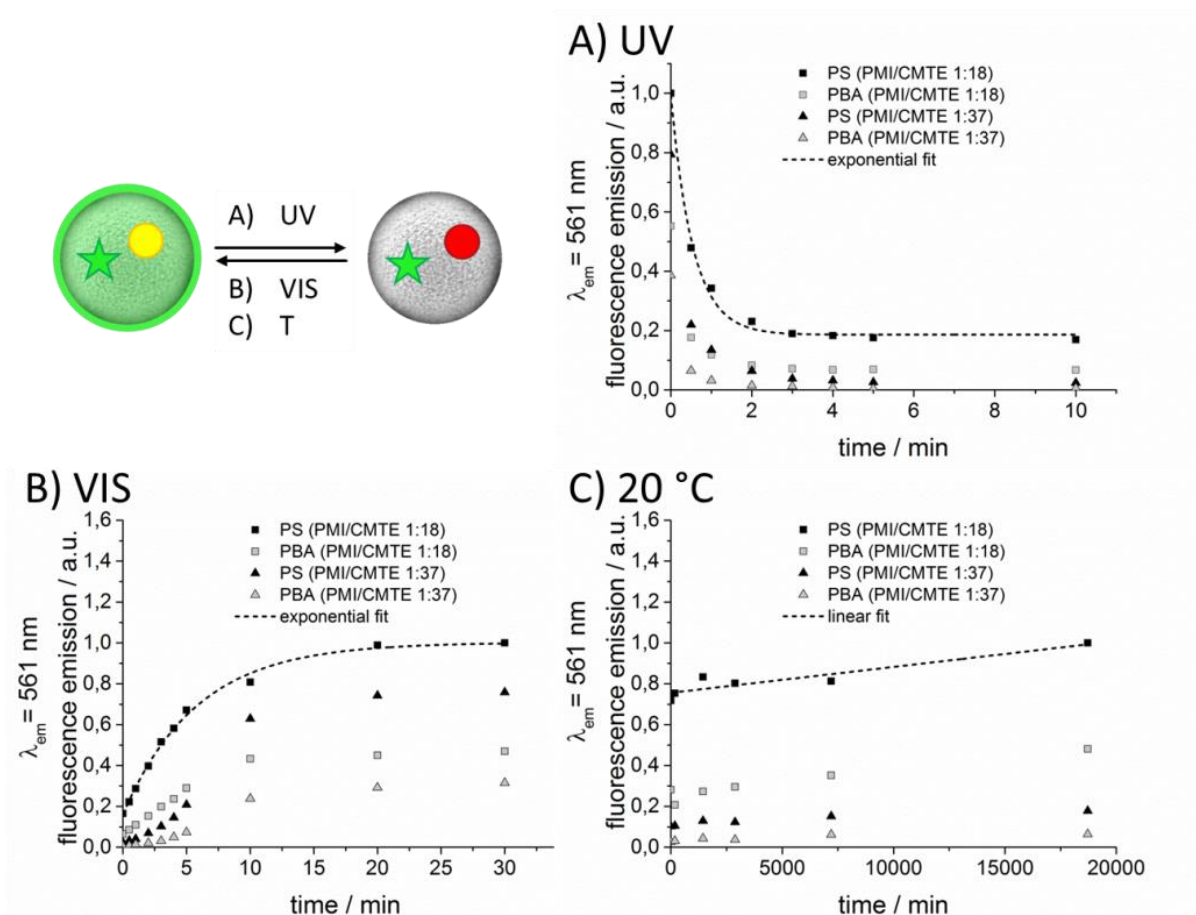


Figure 35 Time dependence of the fluorescence intensity ( $\lambda_{em} = 561 \text{ nm}$ ) of the colloidal dispersions of PS and PBA particles during (A) UV-light irradiation, (B) VIS-light irradiation and (C) storage of the dispersions in the dark at room temperature for PMI/CMTE ratios of 1:18 and 1:37. Only one representative black dashed fitting curve per diagram is shown for clarity.<sup>[103]</sup>

The rate constants for the UV-light irradiation of colloids with encapsulated photoswitchable dye system show that the fluorescence emission intensity of the PMI in PS and in PBA can be successfully reduced by the ring-closed form of the CMTE. As expected, the switching in poly(butyl acrylate) proceeds about 60% faster than the photoswitching in polystyrene. The stiffness of the polystyrene matrix could decelerate the isomerization process because of geometric or steric restrictions.

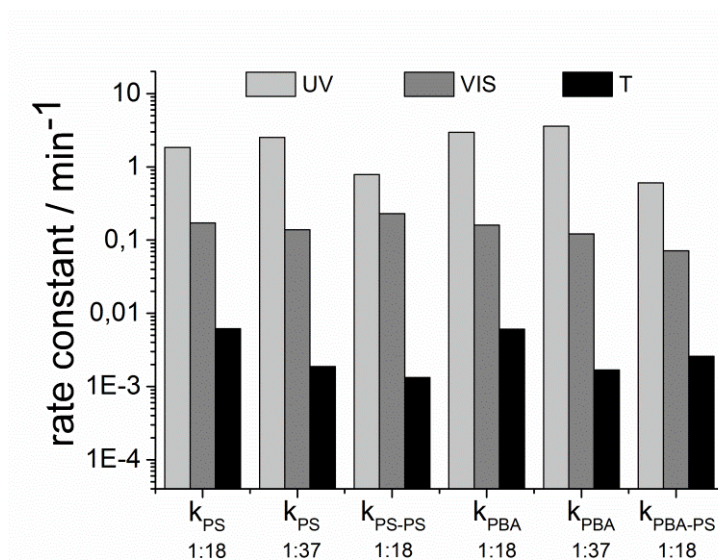


Figure 36 Rate constants in logarithmic scale for the isomerization induced by irradiation with UV (light grey) and VIS-light (dark grey) as well as thermally induced isomerization (black) for the colloids with varying amounts of CMTE.<sup>[103]</sup>

Moreover, the effect of CMTE concentration on the switching efficiency was investigated. The temporal evolution of the fluorescence emission of the dispersions upon irradiation with UV-light containing a higher amount of CMTE (PMI:CMTE such as 1:37, Figure 35A, black and grey triangles as data points) shows that the fluorescence stays at a constant level after 3 min for PS and PBA, respectively. The emission of the system containing the dyes with ratio 1:37 in PS as well as in PBA is significantly lower than that with a ratio of PMI:CMTE of 1:18 (Figure 35A, black and grey squares as data points). As expected, the switching process with higher concentration of CMTE was faster with increasing amount of activated quenching molecules in the environment of the fluorescent dye (Figure 36). Compared to the rate constants of the particles with a ratio PMI:CMTE of 1:18, the rate constants of the intercomponent energy transfer process between the ring-closed form of CMTE and the PMI can be increased by 37% for the polystyrene particles and 21% for the poly(butyl acrylate) nanoparticles when using a higher amount of CMTE (ratio PMI:CMTE such as 1:37).

### **6.3.2.2. VIS-light Induced Reverse Cyclization Isomerization Reaction in Colloids Prepared by Miniemulsion Polymerization**

For the reverse isomerization process the samples were irradiated with visible light in the wavelength range of  $515 \text{ nm} < \lambda < 690 \text{ nm}$ . The corresponding emission spectra (Figure 35B) show a time dependent increase of the fluorescence maximum at  $\lambda_{em} = 561 \text{ nm}$ , which correlates with the increasing amount of CMTE molecules isomerized into the ring-open state, which are not able to quench the emission because of the missing spectral overlap of CMTE absorption and PMI emission. The initial intensity of PMI's emission in polystyrene recovered after 20 min of irradiation. The switching rate constants were similar in the different polymeric environments of PS and PBA colloids and generally about an order of magnitude lower than that of the UV-induced isomerization (Figure 36). For the polystyrene particles with a dye ratio of PMI:CMTE of 1:37 a rate constant 20 times slower and for the dye ratio 1:18 a rate constant 10 times slower than the isomerization in solution were calculated for the VIS-light induced ring-opening reaction. For the PBA particles similar behavior was observed but the isomerization was found to be about 20 times slower for a ratio of PMI:CMTE of 1:18 and 30 times slower for a ratio of 1:37 than the isomerization in solution.

### **6.3.2.3. Reversibility of the Cyclization Process**

It was shown successfully that the fluorescence emission of the colloids with the chosen dye system can be switched by optical stimulation at different wavelengths in UV and visual range. For any applications a high reversibility and high number of cyclization cycles of the emission are necessary. To perform several switching cycles of alternating irradiation with visible and UV-light of PS colloids with the ratio of PMI:CMTE of 1:18 were used. The dispersion was irradiated with UV-light first to ensure all CMTE is present in the excited state, whereas the particle's emission was switched off. Afterwards, the ring-opening reaction was initiated by VIS-light irradiation isomerizing CMTE to the ground state, thus, switching the particles on. After 30 min of irradiation the fluorescence emission of the sample was investigated by fluorescence spectroscopy. Afterwards, the dispersion was again

irradiated with UV-light to initiate the ring-closing reaction. This procedure was repeated several times to obtain a higher number of switching cycles. The resulting emission intensities show the presence of the two states for fluorescence emission (on/off) in colloids for a well-repeatable isomerization, whereas the emission intensities can be restored almost completely for every switching cycle, indicating good photoswitchability (Figure 37).

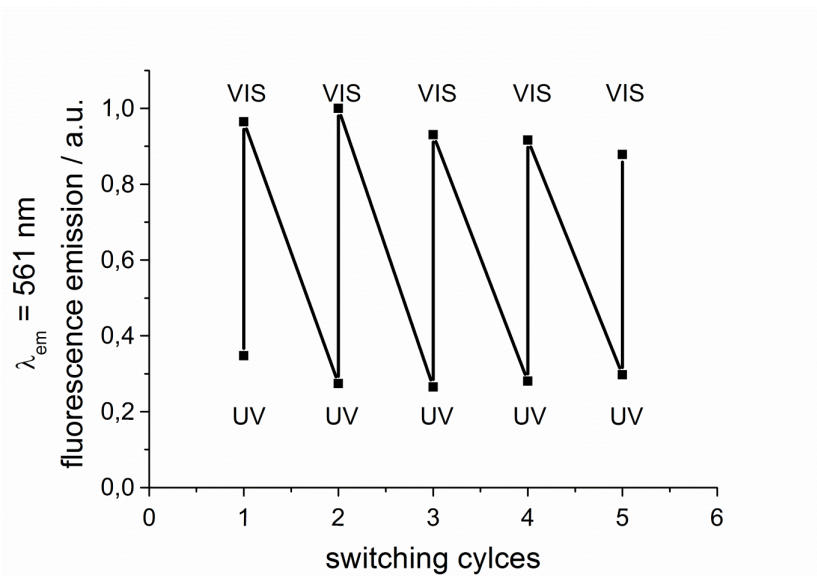


Figure 37 Fluorescence emission at  $\lambda_{em} = 561$  nm of the PS dispersion (PMI:CMTE 1:18) for reversible switching between the on and the off state induced by alternating irradiation with UV and VIS-light over five switching cycles.<sup>[103]</sup>

Slight intensity changes might originate from reduced power of the UV-lamp used throughout the irradiation experiments. Moreover, the temperature in the irradiation chamber increased under continuous irradiation with the UV-lamp which can lead to the thermally activated cyclization reactions of the CMTE resulting in different emission intensities of the colloids.

### 6.3.2.4. Thermal Stability of the Photo-States in Colloids Prepared by Miniemulsion Polymerization

The stability of the individual on/off states in the absence of a stimulus is of great importance. Storage of information can only be realized with stable and defined states. Although the ring-closed form of CMTE is the thermodynamically unstable state, the thermally activated ring opening isomerization can be decelerated by embedding the dye

molecules in a polymeric environment of a colloid. Figure 35C shows the time evolution of the fluorescence intensity at  $\lambda_{em} = 561$  nm of UV-light irradiated dispersions and storage in the dark at room temperature. In both polymeric particles the fluorescence recovery is very slow. Complete recovery of the emission was not observed even after more than 10 days. The data acquired from the system with a ratio of PMI:CMTE of 1:37 are also shown in Figure 35C. Compared to the nanoparticles with a lower ratio PMI:CMTE of 1:18 the fluorescence intensity decreases with a similar rate constant. Comparing the rate constants for the thermally induced restoration it is obvious that the reverse cyclization reaction into the ring-open form proceeds with a similar velocity not depending on the nature of the surrounding polymeric matrix (Figure 36). The results underline the excellent thermal stability of the ring-closed state of CMTE and the steric hindrance of the isomerization in a polymeric environment. The dye system is at least 20 times more stable when being embedded in a polymeric matrix than in solution and light-induced information can easily be stored for more than 10 days.

To summarize, the optical properties and the rate constants confirm that the photoswitching with UV-light proceeds faster in a soft polymeric matrix such as poly(butyl acrylate) ( $T_g \approx -50$  °C) than in a rigid matrix such as polystyrene ( $T_g \approx 71$  °C) (Table 9). The VIS-light induced ring opening reaction has a rate constant which is about 10 times smaller than the rate constant for UV-light induced ring closing cyclization. The fluorescence emission can be reversibly recovered by alternating irradiation with visible light within the wavelength range of  $515 \text{ nm} < \lambda < 690 \text{ nm}$  and UV-light for several switching cycles without any enormous photobleaching effects. The states of the photochromic system show excellent thermal stability when being embedded in polymeric colloids.

### **6.3.2.5. UV-light Induced Photocyclization Reaction in Colloids Prepared by Seeded Emulsion Polymerization**

As mentioned before, the protection of the low  $T_g$  colloids with an additional shell of rigid polystyrene is on the one hand necessary for self-assembly processes. On the other hand it is a well-known possibility to narrow the size distribution of PS and PBA seed colloids produced by miniemulsion polymerization.<sup>[174]</sup> As the seed particle ideally does not change, the

resulting optical properties are expected to be similar to that of the seed particle, with the exception of lower emission intensity. Although the emission intensity is less intense than that from the seed particles the decrease in the emission maximum at  $\lambda_{em} = 561$  nm with proceeding isomerization is still visible and follows an exponential decay (Figure 38A).

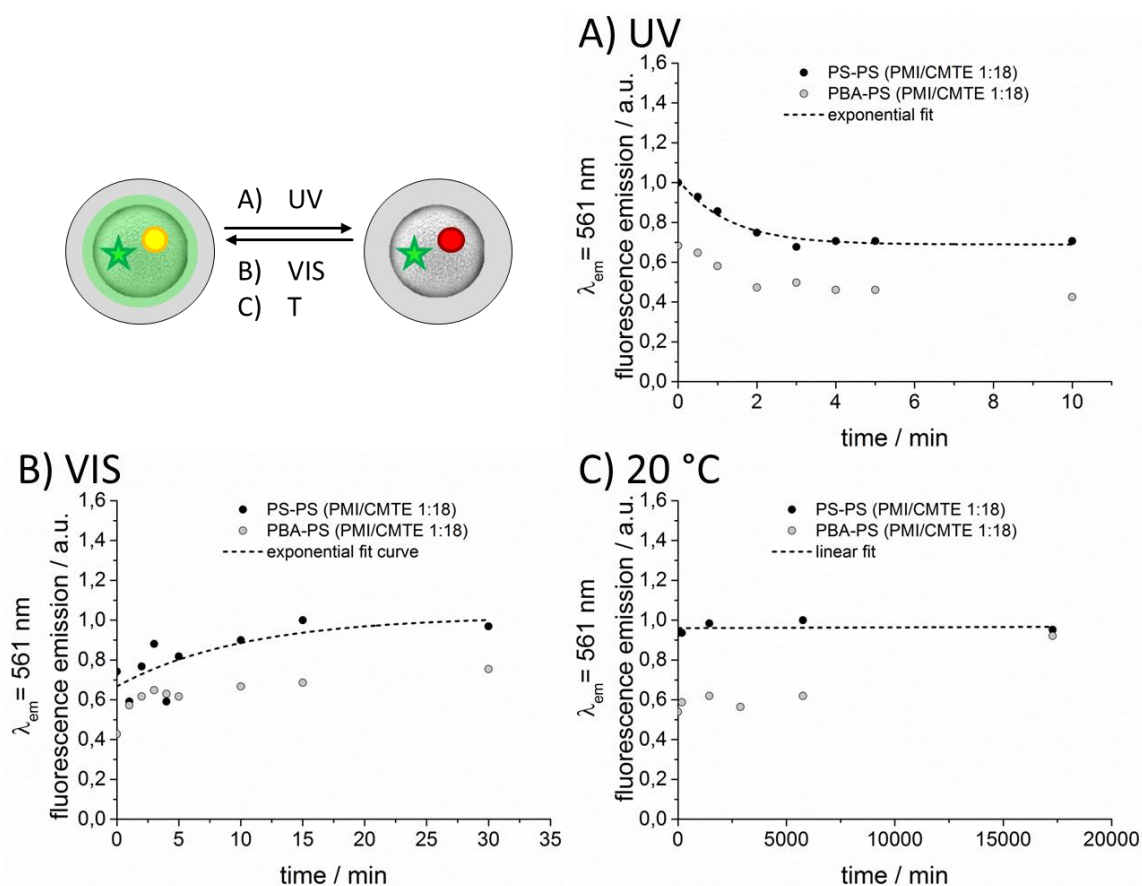


Figure 38 Time dependent development of the fluorescence intensity at  $\lambda_{em} = 561$  nm of the colloidal dispersions of seeded PS–PS and PBA–PS particles during (A) UV-light irradiation, (B) VIS-light irradiation and (C) storage of the dispersions in the dark at room temperature for the ratio of PMI:CMTE of 1:18 (black and grey dots as data points).

The corresponding rate constants of the seeded particles (Figure 36, light grey bars) show that the switching process during UV-light irradiation was decelerated by 58% for the PS-PS and about 80% for the PBA-PS particles compared to the original seed particles from miniemulsion. The differences may arise from scattering effects due to the enlargement of the particles and the additional shell of polystyrene whereby less light reaches the inner functional core of the hybrid seeded particles or light is scattered by the rigid PS matrix.

### **6.3.2.6. VIS-light Induced Reverse Cyclization Isomerization Reaction and Thermal Stability of the Photo-States in Colloids Prepared by Seeded Emulsion Polymerization**

The fluorescence recovery induced by irradiation with visible light with a wavelength range of  $515 \text{ nm} < \lambda < 690 \text{ nm}$  is shown in Figure 38B. After 15 min the fluorescence intensity reaches the initial value. The hybrid particles with an additional protective shell of polystyrene show similar switching behavior as the seed particles prepared by miniemulsion polymerization. The switching process seems to be slightly decelerated but the rate constants lie in the same dimension as the ones for the miniemulsion polymerization (Figure 36, dark grey bars). This effect might be attributed to scattering effects of the larger particles and of the polystyrene matrix.

Figure 38C shows the time dependent development of the thermally induced ring opening reaction of CMTE. The increase of the fluorescence intensity of PMI at  $\lambda_{em} = 561 \text{ nm}$  was plotted versus time and the rate constants were calculated from the linear fit (eq.26, 27) (Figure 36, black bars). The rate constants for the thermally induced cyclization of the CMTE were found to be reduced by 78% for PS-PS and 58% for PBA-PS particles compared to the seed particles from miniemulsion polymerization but are still of the same magnitude (Figure 36). An undesired back-switching to the initial state was not observed for PS–PS colloids in the timeframe of the experiment (12 days), thus underlining the excellent stability of the photo-states when incorporated in polymer particles.

### **6.3.3. Self-Assembly of Photoswitchable Colloids at the Air-Water Interface into Complex Binary Monolayers**

The optical properties of photoswitchable colloids were investigated and an excellent thermal stability for the on/off states in all cases was successfully shown. For the creation of a model system for data storage or light erasable barcoding the colloids needed to be precisely located in defined positions. This can be realized using the self-assembly approach of colloids at the air–water interface of a Langmuir trough into two dimensional highly ordered colloidal monolayers. The primary colloids with a size distribution of  $\sigma > 15\%$  were

not suitable for the production of high quality colloidal monolayers. Therefore, larger particles were produced by seeded emulsion polymerization with a narrower size distribution of  $\sigma = 9\%$  (PS-PS particles) and  $\sigma = 12\%$  (PBA-PS) (Table 9). If the size distribution is too broad, the particles cannot form a hexagonal lattice and the arrangement at the interface is disturbed. Another possibility to create highly ordered monolayers is the formation of a binary colloidal structure. Thus, two differently sized particle systems are co-assembled at the air-water interface. Here, the larger particles serve as template and form a hexagonal densely packed lattice whereby the smaller particles are located at the interstices of the larger template particles. The size of the interstitial sites depends on the contact angle of the colloids at the air-water interface and the immersion depth.

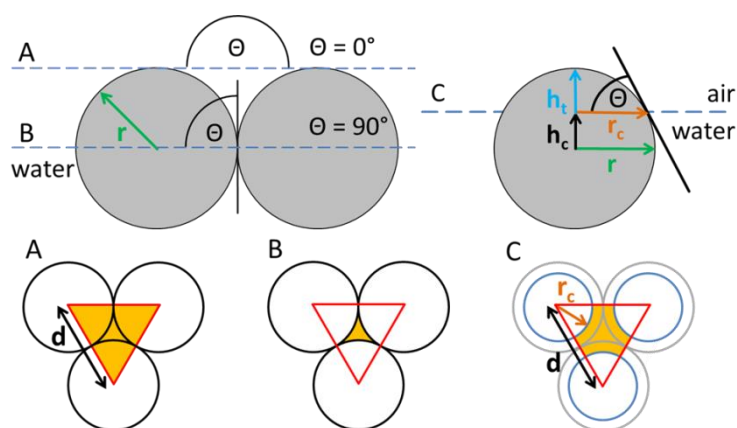


Figure 39 Determination for the size for the interstitial sites' area (orange) of binary monolayers provided by the large particles at the air-water interface depending on the contact angle  $\Theta$ : A)  $\Theta = 0^\circ$ , colloids are completely immersed into the aqueous phase yielding the maximum area for the smaller particles to be located at, B)  $\Theta = 90^\circ$ , the particles are half immersed with the depth in the range of particle radius yielding the minimum area for the small particles, C)  $\Theta$  between 0 to  $90^\circ$ , the particles are partly immersed into the aqueous phase.<sup>[103]</sup>

If the particles had a hypothetical contact angle of  $0^\circ$  (Figure 39A), they would be completely immersed in the aqueous phase of the air-water interface. This scenario is physically impossible because the particles will not adhere to the air-water interface. It provides, however, the hypothetical upper limit for the area/volume in the interstitials. At a contact angle  $\Theta = 90^\circ$  (Figure 39B) the colloids are half immersed in the aqueous phase with a depth in the range of the particle radius. Thus, the gap size for the small particles is minimal. If the contact angle for the large particles differs from the minimum or maximum case the profile of the interstitial site changes (Figure 39C).

In Figure 39,  $r$  is the radius,  $d$  the diameter,  $\Theta$  the contact angle,  $r_c$  the radius of the particles with a contact angle  $0 < \Theta < 90^\circ$  and an immersion depth  $h_c$  and  $h_t$  as the part of the large colloids which reaches out of the aqueous phase. The height  $h_t$  at a given contact angle *e.g.* of  $40^\circ$  for partially immersed particles can be calculated using (eq. 31, 32). At a given contact angle of  $40^\circ$  the height  $h_c$  is about

$$h_c = r \cdot \cos(\Theta) = 440 \text{ nm (eq. 30)}$$

$$h_t = r - h_c = 135 \text{ nm (eq. 31)}$$

$$h_c = \sqrt{2rh_t - h_t^2} = 370 \text{ nm (eq. 32)}$$

The new profile of the interstitial sites, where the smaller particles are located, can be described as a triangular area whereas the corners were cut off by circular segments with radius  $r_c$  (Figure 40, orange area):

$$x = D - 2r_c = 410 \text{ nm (eq. 33)}$$

Carboxylated polystyrene particles of about  $D = 1150 \text{ nm}$  were used within the experiments as template to create localized and defined nano-pixels from the particles with photoswitchable emission. The smaller seeded colloids are located in the interstices of the resulting hexagonal lattice of the large particles. Therefore, it was possible to create binary colloidal crystals of high ordering quality, which can be seen in the resulting scanning electron micrographs (Figure 41A and D). These two dimensional crystals have domain sizes of several hundreds of  $\mu\text{m}^2$ .

The evaluation for the possible particle assignments of the seeded particles at the interstitial sites was done geometrically by assumption of the particle's contact angle of  $40^\circ$  at the air-water interface at  $\text{pH} = 7$  considering equations 5 to 8. As the particles have a size distribution of about  $\sigma = 9\%$  for the seeded polystyrene particles and  $\sigma = 12\%$  for the seeded poly(butyl acrylate) particles the standard deviation  $\sigma$  of the Gaussian fit for the determination of the particle size can be used to describe the particle sizes as  $s$  (diameter  $d - \sigma$ ),  $m$  ( $d$ ) and  $L$  (diameter  $d + \sigma$ ) (Figure 42 and Figure 43) measured by photon cross correlation spectroscopy. The occurring arrangements were analyzed using the scanning electron micrographs of the binary colloidal monolayer for both hybrid particle systems.

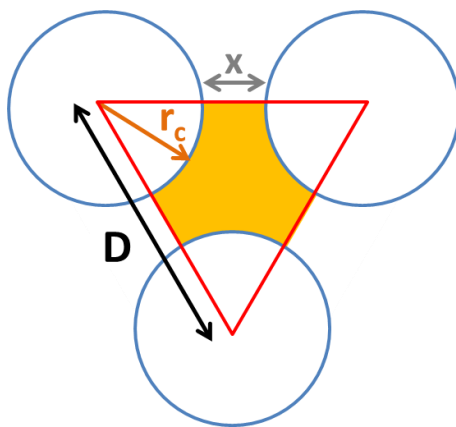


Figure 40 Sketch for the area of the interstitial sites partially immersed into the aqueous phase at the air-water interface with radius  $r_c$ , diameter  $D$  and distance  $x$  depending on the contact angle of the colloids.<sup>[103]</sup>

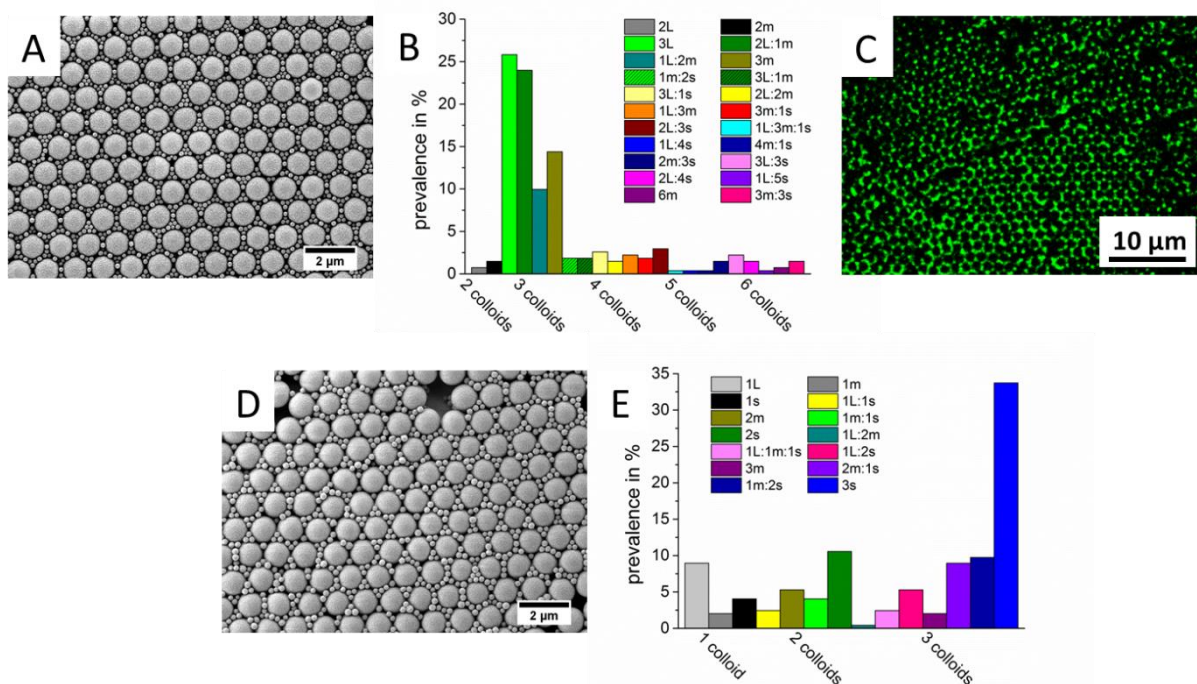


Figure 41 (A) SEM image of an ordered binary colloidal monolayer with  $D = 1150$  nm template colloids and photoswitchable PS-PS seeded particles with a number ratio of  $N_{large}/N_{small}$  of 1:6 and (B) the corresponding statistical analysis for the possible arrangements of the smaller photoswitchable colloids located in the interstitial positions, (C) confocal laser scanning micrograph of a binary monolayer from seeded PS-PS particles shown in (A), (D) SEM image of a binary monolayer with  $D = 1150$  nm template colloids and small photoswitchable PBA-PS seeded particles with a number ratio of  $N_{large}/N_{small}$  of 1:6 and (E) the statistical analysis for the monolayer shown in (D) for PBA-PS colloids.<sup>[103]</sup>

The most frequently occurring arrangements are shown in Figure 42 for seeded polystyrene and in Figure 43 for the seeded poly(butyl acrylate) particles. The size of the interstitial gaps between the particles was calculated as described before and the seeded PS–PS and PBA–PS particles correlated with the size of the gaps. The resulting geometries were distinguished and identified in the scanning electron micrographs (Figure 41A and D). The number ratio of larger to small particles  $N_{large}/N_{small}$  was adjusted to 1:6 at the interface. The statistical evaluation of the binary monolayers shows a predominance of 3 colloids (76%) located in the interstitial positions for the PS–PS particles (Figure 41B), rather than the maximum arrangement of 6 colloids (up to 6%), which is also in agreement with the adjusted number ratio of  $N_{large}/N_{small}$  of 1:6 for template to photoswitchable particles. Figure 41E shows the statistical evaluation of the binary monolayer of template particles with photoswitchable PBA–PS colloids. As the PBA–PS particles are larger ( $D = 260$  nm) than the PS–PS particles ( $D = 191$  nm), the maximum number of particles for the co-localization at the interstitial site is a geometrical arrangement of 3 colloids (see Figure 43). The histogram shows again a predominance of 3 colloids (63%) located in the interstitial positions (Figure 41E). As can be seen in the scanning electron microscopy (SEM) images and from the statistical evaluation (Figure 41A, B, D and E) the binary colloidal monolayers tolerate a relatively broad size distribution of the smaller colloids located at the interstitial sites of the carboxylated PS template particles, without disturbing the high order of the template colloids. With the number ratio of large particles to small particles ( $N_{large}/N_{small}$ ) the configuration can be adjusted reliably, even with broadly distributed colloids.

The binary colloidal monolayer of non-fluorescent template PS particles and photoswitchable PS–PS particles was also investigated by confocal laser scanning microscopy. The corresponding CLSM image (Figure 41C) shows a very high degree of ordering, where the larger template colloids are arranged in a hexagonal lattice (dark spots) and the interstitial sites are filled with the smaller fluorescent seeded particles (green spots). Therefore, it would be possible to address one single interstitial site as a nano-pixel in a very efficient and defined way because of the high crystallinity of the functional colloidal monolayer.

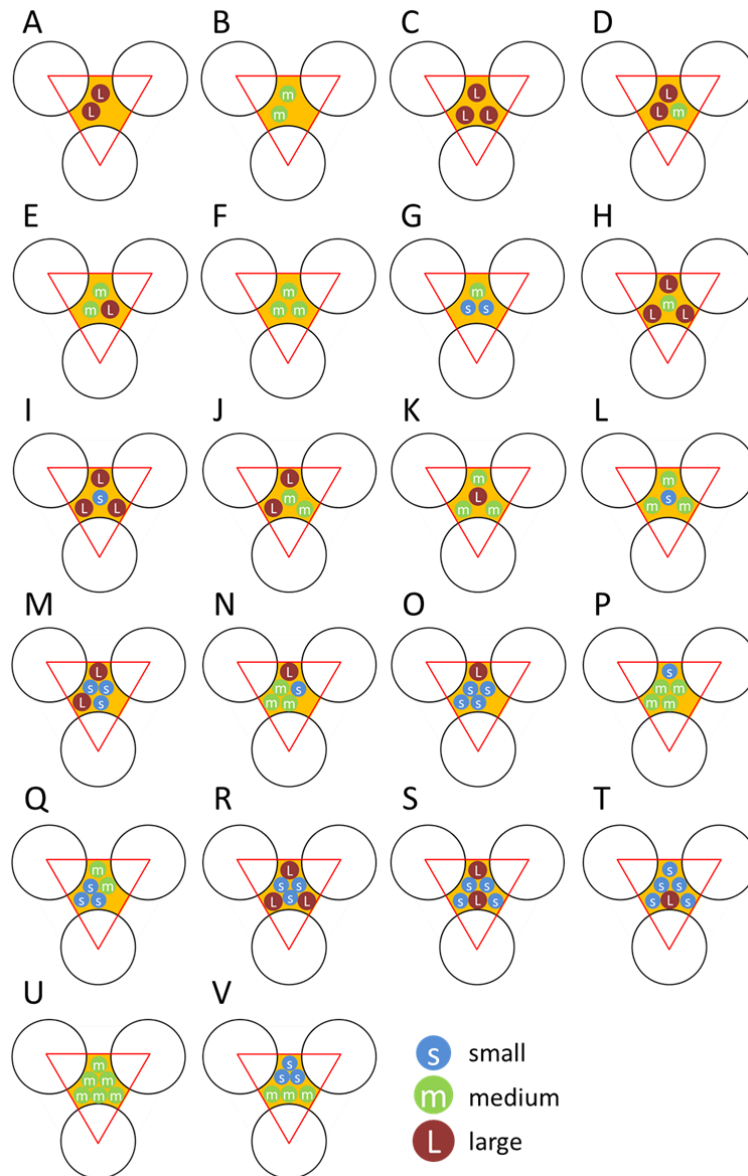


Figure 42 Observed arrangements for the small seeded polystyrene particles at the interstitial sites of partially immersed larger colloids ( $D = 1150$  nm) co-assembled as a binary monolayer A and B) for two particles of size m and L, C to G) for three particles as single particle sizes or in combination, H to L) for four particles at the interstitial site as combinations of all occurring sizes, M to Q) for five particles in combination with a hole and R to V) for six particles of single size or in combination.<sup>[103]</sup>

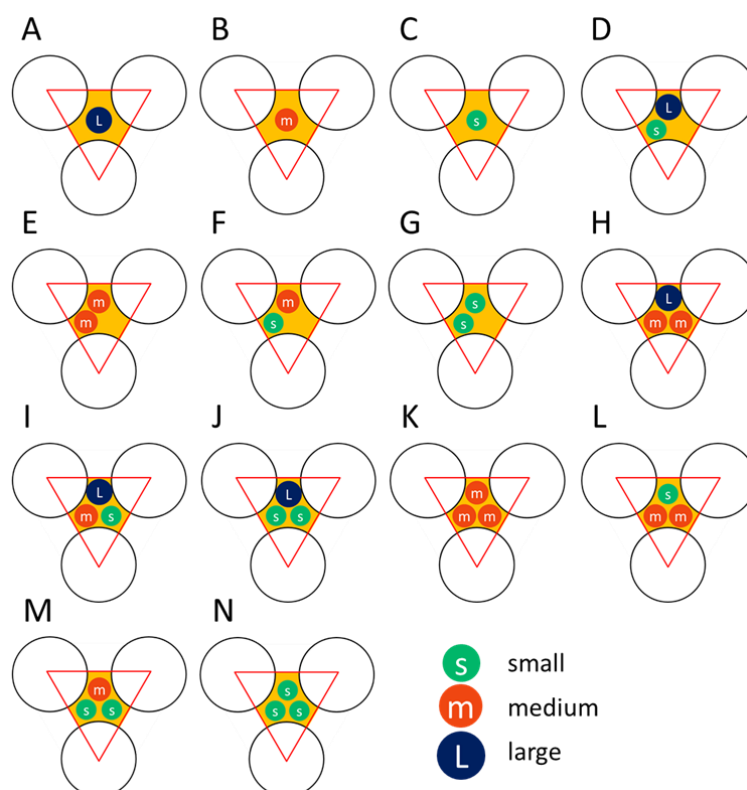


Figure 43 Observed arrangements for the small seeded poly(butyl acrylate) particles at the interstitial sites of partially immersed larger colloids ( $D = 1150$  nm) co-assembled as a binary monolayer A, B and C) for one particle of size s, m and L, D to G) for two particles with all sizes and in combination with a hole, H to N) for three particles at the interstitial site as combinations of all occurring sizes.<sup>[103]</sup>

### 6.3.4. Photoswitching in Colloidal Monolayers

The successful use of a colloidal monolayer to reversibly store (and erase) information with light is shown. An optical fluorescence microscope was used for the investigation of the photoswitching of the colloidal monolayer. As colloids photoswitchable poly(butyl acrylate) particles were self-assembled at the air water interface and transferred onto a substrate. The substrate was first irradiated with visible light to obtain the ring-open state of the CMTE and the highest possible fluorescence intensity of the colloidal particles (Figure 44A).

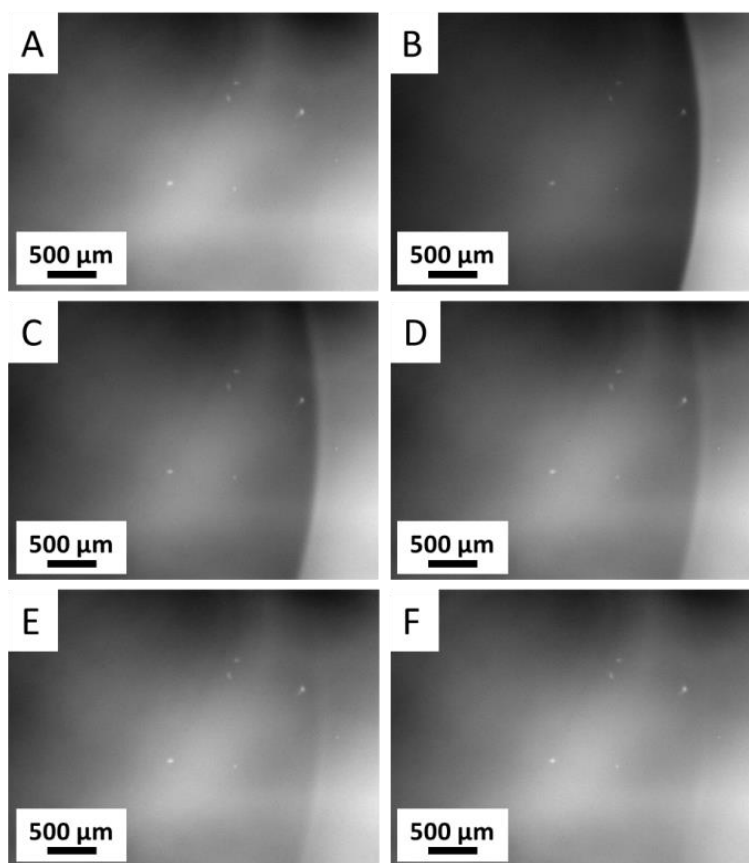


Figure 44 Optical micrographs of a monolayer from photoswitchable PBA colloids using a fluorescence microscope with an 2.5x objective and different optical filters (DAPI-filter,  $\lambda_{ex} = 360$  nm and  $\lambda_{em} = 420$  nm and eGFP-filter,  $\lambda_{ex} = 472$  nm and  $\lambda_{em} = 520$  nm) (A) after irradiation with VIS-light for 5 min using the eGFP-filter, (B) after irradiation with UV-light for 5 min using the DAPI-filter (circular part of the monolayer), (C) after excitation with VIS-light at  $\lambda_{ex} = 472$  nm for 120 ms (eGFP-filter), (D) after excitation for 180 ms, (E) after excitation for 240 ms and (F) after excitation for 300 ms.<sup>[103]</sup>

Afterwards, parts of the substrate were exposed to UV-light to induce the photocyclization reaction of the CMTE into the ring-closed state, whereas the fluorescence emission of the fluorophore is absorbed and the fluorescence is switched off in the exposed areas (Figure 44B). Irradiation with visible light can be used to reversibly erase the stored information (Figure 44C to F). After illumination for overall 300 ms, a complete recovery of the fluorescence intensity in the monolayer was observed.

### 6.3.5. Conclusion and Outlook for Section 6.3.

In summary, an easy and fast method for the production of functional colloidal monolayers with reversibly photoswitchable nano-pixels was presented. The photoswitchable functional polystyrene and poly(butyl acrylate) colloids were synthesized using the miniemulsion polymerization process to incorporate the appropriate dye system based on a perylene as a fluorophore (PMI, *N*-(2,6-diisopropylphenyl)-perylene-3,4-dicarboximide) and a bis-arylethene as a photochrome (CMTE, *cis*-1,2-dicyano-1,2-bis-(2,4,5-trimethyl-3-thienyl) ethene). Thus, addressable photoswitchable entities were generated. The light-induced switching of the fluorescence intensity of the fluorophore via selectively enabling and disabling energy transfer to the photochrome molecule in the confined environment of a colloidal particle was investigated in detail. The incorporated dye system still shows a wavelength range ( $\lambda > 620$  nm) where the fluorescence emission of the fluorescent dye (PMI) cannot be absorbed by the excited isomer of the photochromic dye (CMTE). Because of the residual emission, the particle cannot be completely switched off. To achieve this, either the photochromic dye can be modified by introducing functional groups at the thienyl side groups or at the ethene itself in form of a functional side chains.<sup>[177]</sup> The other possibility would be to modify or exchange the fluorescent dye by a dye whose fluorescent signal can be completely absorbed by the photochrome meaning  $\lambda_{em}$  should be shifted to smaller wavelengths. The only requirement for the new dye system must be the easy readout and excitation by a conventional lasers or LED irradiating light of distinct wavelengths.

Moreover, the thermal stability of the excited state of the photochrome can be increased by a factor of more than 20 compared to the stability in solution by embedding the dyes in a polymeric matrix of colloids. Information stored in the colloids by the photoswitching process can thus be retained over at least several days at room temperature without risking of degradation by uncontrolled cycloreversion reactions. The precise incorporation of defined amounts of the dye molecules into polymeric matrices by miniemulsion polymerization can be used to optimize the quenching of the fluorophore emission. But, concerning the persistence of the single excited states of the photochrome further absorption and fluorescence emission measurements should be done. The lifetime of the ring-closed isomer of the photochrome for instance might be increased by cooling the

irradiated colloids or the monolayer, thus the thermally induced reverse ring opening reaction can be suppressed even further. Heating of the colloids in contrast could accelerate the ring opening cyclization to erase the stored information faster.

The light-induced switching of fluorescence is completely reversible over several cycles without observation of major fluorescence intensity loss. But the number of alternating irradiation switching cycles should be increased to proof the overall persistence of the dye system and the stability against photobleaching. Moreover, the small broadly distributed colloids from miniemulsion polymerization were covered with a polystyrene protection shell by seeded emulsion polymerization resulting larger particles of narrower size distribution. With the seeding process the thermal stability of the excited photochrome isomer at room temperature could be also increased by almost more than 50%.

Functional colloidal monolayers were prepared using the co-assembly method of colloids of two distinct sizes at the air–water interface. The obtained binary monolayers of functional seeded particles and plain larger particles showed high crystallinity of several hundreds of  $\mu\text{m}^2$  resulting a high addressability of the functional colloids. The possible arrangements for the seeded particles located at the interstices of the hexagonally ordered template particles were assessed from the scanning electron micrographs, resulting in a preferred number of three particles at the interstices for the seeded polystyrene as well as for the seeded poly(butyl acrylate) particles. The preparation method of functional binary monolayers offers the possibility to self-assemble colloids with broad size distribution into highly ordered hexagonal lattices. Therefore, even single particles or smaller particle arrangements can be addressed. For the preparation of large-scale binary photo-responsive colloidal monolayers the co-self-assembly process should be improved to result higher crystallinity on bigger length-scales. Very important is the attentive sample preparation and the right adjustment of the particle number ratio  $N_{large}/N_{small}$ . Further, the pixel distance and the pixel size can be adjusted by variation of the template particle size and the number ratio of large to small particles ( $N_{large}/N_{small}$ ). Using smaller particles decreases the distance between the interstitial sites and therefore the interspace of the nano-pixel formed by the photoswitchable particles. The pixel size can be easily reduced by decreasing number of small particles ( $N_{large}/N_{small}$  increased) whereby an increase of  $N_{small}$  generates bigger nano-pixels.

The reversible optically induced storage and elimination of information in such monolayer structures was demonstrated successfully. This technology is envisioned to be of broad interest in information technology as it provides a cheap, simple and efficient way to generate precise substrates for optical manipulation at micro- and nanoscale.

#### **6.4. Colloidal pH Sensors for the Visualization of pH Dependent Processes in Cells**

This section is based on the publication “Nanoprobing the acidification process during intracellular uptake and trafficking” by S. Lerch, S. Ritz, K. Bley, C. Messerschmidt, C. K. Weiss, A. Musyanovych, K. Landfester and V. Mailänder published 2015 in *Nanomedicine: Nanotechnology, Biology and Medicine*, Volume 11, Issue 6, Pages 1585–1596. The publication is reprinted by permission from Elsevier.<sup>[178]</sup>

In the last sections colloids and their self-assembled structures were investigated concerning locally confined physico-chemical properties such as contact angles and particle interactions directly at the air-water interface during self-assembly processes. It was also shown how optical properties can be modified by using functional stimuli-responsive materials and controlled particle interactions to form light-switchable pixels in the nano- and micrometer scale with high localized resolution.

This chapter focusses on the environmental interaction of stimuli responsive nanoparticles not at the air-water interface but during interaction with cells. The path of nanoparticles or nanocapsules through cells can be monitored by using pH-responsive nanoparticles. Such polymeric nanosensors have been developed as probes for real-time imaging and dynamic monitoring of various ions such as  $H^+$ ,  $Ca^{2+}$ ,  $Mg^{2+}$ ,  $K^+$ ,  $Na^+$ , and  $Cl^-$ , which are important for cellular metabolism.<sup>[179-182]</sup> Nanoparticle based sensor systems have several advantages in comparison to highly invasive methods, like *e.g.* microelectrode probing or the use of unconjugated single fluorescent probes: i) due to their small size and inert material they are physically and chemically less-invasive than macroscopic probes, ii) the local concentration and therefore signal strength of the chemical probe can easily be tuned due to the high surface-to-volume ratio<sup>[183]</sup> and iii) surface functionalization as targeting agents may lead

them towards specific sites at or in cells. Nanoparticles have emerged as promising tools to study mechanisms innate to cells such as endocytotic uptake machineries as well as to function as novel delivery systems for drug transport and for addressing specific cell or tissue types. Most nanoparticles are taken up by cells via various endocytotic mechanisms and follow the endo/lysosomal pathway.<sup>[184]</sup> The pH of these compartments is lowered during the maturation of the vesicles - from early to late endosomes to lysosomes - to trigger the release of receptor-bound ligands,<sup>[185]</sup> or to digest debris or nutrients. This acidification can be used to trigger the prospective nanocarriers to release their payload at a distinct position inside the cell<sup>[186]</sup> which can be useful for drug delivery applications in nanomedicine.

In this work polymeric nanoparticles were synthesized and functionalized with a pH sensitive dye. The physico-chemical properties were investigated in detail and pH responsiveness of the dye and the functionalized nanoparticles were evaluated by UV-Vis spectroscopy. The cell experiments and investigation of the nanoparticles' pathway through the cells by confocal laser scanning microscopy were performed by [REDACTED]. Transmission electron microscopy was measured by [REDACTED].

#### **6.4.1. Concept for the Visualization of Time-Dependent pH Processes inside Cells by Functionalized Nanoparticles**

Many colloid based drug delivery approaches rely on a detailed knowledge of the acidification process during intracellular trafficking of endocytosed nanoparticles. Therefore, a nanoparticle based pH-sensor can be constructed composed of a simple polymeric nanoparticle with surface active groups and a pH sensitive dual wavelength fluorescence emitter which is stimulated by varying pH environments. Here, time-dependent pH processes in cells can be monitored by fluorescence microscopy imaging. A requirement for the pH responsive nanoparticles is the non-toxicity for the intercellular applications. Therefore, it is beneficial to prepare nanoparticles without using any surfactant. The emulsifier free emulsion polymerization is the appropriate technique as nanoparticles with narrow size distribution and a high surface group density can be generated without usage of additional surfactants.<sup>[21]</sup> Semaphthorhodafluor-1 (carboxy SNARF-1, Figure 45A) as well-known commercially available dual-wavelength emitter serves as pH sensitive dye, can be

easily coupled as succinimidyl activated ester (SNARF-1-NHS, Figure 45C) with amine functionalities on the particle surface (Figure 45C).

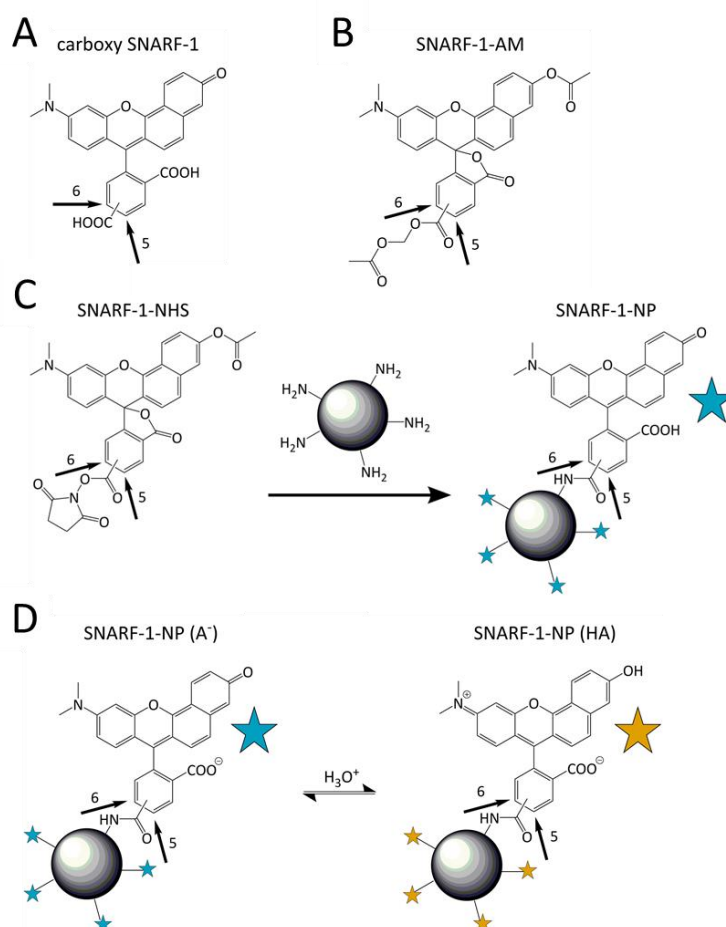


Figure 45 (A) Free dual wavelength dye carboxy SNARF-1, (B) ester protected dye acetoxymethyl ester acetate (SNARF-1-AM) (C) coupling of the pH sensitive dye carboxy SNARF-1-NHS onto amine functionalized nanoparticles, (D) switching between deprotonated (A-) and protonated (HA) form of the dye molecules coupled onto particles (SNARF-1-NPs) by shifting the pH value from basic to acidic.<sup>[187]</sup>

The SNARF-1-NHS is then covalently bound to the particle surface by creation of an amide bond between the carbonyl group of the dye and amine groups of the nanoparticles. The SNARF-1-NPs are able to change their fluorescence emission wavelength upon pH variation. There are two forms of the dye molecule as can be seen in Figure 45D, the deprotonated molecule in basic environments (A-) and the protonated form in acidic environments (HA) that show different emission maxima at  $\lambda_{em, HA} = 580 \text{ nm}$  and  $\lambda_{em, A^-} = 640 \text{ nm}$ . Such NPs with an accessible probe dye can be used as nano-sensors for intracellular and intravesicular

time-dependent pH process monitoring as the color of these nanoparticles changes with time (Figure 46). The local pH changes during nanoparticle transport in cells can therefore be easily visualized by fluorescence microscopy. The results of such processes can be used to design for instance nanocarriers loaded with drugs or any other targets with controllable pH responsive release mechanisms.

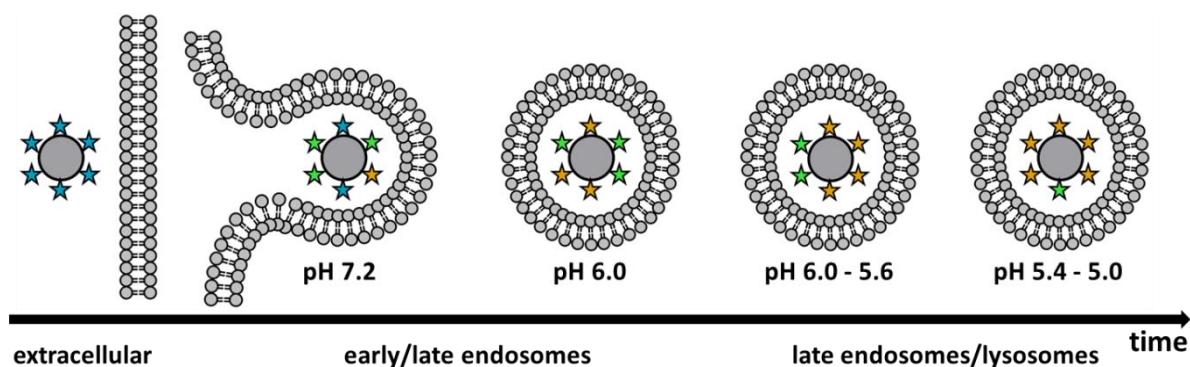


Figure 46 Schematic concept for the enlightening of time-dependent pH processes inside cells for *e.g.* the design of nanoparticular drug carriers with pH sensitive release mechanism.<sup>[187]</sup>

#### 6.4.2. Coupling of the pH-Responsive Dye SNARF-1-NHS onto Amine Functionalized Nanoparticles

Positively charged amine functionalized polystyrene nanoparticles as carriers for the pH responsive dye SNARF-1-NHS were synthesized by soap-free emulsion copolymerization in the presence of the comonomer amino-ethyl methacrylate hydrochloride (AEMH) following the procedure of Ganachaud *et al.*<sup>[188, 189]</sup> After purification, the average particle size and size distribution were measured by angle-dependent dynamic light scattering resulting a hydrodynamic radius ( $R_h$ ) of  $R_h = 61$  nm (Figure 47A) or particle diameter of  $D = 122 \pm 8$  nm, respectively. Figure 47B shows a scanning electron micrograph of the amine functionalized uniformly distributed polymeric particles.

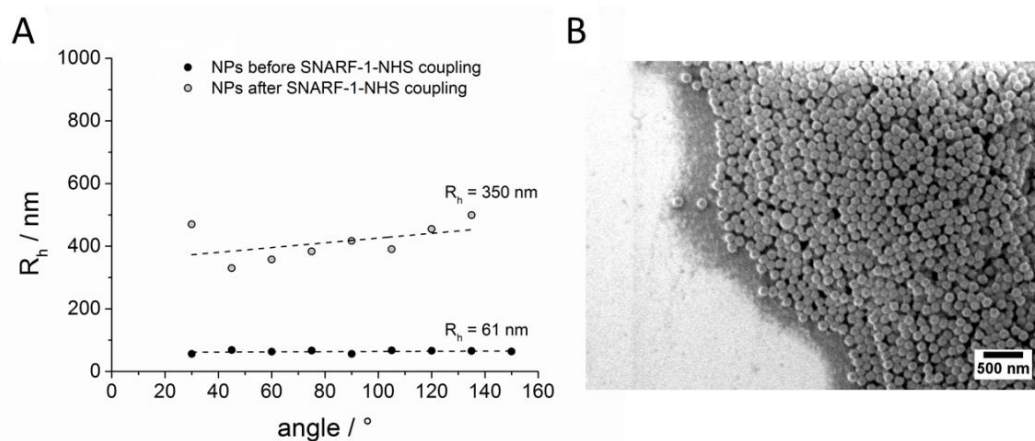


Figure 47 (A) Diagramm of the hydrodynamic radii ( $R_h$ ) of nanoparticles before and after coupling of the pH-responsive dye SNARF-1-NHS versus the light scattering angle, (B) SEM image of the amine functionalized nanoparticles prepared by soap-free emulsion polymerization.<sup>[187]</sup>

The surface properties of the colloids were further characterized. A positive zeta-potential of  $45 \pm 6$  mV was measured and the number of amine groups on the particle surface was determined using the fluorescence assay<sup>[188]</sup> described in chapter 7.4 resulting  $1.5 \cdot 10^{-5}$  mol·mL<sup>-1</sup> or 2.5 amine groups per nm<sup>2</sup>.

Furthermore, the amine functionalized nanoparticles were coupled with carboxy SNARF-1-NHS and used to create nanoparticular pH sensors. The covalent coupling created an amide bond between the esterified carbonyl group of the dye and the amine group on the particle surface (SNARF-1-NP) as shown in the reaction scheme (Figure 45C). The zeta-potential of the dye coupled SNARF-1-NPs decreased from  $45 \pm 6$  mV to  $19 \pm 5$  mV which confirmed a decrease of positively charged groups on the particle surface. The determination of remaining amine groups on the particle surface after coupling with SNARF-1-NHS by fluorescamine assay was not possible because the fluorescence emission of the fluorescamine at  $\lambda_{em} = 470$  nm is absorbed by the SNARF-1 dye molecules ( $\lambda_{ex} = 488$  nm and  $\lambda_{ex} = 514$  nm) resulting no detectable signal. The particle size after dye coupling was measured again with angle-dependent dynamic light scattering resulting an average particle diameter of  $R_h = 350$  nm (Figure 47A). An explanation for such an increase in particle size can be the destabilization of the particle dispersion by reduced electrostatic repulsion and by charge shielding of the coupled dye onto the particle surface. Additionally to reduced

interactions between the amine groups also increased attractive interactions between the amine groups of the particles and the carboxylic acid functions of the SNARF-1 molecules can appear. But also the enormous dilution for DLS measurements can lead to destabilization and aggregation of the particle dispersion. In buffer systems such as used for confocal laser scanning microscopy or either in cell culture medium no aggregation was visible. From similar experiments with comparable particles prepared by miniemulsion polymerization a size increase of about 2 nm was measured.<sup>[190]</sup> The essential difference between the particles prepared by miniemulsion and the ones synthesized by soap-free emulsion polymerization is the usage of surfactants. The colloids from miniemulsion polymerization were additionally stabilized with the non-ionic surfactant Lutensol AT50 which leads to less aggregation after dye coupling and throughout DLS measurements.

To ensure that the fluorescent properties of the dye are not altered by the coupling and washing procedures, the fluorescence spectra of the free dye carboxy SNARF-1 and of SNARF-1-NPs were measured in buffers with different pH values (pH 4.5 – pH 8.5, Table 10). Upon excitation, the protonated form (HA) in acidic environment emits light at a lower wavelength than the deprotonated form (A-) in basic environment (Figure 45B). Thus the pH value can be calculated from the intensity ratio (HA/A-) of the two emission wavelengths of the protonated and deprotonated form.

Figure 48 display the pH-dependent emission spectra of the free carboxy SNARF-1 dye (A) and of the SNARF-1-NHS ester coupled onto the particle surface (B, SNARF-1-NP)). Figure 48 show the ratios of the protonated (HA) and deprotonated (A-) emission maxima of the free dye (SNARF-1, C) and SNARF-1-NP (D) obtained by integrating the spectra over a fixed wavelength.

Table 10 Potassium rich and carbonate-free buffer systems for pH calibration (specification for 500 mL demineralized water.

pH	KCl / g	FCS <sup>1)</sup> / g	MgCl <sub>2</sub> · 6 H <sub>2</sub> O / g	HEPES <sup>2)</sup> / g	MES <sup>3)</sup> / g	Bicine / g	Citric acid · 1 H <sub>2</sub> O / g	Na <sub>2</sub> HPO <sub>4</sub> · 2 H <sub>2</sub> O / g
4.6	4.8	5.0	-	-	-	-	5.6	8.2
5.0	4.8	5.0	-	-	-	-	5,1	9.1
5.5	4.8	5.0	0.2	-	3.0	-	-	-
5.75	4.8	5.0	0.2	-	3.0	-	-	-
6.0	4.8	5.0	0.2	-	3.0	-	-	-
6.4	4.8	5.0	0.2	-	3.0	-	-	-
6.6	4.8	5.0	0.2	-	3.0	-	-	-
6.8	4.8	5.0	0.2	-	3.0	-	-	-
7.2	4.8	5.0	0.2	3.6	-	-	-	-
8.0	4.8	5.0	0.2	-	-	2.4	-	-

<sup>1)</sup> Fetal calf serum (FCS), <sup>2)</sup> 4-(2-hydroxyethyl)-1-piperazineethanesulfonic acid (HEPES), <sup>3)</sup> 2-N-morpholino ethanesulfonic acid (MES).

The ratios (HA/A<sup>-</sup>) of both free dye and dye-coupled nanoparticle conjugates are equal and linear in the range from pH 6.8 to pH 8.0. However, the emission of the free dye differs from the NP-coupled dye for pH values below pH = 6.8. Possible reasons can be the repulsion of H<sup>+</sup> ions from the positively charged particle surface lowering the local pH as has been shown in more detail by others groups.<sup>[191]</sup> Förster resonance energy transfer (FRET) may also occur between protonated and deprotonated SNARF-1 on the NP surface. The average distance between the dye molecules after coupling onto the nanoparticle surface is lowered to the nanometer scale which may allow energy transfer between the protonated und the deprotonated form to occur.

Furthermore, the photo-physical properties of SNARF-1 may be altered through the presence of cellular components.<sup>[192]</sup> Nevertheless, it can be concluded that carboxy SNARF-1 still preserved its pH responsiveness after the coupling process.

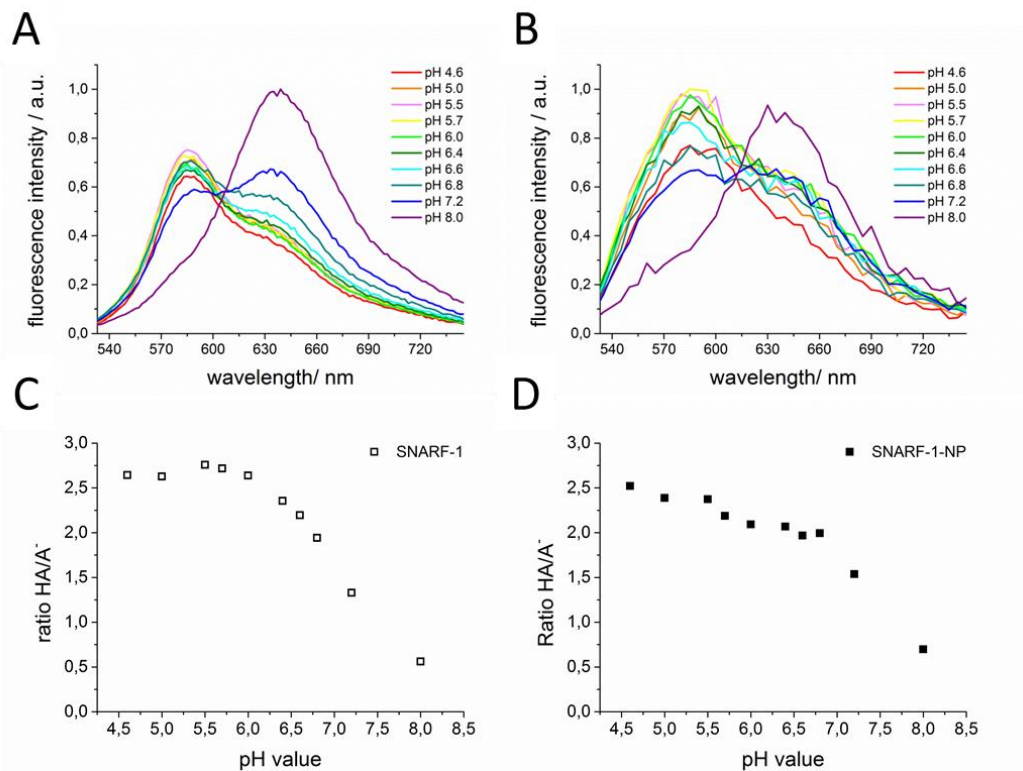


Figure 48 Fluorescence emission spectra of (A) carboxy SNARF-1 dye and (B) SNARF-1-NPs at different pH values,  $\lambda_{ex} = 514$  nm, (C, D) ratios of emission integrals obtained from fluorescence spectroscopy of protonated ( $\lambda_{em, HA} = 550 - 610$  nm) and deprotonated ( $\lambda_{em, A^-} = 640 - 720$  nm) emission range for the (C) SNARF-1 dye and (D) SNARF-1-NPs ( $\lambda_{ex} = 514$  nm).<sup>[187]</sup>

### 6.4.3. Intracellular pH calibration

An intracellular pH calibration was performed by Dr. Sandra Ritz with the CLSM cell imaging, because the fluorescent properties of carboxy SNARF-1 can be altered in the presence of proteins or other cellular components.<sup>[192]</sup> Therefore, HeLa cells were loaded with SNARF-1 acetoxymethyl acetate ester (SNARF-1-AM) or SNARF-1-NPs and treated with buffers of different pH values (Table 10). The (AM) esters of the fluorescent dye SNARF-1 (Figure 45C) are typically non-fluorescent because the extent of the delocalization in the aromatic structure is reduced by esterifying the naphthol hydroxyl group. The AM ester is hydrophobic and therefore able to cross the cell membrane. Once the molecule is inside the cytoplasm, the ester bond is cleaved by unspecific esterases. The polar free form of the dye is no longer able to cross the membrane barrier and trapped inside the cell. The extra- and intracellular pH values were equilibrated with the ionophores nigericin and valinomycin,<sup>[193]</sup>

<sup>194]</sup> which drive the cell membrane to be permeable to  $H^+/K^+$ . However, it is reported that the intracellular pH does not fully adjust to the extracellular pH values in nigericin containing high  $K^+$  saline buffer, but deviates by  $-0.12 \pm 0.02$ , <sup>[195]</sup> which must be considered as an additional calibration error. The intracellular pH was found to be stable after the addition of ionophores within approximately 100 s. To prevent severe toxic effects of the ionophores to the cells, which may lead to the cell membrane rupture and release of the trapped dye into the medium, measurements were performed within 5 min after the addition of ionophores and stabilization of the intracellular pH. A positive control of dye-loaded cells provided an intracellular pH of approximately  $pH = 7.2$ , which is consistent with the previously published values for HeLa cells. <sup>[196]</sup>

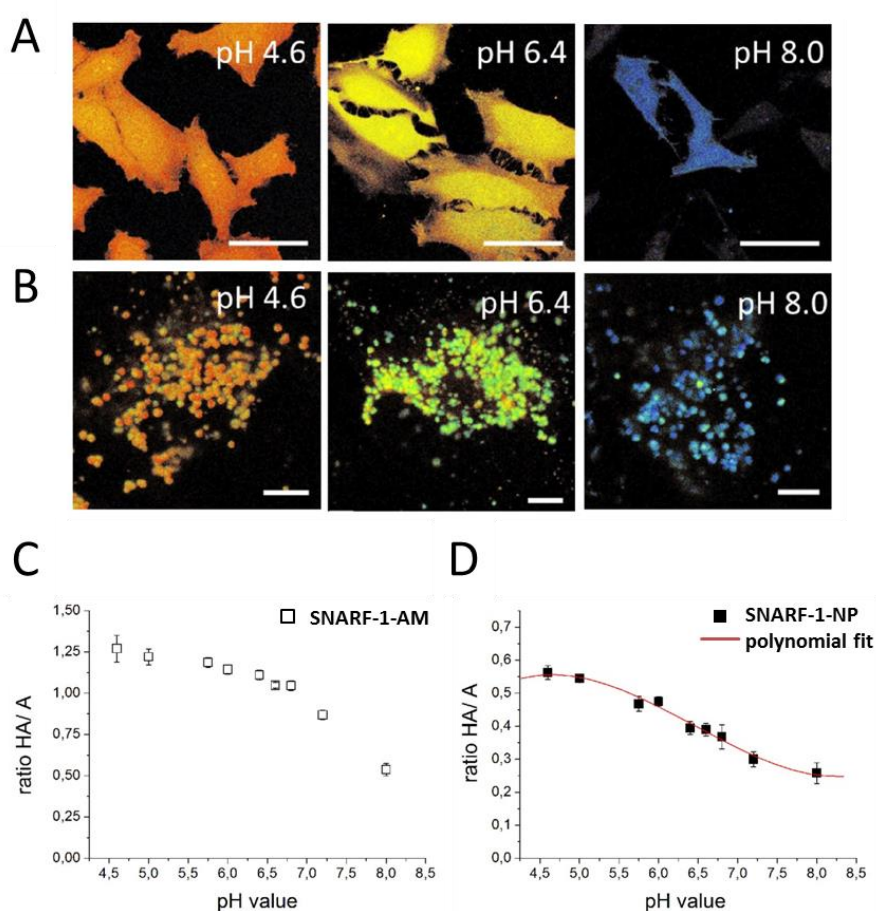


Figure 49 Intracellular calibrations for SNARF-1-AM and SNARF-1-NPs by fluorescence confocal laser scanning microscopy (CLSM) in HeLa cells. A) Representative pseudo-colored pH ratio images of the free SNARF-1-AM ester in the cytosol (scale bars 50  $\mu m$ ), (B) SNARF-1-NPs located in vesicular structures (scale bars 5  $\mu m$ ), (C, D) intracellular ratios of emission integrals obtained from CLSM imaging of protonated ( $\lambda_{em, HA} = 550 - 610$  nm) and deprotonated ( $\lambda_{em, A^-} = 640 - 750$  nm) emission range for the (C) SNARF-1-AM ester and for (D) SNARF-1-NP conjugates ( $\lambda_{ex} = 514$  nm). <sup>[187]</sup>

The free SNARF-1-AM ester was found to be homogeneously distributed in the cytoplasm of the cells (Figure 49A), whereas the SNARF-1-NPs were exclusively located in vesicular structures (Figure 49B). The pH dependent emission ratios ( $HA/A^-$ ) of the free SNARF-1-AM ester and SNARF-1-NPs were plotted in Figure 49C and Figure 49D. The calibration values of SNARF-1-NPs were fitted by a polynomial fit (Figure 49D), and the resulting equation was used to calibrate all further images. The intracellular calibration and the derived polynomial fit function allowed the detection of pH-dependent emission of SNARF-1-NPs in the range of pH 5.0 to pH 8.0. As this detectable pH range lies well in the range of pH changes seen both in the extracellular milieu and endo/lysosomal compartments, SNARF-1-NPs were considered to be an ideal sensor for acidification of NPs after endocytotic uptake into cells. Further, the particles were found to be non-toxic for the cells as evaluated by a cell viability test.

#### **6.4.4. Localization and Acidification of pH-Responsive Nanoparticles in Cells**

The time-dependent nanoparticle localization in living cells and their normal pH environment was monitored by applying the calibration fit function to CLSM images acquired after different incubation times (Figure 50) and measured by Dr. S. Ritz. Pseudo-colored CLSM images show the pH values of the particles in vesicular compartments of HeLa cells incubated with SNARF-1-NPs for 1, 2, 4, 6, 8 and 24 h (Figure 50A). 30 to 60 min after cellular uptake, an acidification of the NP environment was detected by quantifying the local pH with a maximal pH distribution of  $pH\ 5.8 \pm 0.2$ , which is in a typical range for early endosomes ( $\sim pH\ 6$ ).<sup>[197, 198]</sup> After 30 min the signal intensity was high enough for reliable detection.

At first, only few SNARF-1-NPs loaded compartments were observed (1 h); with increasing time, the number and size of vesicular compartments increased until equilibrium is reached after 4 - 6 h. For early time points (1 - 2 h) 'blue spots' ( $pH \geq 7.4$ ) confirmed the location of the SNARF-1-NPs on the exterior of the cell. Intracellular vesicular compartments with green, yellow and red pseudo-color have an acidic pH between pH 5.5 – 7.0, respectively, and are supposed to be endo/lysosomal structures.

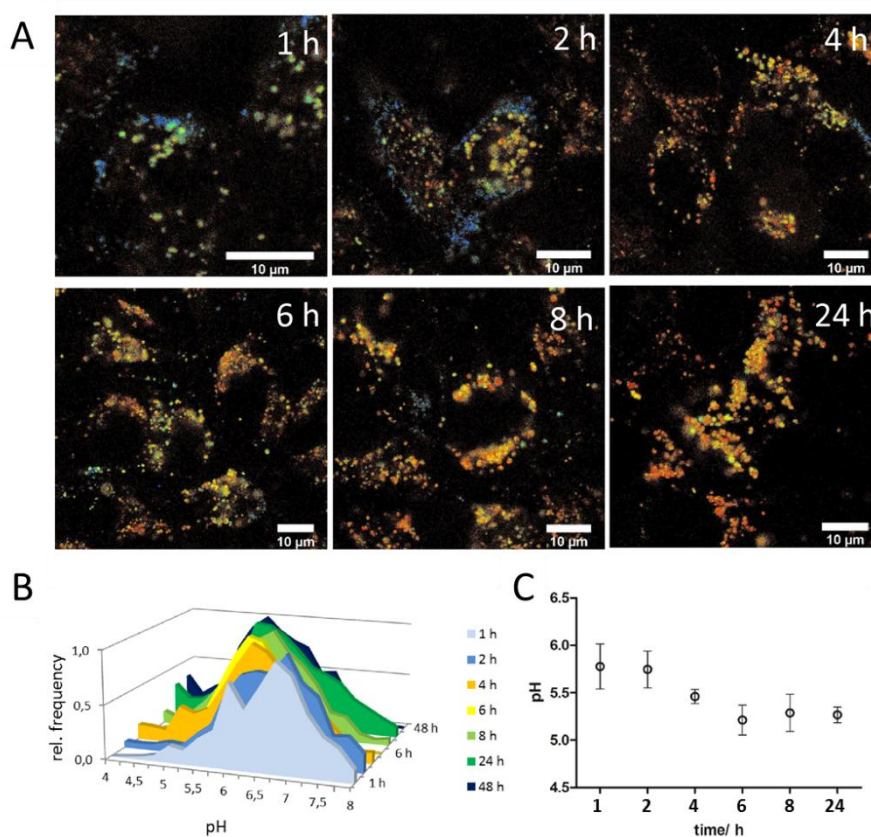


Figure 50 Time-dependent nanoparticle uptake and pH measurements with SNARF-1-NPs by fluorescence live cell CLSM in HeLa cells imaged after the indicated time points ( $\lambda_{ex} = 514 \text{ nm}$ ,  $\lambda_{em, HA} = 550 - 610 \text{ nm}$ ,  $\lambda_{em, A-} = 640 - 750 \text{ nm}$ ). (A) Representative pseudo-colored pH ratio images of SNARF-1-NPs located in vesicular compartments (bar scales  $10 \mu\text{m}$ ), (B) representative pH distribution in intracellular vesicular compartments calculated from one ratio image (ca. 5 cells) per time point, (C) time-dependent pH measurements of SNARF-1-NPs uptake. Mean value and standard deviation calculated from pH mean values from at least 10 ratio images per time point applying the calibration polynomial fit function.<sup>[187]</sup>

According to this, quantitative analysis of the pseudo-colored vesicular structures revealed a bimodal pH distribution with maxima around pH 6.8 and pH 6.0 for early time points ( $5.8 \pm 0.2$ , 1 - 2 h), which progressed to an equilibrium of  $\text{pH } 5.2 \pm 0.2$  after 4 - 6 h (Figure 50B, C). This pH equilibrium was constant for 48 h. The time course of the gradual acidification was plotted in Figure 50C. The data represent the mean value of 10 images per time point comprising roughly 5 cells per image and all vesicular structures in these cells.

TEM imaging done by C. Messerschmidt supported the endo/lysosomal localization of SNARF-1-NPs by displaying a distinct phospholipid layer around the particles which was

positively stained with osmium tetroxide. Such a phospholipid or protein corona respectively is subsequently formed by biomolecules upon contact with biological fluids (cell culture medium, blood) as well as the targeted cell type. Cluster of nanoparticles seen in the TEM images indicated that the fluorescence signals in the CLSM images occurred mostly from more than one nanoparticle. Electron micrographs visualized the SNARF-1-NPs uptake by c-shaped membrane ruffles typical for a macropinocytosis driven mechanism (Figure 51A). After 1 h, single SNARF-1-NPs or packages of  $\leq 5$  NPs surrounded by phospholipids were localized in the cytoplasm close to the plasma membrane (Figure 51B). Simultaneously, particle packages ( $\sim 5 - 10$  NPs) were located in perinuclear regions (Figure 51C).

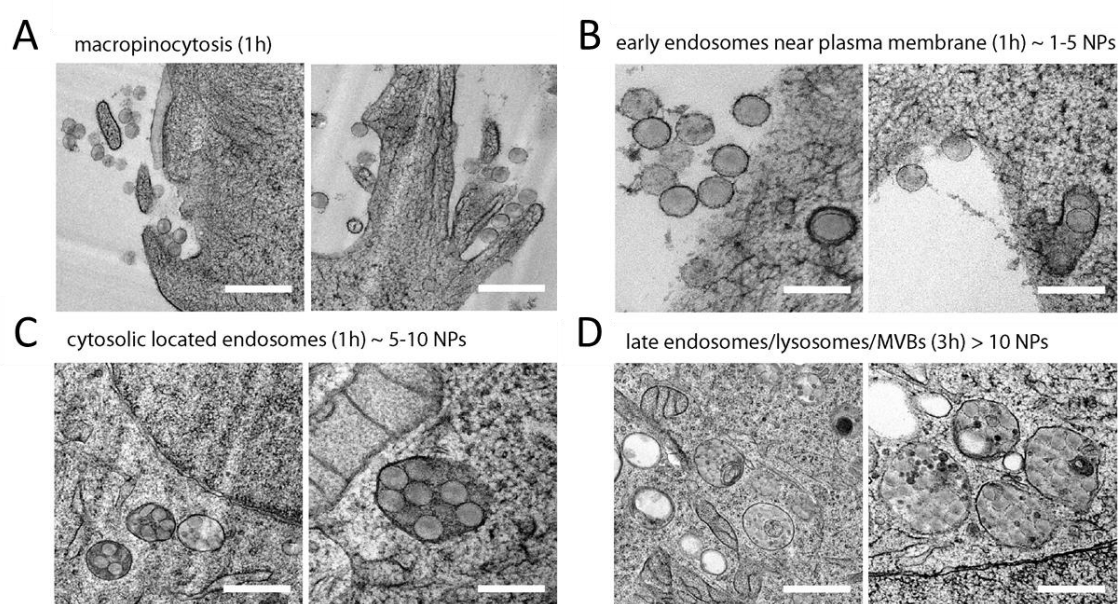


Figure 51 Transmission electron microscopy (TEM) images taken by C. Messerschmidt of SNARF-1-NP uptake in HeLa cells. HeLa cells were loaded with SNARF-1-NPs ( $0.3 \text{ g}\cdot\text{L}^{-1}$ ) and prepared for TEM imaging after 1 h and 3 h incubation time, MVBs (multi vesicular bodies), bar scales 300 nm.<sup>[187]</sup>

After 3 h, nanoparticles were identified in endosomal/lysosomal vesicles and densely filled multivesicular bodies ( $> 10$  NPs) (Figure 51D). This suggests a fusion of vesicular compartments containing NPs during the ripening process and an increased number of particles in clusters with increasing incubation time.

The proposed acidification processes of SNARF-1-NPs in HeLa cells was also supported by co-localization studies with fluorescent GFP-labeled endo/lysosomal Rab family proteins and live cell imaging. The Rab family of small GTPases is a major protein family regulating

intracellular trafficking and fusion of endosomal structures. Live cell imaging was performed with HeLa cells that were transiently transfected with the fluorescent Rab proteins 4a, 5a, 7 and 9, before supplying SNARF-1-NPs. Representative fluorescence images are shown in Figure 52 and Figure 53A. Rab4a is present in early endosomes and regulates recycling to the plasma membrane.<sup>[196]</sup> Rab5a is a marker for vesicle trafficking from the plasma membrane to early endosomes and homotypic fusion of early endosomes.<sup>[199]</sup> Rab7 accompanies transport from early endosomes via multivesicular bodies to late endosomes/lysosomes.<sup>[200]</sup> Rab9 is a marker for cycling between late endosomes and trans-Golgi network.<sup>[201]</sup>

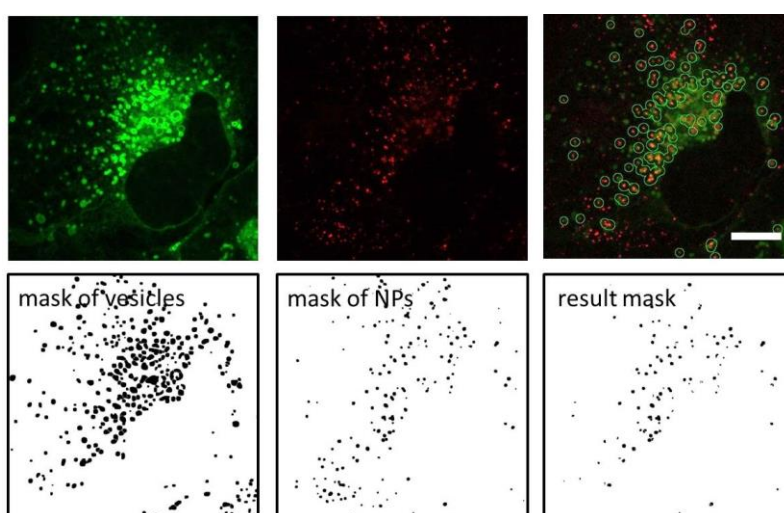


Figure 52 Exemplary images of co-localization between SNARF-1-NPs with GFP-Rab9 after uptake in HeLa cells (1 h). CLSM images (scale bar 10  $\mu\text{m}$ ) of single channels (GFP-Rab9, green, SNARF-1-NP, red) were semi-automatically filtered to select the vesicular structures and nanoparticles, and converted into binary masks displaying selected black objects on a white background. The binary masks were multiplied with each other to create a result mask displaying the NPs in vesicular structures. Rab9 is a marker for late endosomes and lysosomes.<sup>[187]</sup>

Quantitative image analysis revealed that after 1 h of incubation with nanoparticles, most of the SNARF-1-NPs were on the way from early to late endosomes and lysosomes indicated by co-localization with EGFP-Rab7 ( $70\% \pm 9.5\%$ ) and EGFP-Rab 9 ( $62\% \pm 18\%$ ) stained structures. Less particles are on the route from the plasma-membrane to early endosomes (co-localization with EGFP-Rab5a ( $14\% \pm 3\%$ )) or on the way backwards to the plasma-membrane in recycling endosomes (co-localization with EGFP-Rab4a ( $6\% \pm 1\%$ )) which can be seen in Figure 53A and B. Similar trends for intracellular co-locations with Rab family members were recently observed by Sandin *et al.*<sup>[202]</sup> Before endocytosis, the majority of surface bound carboxy SNARF-1 was deprotonated. During maturation from early to late

endosomes and lysosomes, the ratio of protonated to deprotonated SNARF-1-NPs increased with the decrease of the pH, which is caused by the vacuolar type of H<sup>+</sup>-ATPases (V-ATPases).<sup>[203]</sup>

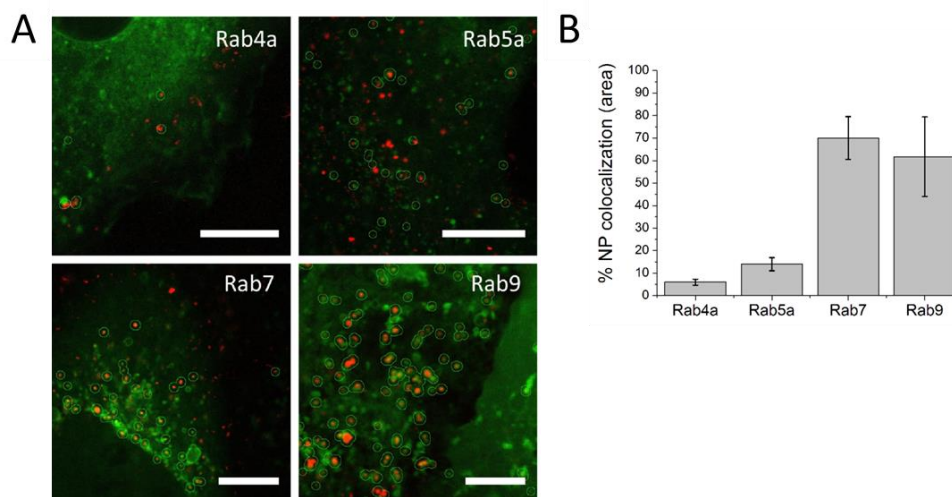


Figure 53 Co-localization of SNARF-1-NPs with endo/lysosomal marker proteins inside HeLa cells (1 h), (A) fluorescence live cell images of HeLa cells expressing fluorescent-labeled proteins of the Rab small GTPase family (green), co-localized structures highlighted by a yellow circle, bar scales 10 μm, (B) quantitative analysis of SNARF-1-NPs co-localizing with the indicated Rab proteins after 1 h uptake in HeLa cells. Object based co-localization is expressed as percentage area of NP overlapping with endosomal marker protein in relation to all SNARF-1-NPs. Mean value and standard deviation calculated from 5 images per time point.<sup>[187]</sup>

#### 6.4.5. Conclusion and Outlook for Section 6.4

Amine functionalized polystyrene nanoparticles with narrow size distribution were synthesized by soap-free emulsion polymerization and functionalized with the pH-responsive dual wavelength dye SNARF-1 by NHS ester mediated coupling reaction. The nanoparticles were characterized regarding their physico-chemical and optical properties proving that the dye molecules preserve their fluorescent properties as dual wavelength emitters even after coupling reaction. Such nanoparticle conjugated pH-sensors are potential tools for the monitoring of local pH changes in endo/lysosomal compartments what has also been shown. Their application will improve the understanding of basic cell-physiological processes, like

infection cycle of viruses or nanoparticle uptake and pH triggered drug release. Additionally, they may be applied for drug screening of pH affecting compounds like ionophores, or as diagnostic tool for pH affected diseases like cancer or Alzheimer.

The presented concept of SNARF-1 coupled to amino-functionalized NPs could be further developed towards a multifunctional sensor NP, *e.g.* by coupling additional ion sensors. The fluorescent spectrum of SNARF-1 can easily be distinguished from the  $\text{Ca}^{2+}$  chelator acetyloxymethyl 2-[5-[bis-[2-(acetyloxymethoxy)-2-oxoethyl]amino]-4-[2-[2-[bis-[2-(acetyloxymethoxy)-2-oxoethyl] amino]-5-methylphenoxy]ethoxy]-1-benzofuran-2-yl]-1, 3-oxazole-5-carboxylate (fura-2 AM) or the  $\text{Na}^+$  ion chelator bis(acetyloxymethyl) 4-[6-[13-[2-[2, 4-bis(acetyloxymethoxycarbonyl)phenyl]-5-methoxy-1-benzofuran-6-yl]-1, 4, 10-trioxa-7, 13-diazacyclopentadec-7-yl]-5-methoxy-1-benzofuran-2-yl]benzene-1,3-dicarboxylate (SBFI-AM), facilitating simultaneous measurement of  $\text{H}^+$ ,  $\text{Ca}^{2+}$  and  $\text{Na}^+$  ion concentrations in cells.<sup>[204]</sup> This study increases the understanding of cellular trafficking of nanoscale particles.

## 7. Experimental Section

### 7.1. General Procedures

#### 7.1.1. Materials

Styrene (Merck, Darmstadt, Germany) and acrylic acid (AA) were purified using a nitrogen pressured alumina flash column. All other chemicals were used without further purification: poly(sodium styrene sulfonate) (NaPSS, Sigma-Aldrich, St. Louis, USA), 2-aminoethyl methacrylate hydrochloride (AEMH, Sigma Aldrich, St. Louis, USA; 90%), 2,2'-azobis(2-(2-imidazolin-2-yl)propane) dihydrochloride (VA-044), ammonium peroxodisulfate (Sigma Aldrich, St. Louis, USA), sodium dodecyl sulfate (SDS, Sigma Aldrich, St. Louis, USA) and ethanol (VWR International GmbH, Darmstadt, Germany). Demineralized and MilliQ water (resistivity 18.2 M $\Omega$ ·cm) were used throughout the experiments.

#### 7.1.2. Carboxyl and Sulfonate Functionalized Nanoparticles by Soap-Free Emulsion Polymerization

Negatively charged carboxylated and sulfonated polystyrene colloids were prepared by soap-free emulsion copolymerization following a modified protocol from Goodwin.<sup>[21]</sup>

MilliQwater was heated up to 80 °C in a three-necked round-bottom flask equipped with a reflux condenser and septa. Under continuous bubbling of argon the water was deoxygenated for 30 min. Styrene was added with a syringe and the mixture was stirred for 10 min at  $\sim 1000 \text{ min}^{-1}$ . The comonomer (AA or NaPSS) was dissolved in 5 mL of MilliQ water and added to the reaction mixture with a syringe. After further 5 min the initiator (APS), dissolved in 5 mL of water was also added to the mixture to initiate the emulsion polymerization process. The polymerization proceeded under argon atmosphere and continuous stirring at  $\sim 700 \text{ min}^{-1}$  for 24 h. The particle dispersion was dialyzed (MWCO 14,000 g·mol<sup>-1</sup>, Carl Roth, Karlsruhe, Germany) for 3 d under repeated exchange of demineralized water. The experimental details as well as the physico-chemical characterization of the resulting colloids after dialysis were listed in Table 11.

Table 11 Amounts and characteristics of colloids (dialyzed) prepared by surfactant free emulsion polymerization with carboxyl and sulfonate groups on the particle surface.

sample (dialyzed)	St / g	MilliQ / mL	APS / mg	AA / mg	NaPSS / mg	R <sub>h</sub> / nm	σ / %	zeta- potential / mV
KB111122	30.0	300	99.6	-	11	419	10.0	-57.8 ± 6.5
KB111212	13.0	250	200.5	199.8	-	385	4.7	-49.2 ± 5.5
KB120510A	1.7	125	200.4	201.6	-	186	4.3	-48.0 ± 6.9
KB120510B	10	250	200.4	201.9	-	315	9.2	-53.6 ± 6.3
KB120529	17	250	200.7	200.6	-	432	6.9	-57.4 ± 5.7
G212	415	5000	1826	9587	-	1150	10.0	-67.6 ± 4.3

### 7.1.3. Amine Functionalized Nanoparticles by Soap-Free Emulsion Polymerization

Positively charged amine functionalized polystyrene colloids were synthesized by soap-free emulsion copolymerization following a modified protocol of Ganachaud *et al.*<sup>[189, 205]</sup>

MilliQ water was heated up to 55 °C for 30 min under continuous bubbling of argon. Styrene was added with a syringe and stirred for 10 min at 1200 ·min<sup>-1</sup>. After 5 min the comonomer (AEMH) dissolved in 2 mL MilliQ water was added with a syringe. After further 5 min the initiator (VA-044), dissolved in 3 mL MilliQ water was also added to initiate the polymerization process. The polymerization proceeded for 24 h at 55 °C under continuous stirring at 500 min<sup>-1</sup> under argon atmosphere. After synthesis and cooling down, the dispersion was dialyzed (Table 12 shows the experimental setup and the particle size determination for the amine functionalized colloids prepared by surfactant free emulsion polymerization).

Table 12 Amounts and characteristics of colloids with amine groups on the surface prepared by surfactant free emulsion copolymerization after thorough dialysis.

sample (dialyzed)	St / mL	MilliQ / mL	VA-044 / mg	AEMH / mg	R <sub>h</sub> / nm	σ / %	zeta- potential / mV
KB120912A	11	125	284.4	500.0	150	14.7	46.3 ± 6.1
KB120912B	5.5	125	284.4	250.0	67	14.9	43.5 ± 10.7
KB120917A	15	200	284.4	341.3	89	13.5	38.8 ± 11.4
KB130114A	15	200	284.4	409.5	92	15.2	43.9 ± 13.3
KB130114B	15	200	284.4	682.5	135	15.6	45.0 ± 5.0

#### 7.1.4. Cleaning of Colloid Dispersions

3 mL of the colloid dispersion was washed before further usage with an ethanol-water mixture (50 vol.%) and by centrifugation-redispersion cycles. Particles < 1 μm were centrifuged 35 min at 10,000·min<sup>-1</sup> and particles > 1 μm 20 min at 8,000·min<sup>-1</sup>. Therefore, after centrifugation the supernatant was replaced with the same volume of an ethanol-water mixture and redispersed by ultrasonication. After 3 cycles of centrifugation the supernatant was replaced with MilliQ water and the solid content was adjusted to 5.0 wt.% if not stated otherwise.

#### 7.1.5. Cleaning of Glass or Wafer Substrates

The substrates were cleaned using a basic piranha-solution to remove any impurities and to decrease the contact angle to almost 0°. Therefore, the substrates were placed into a Färber box containing a solution of 10 mL 33% hydrogen peroxide solution, 10 mL 30% ammonia solution (NH<sub>4</sub>OH) and 50 mL MilliQ water (*careful! Basic piranha solution is extremely corrosive!*). The substrates were heated up to 75 °C for 45 min. After cooling down the substrates were thoroughly rinsed with MilliQ water and stored in ethanol until use.

### **7.1.6. Colloidal Monolayer Formation at the Langmuir-Blodgett Trough**

The aqueous colloidal dispersion was diluted 1:2 with ethanol as spreading agent. For the self-assembly the dispersion was spread onto the water surface of the Langmuir trough (KSV NIMA, Biolin Scientific with a length of 364 cm and a width of 75 cm (total surface area 273 cm<sup>2</sup>), using a partially immersed tilted glass slide as spreading help. The dispersion was added drop wise at the upper end of the glass slide to flow down slowly. This led to well-ordered hexagonally densely packed monolayers. All other particle arrangements were prepared by direct applying the dispersion-ethanol mixture drop wise at the air-water interface of the Langmuir trough using a 100  $\mu$ L Eppendorf pipette. The surface film was allowed for 10 min to equilibrate before compression to assure that the entire spreading agent was evaporated. The process can be followed by surface pressure detection using the Wilhelmy plate film balance of the Langmuir trough. When the ethanol was completely evaporated the surface pressure stays constant indicating the point where the colloidal monolayer at the interface can be compressed by the moveable barriers of the trough. The created monolayer can be transferred to the substrate lying in the subphase on a special holder by surface lowering transfer (Figure 9). Therefore, the subphase was removed after compression behind the barriers using a membrane pump ( $1 \text{ L}\cdot\text{h}^{-1}$ ), whereupon the monolayer is settled smoothly onto the substrate. The monolayer covered substrate was dried under a shallow angle until all water has been evaporated.

### **7.1.7. General Analytical Tools**

#### **7.1.7.1. Dynamic Light Scattering and Photon Cross-Correlation Spectroscopy**

The average hydrodynamic radius and the size distribution of the colloids was measured either by angle-dependent dynamic light scattering (ALV/CGS3 compact goniometer system with a He/Ne laser (632.8 nm)) at 20 °C or with photon cross-correlation spectroscopy (Nanophox, Sympatec GmbH, Clausthal-Zellerfeld, Germany). The final solid content of the colloid dispersion in MilliQ water was adjusted to 0.01 wt.% for the measurements.

### 7.1.7.2. Zeta-Potential Measurements

The zeta-potential measurements were performed using a Nano Zetaziser (3000 HAS Malvern Instruments GmbH, Herrenberg, Germany). Colloid dispersions were diluted with KCl solution ( $1 \cdot 10^{-3} \text{ mol} \cdot \text{L}^{-1}$ ) to a final solid content of approximately 0.01 wt.%. The dispersion was applied to a special capillary cell and measured in triplicate. The average value of the three measurements was used as final value for the zeta-potential.

### 7.1.7.3. Particle Charge Detection

The amount of functional groups on the particle surface was determined by titration against the opposite charged polyelectrolyte. Poly(diallyldimethyl ammonium chloride) (PDADMAC) was used as polyelectrolyte for the determination of carboxyl and sulfonate groups on the particles surface and polyelectrolyte sodium polyethylene sulfonate (PESNa) for the amine functionalized particles. The instrumental setup consisted of the particle charge detector (Mütek GmbH, Germany) in combination with a Titrino Automatic Titrator (Metrohm AG, Switzerland). For the measurements 10 mL of the colloid dispersion (0.1 wt.%) were titrated at least three times against the opposite charged polyelectrolyte. The average number of functional groups was calculated from the amount of consumed polyelectrolyte.<sup>[206]</sup>

### 7.1.7.4. Fluorescamine Assay

The amount of amine groups on the particle surface was also detected and calculated by fluorescence titration following the procedure published by Ganachaud *et al.*<sup>[188, 205]</sup> In brief, the calibration curve was plotted from hexylamine solutions of given concentrations in sodium borate buffer (pH = 9.5,  $0.1 \text{ mol} \cdot \text{L}^{-1}$ ) and freshly prepared fluorescamine solution in acetone ( $0.3 \text{ g} \cdot \text{L}^{-1}$ ). 25  $\mu\text{L}$  of the colloid dispersion with a solid content of 1.0 wt.% were added to 725  $\mu\text{L}$  of borate buffer together with 250  $\mu\text{L}$  of fluorescamine solution. After 30 s vigorous mixing, 100  $\mu\text{L}$  of the dispersion were placed in a 96-well plate (Corning Incorporated 3603) and fluorescence emission of the fluorescamine at  $\lambda_{em} = 470 \text{ nm}$  was

followed by a Tecan Infinite M1000 Plate Reader (Tecan Group Ltd., Maennedorf, Switzerland) using an excitation wavelength of  $\lambda_{ex} = 410$  nm.

#### **7.1.7.5. Differential Scanning Calorimetry and Thermal Gravimetric Analysis**

The colloid dispersion was dried before measurement by freeze-drying and 10-25 mg was placed in the crucible. Differential scanning calorimetry was measured using a DSC823<sup>e</sup> (Mettler Toledo, Gießen, Germany) following a heat protocol of 10 K·min<sup>-1</sup> under nitrogen atmosphere from 25 up to 300 °C.

#### **7.1.7.6. SEM Measurements**

All scanning electron micrographs were recorded using a Gemini 1530 microscope (Carl Zeiss AG, Oberkochen, Germany) at 0.3 kV. The samples from colloid dispersion after polymerization were prepared using a 0.01 wt.% colloid dispersion which is placed in the middle of a 5x5 mm<sup>2</sup> single side polished silicon wafer (Si-Mat, Kaufering, Germany). After evaporation of the water drop a thin layer of colloids is left on the wafer surface which was placed into the electron microscope.

### **7.2. Experimental Details for Section 6.1 and 6.2**

#### **7.2.1. Entrapment of Nanoparticles at the Air-Water Interface with Poly(butyl cyanoacrylate)**

To visualize nanoparticles directly at the air-water interface the interfacial polymerization with butyl cyanoacrylate (BCA) was used. For entrapping hexagonal arrangements a 100 mL dish was first filled with MilliQ water or 0.1 mM SDS solution and a pre-cleaned hydrophilic glass slide partially immersed into the subphase in a shallow angle of 45°. The diluted colloidal dispersion (2.5 wt.%, 50 vol.% ethanol) was applied to the air-water interface by the

glass slide until the surface was completely covered. Afterwards, the glass slide was removed carefully and BCA was heated up to 50 °C in an aluminum dish next to the monolayer containing dish. Both dishes were placed in a closed box, whereupon the polymerization of BCA was initiated by contact with the water surface. Depending on the duration and the amount of BCA addition by the gas phase, the thickness of the PBCA-composite film was adjusted. The composite films were carefully transferred onto a pre-cleaned substrate by vertically immersion into the water subphase and following slow lifting above the interface under a shallow angle into a horizontal position. After drying, the samples were examined by scanning electron microscopy.

For the interfacial polymerization at the Langmuir trough a different experimental setup was necessary as can be seen in Figure 12. The colloidal monolayer was prepared as described earlier and compressed to the desired surface pressure. Then, the BCA placed in a pre-heated (80 °C) aluminum dish covered with a funnel-tube-funnel system was evaporated. The temperature needs to be higher than for the entrapment in a BCA gas filled box as described earlier to guarantee the passage of the BCA gas from the pre-heated dish across the funnel-tube construction to the water interface of the trough. The composite film is transferred to the substrate by surface lowering transfer. Therefore, the subphase was removed behind the barriers using a membrane pump (1 L·h<sup>-1</sup>). The composite film covered the substrate and after drying it was examined by electron microscopy.

### **7.2.2. Preparation of Colloid-Copolymer Mixtures**

For the preparation of non-hexagonally closed packed colloidal monolayers a mixture of colloids with the block-copolymer PAA<sub>x</sub>-*b*-PMMA<sub>y</sub> <sup>[155, 156]</sup> with varying concentrations, block lengths (x, y) and molecular weight were used. Prior use, the block-copolymer was dissolved in water with 1eq. of 1M NaOH ( $c = 10 \text{ mg}\cdot\text{mL}^{-1}$ ) at 70 °C and neutralized with 1M HCl using a pH-meter. The block-copolymer solution was added to the pre-cleaned particle dispersion and mixed for 30 s. For application on the Langmuir trough the mixture was diluted with ethanol (50 vol.%) and spread at the air-water interface.

## **7.2.3. Analytical Tools for Section 6.1 and 6.2**

### **7.2.3.1. Colloidal Probe AFM**

For comparison, particle contact angles were measured using an atomic force microscope (AFM). Polystyrene particles were glued to tipless AFM cantilevers (Mikromasch NSC12) using a two-component, room temperature curing epoxy (Uhu Endfest 300). Using an AFM (JPK Nanowizard), the particles were brought into contact with the air-liquid interface of an air bubble ( $\sim 0.5 \mu\text{L}$  in volume) in a polystyrene petri dish filled with distilled, deionized water, and then pulled away. Both the position of the cantilever and its deflection were recorded during the measurement. The force on the cantilever over the course of the measurement was determined from the deflection using the cantilever spring constant, which was measured using the thermal noise method with a Dimension 3100 AFM. The position of the particle was determined by subtracting the deflection of the cantilever from its position. The particle contact angles were determined from plots of the force on the particle against the particle position. The receding particle contact angle were determined based on the distance  $d$  between the point where the particle makes contact with the interface and the point where the particle is at its equilibrium position with respect to the interface as the particle comes into contact with the bubble. Advancing contact angles were determined similarly, using the equilibrium position as the particle was withdrawn from the bubble.

## **7.2.4. Optical Determination of the contact angle**

From scanning electron micrographs, the top view diameters of the visible parts of the colloids were evaluated using the program ImageJ. At least 100 objects were used for the analysis.

## 7.3. Experimental Details for Section 6.3

### 7.3.1. Materials

Styrene (Merck, Darmstadt, Germany), acrylic acid (AA, Sigma-Aldrich, St. Louis, USA) and butyl acrylate (BA, Sigma-Aldrich, St. Louis, USA) were purified using a nitrogen pressured alumina flash column. All other chemicals were used without further purification: 2,2'-azobis(2-methylbutyronitrile) (V59, Wako Chemicals, Neuss, Germany), *cis*-1,2-dicyano-1,2-bis-(2,4,5-trimethyl-3-thienyl) ethene (CMTE, TCI Europe), *N*-(2,6-diisopropylphenyl)-perylene-3,4-dicarboximid (PMI, a donation from BASF, Ludwigshafen, Germany), ethanol (VWR International GmbH, Darmstadt, Germany), purchased from Sigma Aldrich (St. Louis, USA): ammonium peroxydisulfate (APS), hexadecane, and sodium dodecyl sulfate (SDS). Demineralized and MilliQ water (resistivity 18.2 M $\Omega$ -cm) were used throughout the experiments.

### 7.3.2. Photoswitchable Nanoparticles by Miniemulsion Polymerization

The photoswitchable dye-labeled particles were synthesized following the standard recipe for a direct miniemulsion polymerization.

6 g of the monomer (styrene (St) or butyl acrylate (BA)) were mixed with 250 mg of hexadecane (HD), 100 mg of the initiator (V59) and varying amounts of the photoswitchable dye CMTE and the fluorescent dye PMI. After complete dissolution of the dyes the monomer mixture was added to a solution of 100 mg sodium dodecyl sulfate (SDS) dissolved in 24 g of MilliQ water and stirred at 900 rpm for 1 h. The typical miniemulsion was created by ultrasonication (Branson digital sonifier 450-D, Dietzenbach, Germany) of the pre-emulsion under ice-cooling with a ½" tip, 90% amplitude following a 10 s-pulse-10 s-pause protocol for 2 min. Afterwards, the mixture was transferred into a round bottom flask and heated up to 72 °C under gentle stirring for 24 h. After polymerization the particle dispersion was dialyzed (Table 13 shows the experimental setup and the particle size characterization for the colloids prepared by miniemulsion polymerization).

Table 13 Amounts and characteristics of colloids (dialyzed) prepared by miniemulsion polymerization.

sample (dialyzed)	St / g	BA / g	HD / mg	PMI / mg	CMTE / mg	V59 / mg	SDS / mg	MilliQ / g	R <sub>h</sub> /nm	σ /%
KB111213A	6.0	-	257.1	2.6	25.4	100.0	100,1	24.0	90	15.6
KB111213B	-	6.0	253.7	2.3	25.4	100.1	100,4	24.0	156	12.8
KB111213C	6.0	-	253.5	2.0	50.6	99.7	100,3	24.0	96	16.7
KB111213D	-	6.0	251.8	2.3	50.0	99.8	100,3	24.0	165	18.2
KB120521A	6.0		250.4	4.1	50.7	100.6	100.3	24.0	131	21
KB120521B	-	6.0	251.3	4.3	50.3	100.1	100.4	24.0	120	25

### 7.3.3. Photoswitchable Nanoparticles by Seeded Emulsion Polymerization

A dispersion of 100 mL MilliQ water containing 0.1 wt.% of seed particles (dialyzed, photoswitchable polystyrene or poly(butyl acrylate) colloids from miniemulsion polymerization) and 0.01 wt.% of SDS was heated up to 75 °C under continuous stirring in a three necked round bottom flask equipped with a condenser and septa. Argon gas was bubbled through the dispersion for 30 min. 500 mg of the initiator ammonium peroxodisulfate (APS) were dissolved in 3 mL water and added by a syringe to the stirred dispersion. Furthermore, 2 g of styrene and 150 mg of acrylic acid were mixed and added with a syringe pump at a flow rate of 1 mL·h<sup>-1</sup> to the stirring dispersion. The reaction was polymerized at 80 °C for 24 h under argon atmosphere. The dispersion was dialyzed (membranes with MWCO 14,000 g·mol<sup>-1</sup>, Carl Roth, Karlsruhe, Germany) for 3 d under repetitive exchange of the demineralized water.

Table 14 Amounts and characteristics of colloids (dialyzed) prepared by seeded emulsion polymerization.

sample (dialyzed)	Seed dispersion	styrene / mL	APS / mg	SDS / mg	MilliQ / mL	AA / mg	R <sub>h</sub> / nm	σ / %
<b>KB120201B</b>	KB111213Adial 0.33 g	2.8	250.7	5.6	50	-	321	15.0
<b>KB120201C</b>	KB111213Bdial 0.28 g	0.8	250.0	5.2	50	-	286	12.9
<b>KB120201D</b>	KB111213Cdial 0.30 g	2.2	250.3	5.3	50	-	316	17.4
<b>KB120201E</b>	KB111213Ddial 0.30 g	0.9	250.7	5.0	50	-	316	11.6
<b>KB120309A</b>	KB111213Adial 0.33 g	4.0	249.9	5.0	50	250	333	13.8
<b>KB120309B</b>	KB111213Bdial 0.28 g	0.6	250.9	4.9	50	250	158	16.0
<b>KB120621A</b>	KB120521Adial 0.58 g	2.2	501.5	10.1	100	151.3	191	8.9
<b>KB120612B</b>	KB120521Bdial 0.69 g	2.2	501.5	10.1	100	150.0	260	11.9

### 7.3.4. Creation of Binary Photoswitchable Colloidal Monolayers

For the preparation of photoswitchable binary colloidal monolayers the co-assembly method of colloids at the air-water interface of a Langmuir trough was used. Prior use, the colloid dispersions were prepared as described under chapter 7.1.4. Here, two dispersions containing colloids of different sizes and functionalities were mixed in a distinct number ratio of large to small ( $N_{large}/N_{small}$  such as 1/6) particles and diluted with 50 vol.% ethanol as spreading agent. The larger non-fluorescent particles (1150 nm, 14.3 wt.%) were used as a template for the smaller photoswitchable particles (190 nm, 1.1 wt.%) prepared by seeded emulsion polymerization. After compressing ( $v_{comp} = 20 \text{ mm}\cdot\text{min}^{-1}$ ) the air-water interface the binary colloidal monolayer was transferred to a silicon wafer and investigated with a scanning electron Gemini 1530 microscope (Carl Zeiss AG, Oberkochen, Germany).

### **7.3.5. Irradiation of the Photoswitchable Dye CMTE in Solutions and Colloids**

For the irradiation experiments and investigation of the photo-states of the photo-responsive dye CMTE a mercury short arc lamp (HBO 100 W/2, 100 W, Osram) was used. The wavelength was adjusted with different optical band filters. For UV-irradiation a dark violet band pass (UG 1, Schott, 270-430 nm) and for VIS-light irradiation a combination of a light blue broad band (BG39, Schott) and a yellow optical filter (OG515, Schott) were used, transmitting light within a wavelength range of 515 to 690 nm. Either dye solutions or colloid dispersions were placed in front of the mercury short arc lamp under continuous stirring and irradiated with the wavelength range that is needed for distinct photo-states of the photochromic dye (CMTE).

### **7.3.6. Analytical Tools for Section 6.3**

#### **7.3.6.1. UV-VIS Spectroscopy**

Absorption spectra of the photochromic dye (CMTE) in solution were measured using a Perkin Elmer Lambda 25 UV-VIS spectrometer. 3 mL of a solution of the photochromic dye in the corresponding monomer (styrene or BA) with a concentration of  $c = 1 \cdot 10^{-6} \text{ mol} \cdot \text{L}^{-1}$  were analysed within a wavelength range between 300 – 800 nm.

#### **7.3.6.2. Fluorescence Emission Spectroscopy**

Fluorescence emission spectra were recorded on a TIDAS 3D fluorescence spectrometer with an excitation wavelength of  $\lambda_{ex} = 490 \text{ nm}$ . For the measurements 3 mL of a fluorescent dye solution (PMI,  $c = 5.2 \cdot 10^{-6} \text{ mol} \cdot \text{L}^{-1}$ ) in monomer (styrene and butyl acrylate) were used. Dispersions of photoswitchable nanoparticles (solid content of 1.5 wt.%) from miniemulsion as well as from seeded emulsion polymerization were also investigated.

### 7.3.6.3. Confocal Laser Scanning Microscopy

Photoswitchable binary colloidal monolayers from large plain template particles (1150 nm) and photoswitchable smaller particles (190 nm) were investigated after co-assembly and compression at the air-water interface of a Langmuir trough. After transfer to a microscopy glass substrate the monolayer was imaged using a TCS SP5 (Leica) with a tunable argon laser at  $\lambda_{ex} = 488$  nm.

### 7.3.6.4. Fluorescence Microscopy

For the photoswitching of the functional colloidal monolayers an optical wide field fluorescence microscope (Olympus IX81, inverted fluorescence microscope, Hamburg, Germany) with 2.5x objective (UIS2), 100 W halogen lamp and different filters, such as a DAPI filter (UMNU 2,  $\lambda_{ex} = 360$  nm and  $\lambda_{em} = 420$  nm) for the UV-light irradiation and a eGFP filter (U-MF2,  $\lambda_{ex} = 472$  nm and  $\lambda_{em} = 520$  nm) for the VIS-light irradiation were used. The sample was alternately irradiated for 5 min with either UV or VIS-light and images were taken using the eGFP filter for the excitation of PMI.

## 7.4. Experimental Details for Section 6.4

### 7.4.1. Materials

For the preparation of pH nano-sensors the following chemicals were used: the pH-sensitive dye 5' (and 6') carboxy-10-dimethylamino-3-hydroxy-spiro[7H-benzo[c]xanthene-7,1'(3'H)-isobenzofuran]-3'-one (carboxy SNARF-1), SNARF-1 acetate succinimidyl ester (SNARF-1-NHS), SNARF-1 acetoxymethyl ester acetate (SNARF AM ester); all Invitrogen, Karlsruhe, Germany, dimethyl sulfoxide (DMSO, Merck, Darmstadt, Germany), fluorescamine (Sigma Aldrich, St. Louis, USA; >98%), sodium borate (Merck, Darmstadt, Germany), hexylamine (Sigma Aldrich, St. Louis, USA; 99%), Hank's Balanced Salt Solution (HBSS, Life Technologies GmbH, Darmstadt, Germany), Dulbecco's Modified Eagle Medium (DMEM Gibco®, Life Technologies GmbH, Darmstadt, Germany), 4-(2-hydroxyethyl)-1-piperazineethanesulfonic acid (HEPES), 2-(*N*-morpholino)ethane sulfonic acid (MES) and fetal calf serum (FCS, Gibco®,

Life Technologies GmbH, Darmstadt, Germany). Demineralized and MilliQ water (resistivity 18.2 M $\Omega$ -cm) were used throughout the experiments.

#### **7.4.2. Preparation of SNARF-Labeled Nanoparticles**

Amino functionalized colloidal particles (KB130114B, dialyzed) were used for the preparation of SNARF-labeled nano-particular pH sensors (Table 9).

The pH-sensitive dye SNARF-1-NHS was coupled onto amino-functionalized polystyrene colloids forming an amide bond between the amine group of the nanoparticle and the carboxylic acid function of the dye. 0.11 mg of SNARF-1-NHS dissolved in 440  $\mu$ L dimethyl sulfoxide (DMSO) ( $c = 0.25 \text{ mg}\cdot\text{mL}^{-1}$ ) were added to a dispersion of amino-functionalized colloids with a solid content of 0.4 wt.% and stirred for 24 h. An excess of 3000 $\times$  of SNARF-1-NHS with regard to the total amount of determined surface amine groups was used. After coupling and prior use for further experiments, the colloids were purified by dialysis (MWCO 14,000  $\text{g}\cdot\text{mol}^{-1}$ , Carl Roth, Karlsruhe, Germany) under repetitive exchange of demineralized water for 3 d and then washed with MilliQ water via repetitive centrifugation/redispersion in the same amount of water at 22,000  $\text{min}^{-1}$  for 45 min until no fluorescence intensity was detected in the supernatant.

#### **7.4.3. Probing of Nanoparticle pH Environment in HeLa Cells**

HeLa cells were incubated in DMEM with 10% fetal calf serum (FCS), 100  $\text{units}\cdot\text{mL}^{-1}$  penicillin and 100  $\mu\text{g}\cdot\text{mL}^{-1}$  streptomycin in a humidified incubator at 37  $^{\circ}\text{C}$  and 5% carbondioxide ( $\text{CO}_2$ ). For confocal laser scanning microscopy (CLSM), cells were seeded at a concentration of  $1.5 \cdot 10^4 \text{ cells}\cdot\text{cm}^{-2}$  and grown on 8-well cover glass Lab-Teks (Nunc, Langensfeld, Germany).

#### **7.4.4. Intracellular calibration with SNARF-1-AM Ester and SNARF-1-NP**

The pH-responsive SNARF dye was calibrated in cells with SNARF-1-AM ester and SNARF-1-NPs. Before imaging cells were allowed to grow for 24 h on 8-well cover glass Lab-Teks.

SNARF-1 AM ester (0.5  $\mu\text{g}$ ), dissolved in 1  $\mu\text{l}$  DMSO (0.5  $\text{g}\cdot\text{L}^{-1}$ ), was incubated with 10  $\mu\text{l}$  of FCS for 5 min to improve the water solubility and loading efficiency. Before loading the HeLa cells with SNARF-1 AM ester, the cells were washed with Hank's Balanced Salt Solution buffer (HBSS, Life Technologies GmbH, Darmstadt, Germany), then the mixture was added to the cells together with 500  $\mu\text{l}$  HBSS buffer. The cleavage of the dye by esterases was performed in a humidified incubator at 37  $^{\circ}\text{C}$  and 5%  $\text{CO}_2$  for 30 min. After dye loading, the HBSS buffer was replaced by a buffer with the desired pH value (Table 10). Alternatively, for calibration measurements with dye-NP conjugates, cells were loaded with 0.075  $\text{g}\cdot\text{L}^{-1}$  of SNARF-1-NP for 24 h, then washed and measured in 500  $\mu\text{l}$  buffer with the different pH value (Table 10). All buffers used were potassium rich and carbonate-free to ensure good pH equilibration by  $\text{K}^+$  ionophores and long-time pH stability in the presence of air, respectively. The pH equilibration was performed by adding the ionophores nigericin (5  $\mu\text{g}$ ) and valinomycin (2.5  $\mu\text{g}$ ), dissolved in 7.5  $\mu\text{L}$  DMSO to the 500  $\mu\text{L}$  HBSS buffer. The ionophores were added to the cells immediately before the measurements and measured within 5 min. Buffers were used for intracellular calibration. Buffer chemicals were solved in 500 mL demineralized water. After pH adjustment with 0.1 M hydrochloric acid (HCl) or sodium hydroxide (NaOH), they were sterile filtered and stored at 4  $^{\circ}\text{C}$ .

#### **7.4.5. Analytical Tools for Section 6.4**

##### **7.4.5.1. Fluorescence Emission Spectroscopy**

Fluorescence emission spectra of the free carboxy SNARF-1-dye and SNARF-1-NPs ( $c = 100 \mu\text{g}\cdot\text{mL}^{-1}$ ) were recorded using an excitation wavelength of  $\lambda_{\text{ex}} = 514 \text{ nm}$  at different pH values to evaluate dye functionality after NP coupling with the M1000 plate reader (Tecan Group Ltd., Maennedorf, Switzerland), gain 200 and bandwidth 5 nm. A solution of the dye carboxy SNARF-1 ( $c = 0.5 \mu\text{g}\cdot\text{mL}^{-1}$ ) was diluted with buffer solutions of varying pH to

obtain a final concentration of ( $c = 1 \mu\text{g}\cdot\text{mL}^{-1}$ ). The colloids with coupled SNARF dye were also diluted to result a final concentration of SNARF-1-NPs ( $c = 100 \mu\text{g}\cdot\text{mL}^{-1}$ ). Further, 200  $\mu\text{L}$  of the corresponding solution or dispersion were placed in black clear-bottom polystyrene 96-well plates (Corning Inc., New York, USA). The fluorescence emission spectra were measured twice and the average values of the wavelength dependent fluorescence emission of both measurements were used to obtain the final emission spectra.

### 7.4.5.2. Confocal Laser Scanning Microscopy

CLSM measurements were performed using a TCS SP5 (Leica), a 100 $\times$  oil plan apochromat objective (1.4 numerical aperture), and a tunable argon laser with  $\lambda_{ex} = 514 \text{ nm}$ . Emission range was set to  $\lambda_{em} = 550 - 610 \text{ nm}$  and  $\lambda_{em} = 640 - 750 \text{ nm}$ . Signals were detected by photomultipliers with fixed gain values. For calibration, 5-10 images were collected per pH value and the mean intensity of the cytosol (SNARF-AM ester) or vesicular structures (SNARF-1-NPs) was quantified. Care was taken that the ratios of the fluorescence intensities of the protonated and deprotonated form of SNARF-1 (Figure 45) were acquired with the same instrumental setup and settings in all experiments.

### 7.4.5.3. TEM Measurements

Transmission electron microscopy on HeLa cells treated one and three hours of incubation time with  $300 \mu\text{g}\cdot\text{mL}^{-1}$  of SNARF-1-NPs was used to visualize SNARF-1-NPs at high resolution in their cellular environment. Before treatment, cells were cultured for 48 h after seeding onto 3 mm  $\varnothing$  sapphire discs at a density of  $30.000 \text{ cells}\cdot\text{cm}^{-2}$  in a 24-well plate. At the end of the incubation period, cells were fixed by means of high pressure freezing using a Compact 01 HPF machine (Wohlwend GmbH, Switzerland). Subsequent freeze-substitution was conducted using a Leica EM AFS 2 device (Leica Microsystems, Germany). The substitution medium contained acetone p.a., 0.2% osmium tetroxide, 0.1% uranyl acetate and 5% water. The mixture was pre-cooled to  $-90^\circ\text{C}$  before the samples were added. After freeze-substitution, the samples were washed twice with acetone p.a. and finally embedded into

EPON 812 resin. Ultrathin sectioning of the embedded samples was performed using a Leica Ultracut UCT (Leica Microsystems, Germany) equipped with a diamond knife.

Examination of thin sections was conducted using a FEI Tecnai F20 transmission electron microscope (FEI, USA) operated at an acceleration voltage of 200 kV. Bright field images were acquired using a Gatan US1000 slow scan CCD camera (Gatan Inc., USA).

## 8. Bibliography

1. Pieranski, P., *TWO-DIMENSIONAL INTERFACIAL COLLOIDAL CRYSTALS*. Physical Review Letters, **1980**. 45(7): p. 569-572.
2. Retsch, M., et al., *Template-free structuring of colloidal hetero-monolayers by inkjet printing and particle floating*. Soft Matter, **2010**. 6(11): p. 2403-2412.
3. Vogel, N., et al., *Laterally Patterned Ultraflat Surfaces*. Small, **2009**. 5(7): p. 821-825.
4. Galisteo-Lopez, J.F., et al., *Self-Assembled Photonic Structures*. Advanced Materials, **2011**. 23(1): p. 30-69.
5. Hulteen, J.C., et al., *Nanosphere lithography: Size-tunable silver nanoparticle and surface cluster arrays*. Journal of Physical Chemistry B, **1999**. 103(19): p. 3854-3863.
6. Hulteen, J.C. and R.P. Van Duyne, *Nanosphere lithography: A materials general fabrication process for periodic particle array surfaces*. Journal of Vacuum Science & Technology A, **1995**. 13(3): p. 1553-1558.
7. Haes, A.J., et al., *Nanoscale optical biosensor: Short range distance dependence of the localized surface plasmon resonance of noble metal nanoparticles*. Journal of Physical Chemistry B, **2004**. 108(22): p. 6961-6968.
8. Haes, A.J., et al., *A nanoscale optical biosensor: The long range distance dependence of the localized surface plasmon resonance of noble metal nanoparticles*. Journal of Physical Chemistry B, **2004**. 108(1): p. 109-116.
9. Fischer, J., et al., *Near-Field-Mediated Enhancement of Two-Photon-Induced Fluorescence on Plasmonic Nanostructures*. Journal of Physical Chemistry C, **2010**. 114(49): p. 20968-20973.
10. Camden, J.P., et al., *Controlled Plasmonic Nanostructures for Surface-Enhanced Spectroscopy and Sensing*. Accounts of Chemical Research, **2008**. 41(12): p. 1653-1661.
11. Bianchi, E., R. Blaak, and C.N. Likos, *Patchy colloids: state of the art and perspectives*. Physical Chemistry Chemical Physics, **2011**. 13(14): p. 6397-6410.
12. Groschel, A.H., et al., *Guided hierarchical co-assembly of soft patchy nanoparticles*. Nature, **2013**. 503(7475): p. 247-251.
13. Jensen, T.R., G.C. Schatz, and R.P. Van Duyne, *Nanosphere lithography: Surface plasmon resonance spectrum of a periodic array of silver nanoparticles by ultraviolet-visible extinction spectroscopy and electrodynamic modeling*. Journal of Physical Chemistry B, **1999**. 103(13): p. 2394-2401.
14. Derjaguin, B., *A theory of interaction of particles in presence of electric double layers and the stability of lyophobic colloids and disperse systems*. Acta Physicochimica Urss, **1939**. 10(3): p. 333-346.

15. Derjaguin, B. and L. Landau, *THEORY OF THE STABILITY OF STRONGLY CHARGED LYOPHOBIC SOLS AND OF THE ADHESION OF STRONGLY CHARGED-PARTICLES IN SOLUTIONS OF ELECTROLYTES*. Progress in Surface Science, **1993**. 43(1-4): p. 30-59.
16. Verwey, E.J.W., *THEORY OF THE STABILITY OF LYOPHOBIC COLLOIDS*. Journal of Physical and Colloid Chemistry, **1947**. 51(3): p. 631-636.
17. Stern, O., *The theory of the electrolytic double shift*. Zeitschrift Fur Elektrochemie Und Angewandte Physikalische Chemie, **1924**. 30: p. 508-516.
18. Grahame, D.C., *THE ELECTRICAL DOUBLE LAYER AND THE THEORY OF ELECTROCAPILLARITY*. Chemical Reviews, **1947**. 41(3): p. 441-501.
19. Butt, H.J.G., K.; Kappl, M., *Physics and Chemistry of Interfaces*. 2006, Weinheim: Wiley-VCH.
20. Russel, W.B., D. A. Saville, and W.R. Schowalter., *Colloidal Dispersions*. 1989: Cambridge University Press.
21. Goodwin, J.W., et al., *STUDIES ON PREPARATION AND CHARACTERIZATION OF MONODISPERSE POLYSTYRENE LATTICES .3. PREPARATION WITHOUT ADDED SURFACE-ACTIVE AGENTS*. Colloid and Polymer Science, **1974**. 252(6): p. 464-471.
22. Oettel, M. and S. Dietrich, *Colloidal Interactions at Fluid Interfaces†*. Langmuir, **2008**. 24(4): p. 1425-1441.
23. Oettel, M., A. Domínguez, and S. Dietrich, *Attractions between charged colloids at water interfaces*. Journal of Physics: Condensed Matter, **2005**. 17(32): p. L337.
24. Maestro, A., et al., *Contact angle of micro- and nanoparticles at fluid interfaces*. Current Opinion in Colloid & Interface Science, **2014**. 19(4): p. 355-367.
25. Paunov, V.N., et al., *LATERAL CAPILLARY FORCES BETWEEN FLOATING SUBMILLIMETER PARTICLES*. Journal of Colloid and Interface Science, **1993**. 157(1): p. 100-112.
26. Danov, K.D. and P.A. Kralchevsky, *Capillary forces between particles at a liquid interface: General theoretical approach and interactions between capillary multipoles*. Advances in Colloid and Interface Science, **2010**. 154(1–2): p. 91-103.
27. Stamou, D., C. Duschl, and D. Johannsmann, *Long-range attraction between colloidal spheres at the air-water interface: The consequence of an irregular meniscus*. Physical Review E, **2000**. 62(4): p. 5263-5272.
28. Kralchevsky, P.A. and K. Nagayama, *Capillary interactions between particles bound to interfaces, liquid films and biomembranes*. Advances in Colloid and Interface Science, **2000**. 85(2–3): p. 145-192.
29. Poon, W.C.K., *The physics of a model colloid–polymer mixture*. Journal of Physics: Condensed Matter, **2002**. 14(33): p. R859.

30. Oversteegen, S.M. and H.N.W. Lekkerkerker, *On the accuracy of the Derjaguin approximation for depletion potentials*. *Physica A: Statistical Mechanics and its Applications*, **2004**. 341(0): p. 23-39.
31. Tuinier, R., J. Rieger, and C.G. de Kruif, *Depletion-induced phase separation in colloid-polymer mixtures*. *Advances in Colloid and Interface Science*, **2003**. 103(1): p. 1-31.
32. Jenkins, P. and M. Snowden, *Depletion flocculation in colloidal dispersions*. *Advances in Colloid and Interface Science*, **1996**. 68: p. 57-96.
33. Napper, D.H., *Steric stabilization*. *Journal of Colloid and Interface Science*, **1977**. 58(2): p. 390-407.
34. Goldenberg, L.M., et al., *Ordered Arrays of large latex particles organized by vertical deposition*. *Langmuir*, **2002**. 18(8): p. 3319-3323.
35. Malaquin, L., et al., *Controlled particle placement through convective and capillary assembly*. *Langmuir*, **2007**. 23(23): p. 11513-11521.
36. Chen, K.M., et al., *Selective self-organization of colloids on patterned polyelectrolyte templates*. *Langmuir*, **2000**. 16(20): p. 7825-7834.
37. Arutinov, G., S.B. Brichkin, and V.F. Razumov, *Self-Assembling of polystyrene microsphere monolayers by spin-coating*. *Nanotechnologies in Russia*, **2010**. 5(1-2): p. 67-72.
38. Chen, J., et al., *Controllable fabrication of 2D colloidal-crystal films with polystyrene nanospheres of various diameters by spin-coating*. *Applied Surface Science*, **2013**. 270: p. 6-15.
39. van Duffel, B., et al., *Langmuir-Blodgett deposition and optical diffraction of two-dimensional opal*. *Journal of Materials Chemistry*, **2001**. 11(12): p. 3333-3336.
40. Vogel, N., et al., *A Convenient Method to Produce Close- and Non-close-Packed Monolayers using Direct Assembly at the Air-Water Interface and Subsequent Plasma-Induced Size Reduction*. *Macromolecular Chemistry and Physics*, **2011**. 212(16): p. 1719-1734.
41. Meng, X. and D. Qiu, *Gas-Flow-Induced Reorientation to Centimeter-Sized Two-Dimensional Colloidal Single Crystal of Polystyrene Particle*. *Langmuir*, **2014**. 30(11): p. 3019-3023.
42. Wen, T. and S.A. Majetich, *Ultra-Large-Area Self-Assembled Mono layers of Nanoparticles*. *ACS Nano*, **2011**. 5(11): p. 8868-8876.
43. Edwards, T.D. and M.A. Bevan, *Controlling Colloidal Particles with Electric Fields*. *Langmuir*, **2014**. 30(36): p. 10793-10803.
44. Tracy, J.B. and T.M. Crawford, *Magnetic field-directed self-assembly of magnetic nanoparticles*. *MRS Bulletin*, **2013**. 38(11): p. 915-920.

45. Haes, A.J. and R.P. Van Duyne, *A unified view of propagating and localized surface plasmon resonance biosensors*. *Analytical and Bioanalytical Chemistry*, **2004**. 379(7-8): p. 920-930.
46. Martines, E., et al., *Superhydrophobicity and superhydrophilicity of regular nanopatterns*. *Nano Letters*, **2005**. 5(10): p. 2097-2103.
47. Cheng, Y.T. and D.E. Rodak, *Is the lotus leaf superhydrophobic?* *Applied Physics Letters*, **2005**. 86(14).
48. Guo, Z., W. Liu, and B.-L. Su, *Superhydrophobic surfaces: From natural to biomimetic to functional*. *Journal of Colloid and Interface Science*, **2011**. 353(2): p. 335-355.
49. NEINHUIS, C. and W. BARTHLOTT, *Characterization and Distribution of Water-repellent, Self-cleaning Plant Surfaces*. *Annals of Botany*, **1997**. 79(6): p. 667-677.
50. Kosiorek, A., et al., *Shadow Nanosphere Lithography: Simulation and Experiment*. *Nano Letters*, **2004**. 4(7): p. 1359-1363.
51. Zhang, J., et al., *Colloidal Self-Assembly Meets Nanofabrication: From Two-Dimensional Colloidal Crystals to Nanostructure Arrays*. *Advanced Materials*, **2010**. 22(38): p. 4249-4269.
52. Haes, A.J., et al., *A localized surface plasmon resonance biosensor: First steps toward an assay for Alzheimer's disease*. *Nano Letters*, **2004**. 4(6): p. 1029-1034.
53. Kitaev, V. and G.A. Ozin, *Self-assembled surface patterns of binary colloidal crystals*. *Advanced Materials*, **2003**. 15(1): p. 75-+.
54. Velikov, K.P., et al., *Layer-by-layer growth of binary colloidal crystals*. *Science*, **2002**. 296(5565): p. 106-109.
55. Detrich, A., et al., *Langmuir and Langmuir-Blodgett Films of Bidisperse Silica Nanoparticles*. *Langmuir*, **2010**. 26(4): p. 2694-2699.
56. Vogel, N., et al., *Wafer-Scale Fabrication of Ordered Binary Colloidal Monolayers with Adjustable Stoichiometries*. *Advanced Functional Materials*, **2011**. 21(16): p. 3064-3073.
57. Staudt, T., et al., *Magnetic Polymer/Nickel Hybrid Nanoparticles Via Miniemulsion Polymerization*. *Macromolecular Chemistry and Physics*, **2013**. 214(19): p. 2213-2222.
58. Vogel, N., et al., *Accurate Elemental Analysis of Metal-Containing Polymer Latexes Using ICP-Optical Emission Spectrometry*. *Macromolecular Chemistry and Physics*, **2010**. 211(12): p. 1355-1368.
59. Yin, Y., et al., *Template-Assisted Self-Assembly: A Practical Route to Complex Aggregates of Monodispersed Colloids with Well-Defined Sizes, Shapes, and Structures*. *Journal of the American Chemical Society*, **2001**. 123(36): p. 8718-8729.

60. Yang, P.a.D., Tao and Zhao, Dongyuan and Feng, Pingyun and Pine, David and Chmelka, Bradley F. and Whitesides, George M. and Stucky, Galen D., *Hierarchically Ordered Oxides*. Science, **1998**. 282: p. 2244-2246.
61. Bellido, E., et al., *Structuration and Integration of Magnetic Nanoparticles on Surfaces and Devices*. Small, **2012**. 8(10): p. 1465-1491.
62. Confalonieri, G.A.B., et al., *Template-assisted self-assembly of individual and clusters of magnetic nanoparticles*. Nanotechnology, **2011**. 22(28): p. 285608.
63. Xia, Y., et al., *Unconventional Methods for Fabricating and Patterning Nanostructures*. Chemical Reviews, **1999**. 99(7): p. 1823-1848.
64. Hanske, C., et al., *Strongly Coupled Plasmonic Modes on Macroscopic Areas via Template-Assisted Colloidal Self-Assembly*. Nano Letters, **2014**. 14(12): p. 6863-6871.
65. Ye, Y.H., et al., *Self-assembly of colloidal spheres on patterned substrates*. Applied Physics Letters, **2001**. 79(6): p. 872-874.
66. Rycenga, M., P.H.C. Camargo, and Y. Xia, *Template-assisted self-assembly: a versatile approach to complex micro- and nanostructures*. Soft Matter, **2009**. 5(6): p. 1129-1136.
67. Varghese, B., et al., *Size Selective Assembly of Colloidal Particles on a Template by Directed Self-Assembly Technique*. Langmuir, **2006**. 22(19): p. 8248-8252.
68. Mammen, L., et al., *Functional superhydrophobic surfaces made of Janus micropillars*. Soft Matter, **2015**. 11(3): p. 506-515.
69. Tien, J., A. Terfort, and G.M. Whitesides, *Microfabrication through Electrostatic Self-Assembly*. Langmuir, **1997**. 13(20): p. 5349-5355.
70. Fulda, K.U. and B. Tiede, *Monolayers of mono- and bidisperse spherical polymer particles at the air/water interface and Langmuir-Blodgett layers on solid substrates*. Supramolecular Science, **1997**. 4(3-4): p. 265-273.
71. Srivastava, S., et al., *Tunable Nanoparticle Arrays at Charged Interfaces*. ACS Nano, **2014**. 8(10): p. 9857-9866.
72. Sciortino, F., et al., *Self-assembly of patchy particles into polymer chains: A parameter-free comparison between Wertheim theory and Monte Carlo simulation*. Journal of Chemical Physics, **2007**. 126(19).
73. Edwards, E.W., D. Wang, and H. Mohwald, *Hierarchical organization of colloidal particles: From colloidal crystallization to supraparticle chemistry*. Macromolecular Chemistry and Physics, **2007**. 208(5): p. 439-445.
74. Zhang and S.C. Glotzer, *Self-Assembly of Patchy Particles*. Nano Letters, **2004**. 4(8): p. 1407-1413.

75. Niemeyer, C.M. and U. Simon, *DNA-Based Assembly of Metal Nanoparticles*. European Journal of Inorganic Chemistry, **2005**. 2005(18): p. 3641-3655.
76. Taton, T.A., et al., *The DNA-Mediated Formation of Supramolecular Mono- and Multilayered Nanoparticle Structures*. Journal of the American Chemical Society, **2000**. 122(26): p. 6305-6306.
77. Lalander, C.H., et al., *DNA-Directed Self-Assembly of Gold Nanoparticles onto Nanopatterned Surfaces: Controlled Placement of Individual Nanoparticles into Regular Arrays*. ACS Nano, **2010**. 4(10): p. 6153-6161.
78. Mirkin, C.A., et al., *A DNA-based method for rationally assembling nanoparticles into macroscopic materials*. Nature, **1996**. 382(6592): p. 607-609.
79. Wang, Y., et al., *Colloids with valence and specific directional bonding*. Nature, **2012**. 491(7422): p. 51-55.
80. Yi, G.-R., D.J. Pine, and S. Sacanna, *Recent progress on patchy colloids and their self-assembly*. Journal of Physics-Condensed Matter, **2013**. 25(19).
81. Glotzer, S.C. and M.J. Solomon, *Anisotropy of building blocks and their assembly into complex structures*. Nat Mater, **2007**. 6(7): p. 557-562.
82. Kraft, D.J., et al., *Surface roughness directed self-assembly of patchy particles into colloidal micelles*. Proceedings of the National Academy of Sciences of the United States of America, **2012**. 109(27): p. 10787-10792.
83. Pawar, A.B. and I. Kretzschmar, *Fabrication, Assembly, and Application of Patchy Particles*. Macromolecular Rapid Communications, **2010**. 31(2): p. 150-168.
84. Langmuir, I., *The constitution and fundamental properties of solids and liquids. II. Liquids*. Journal of the American Chemical Society, **1917**. 39: p. 1848-1906.
85. Blodgett, K.B., *Monomolecular films of fatty acids on glass*. Journal of the American Chemical Society, **1934**. 56: p. 495-495.
86. Dervichian, D.G., *Changes of Phase and Transformations of Higher Order in Monolayers*. The Journal of Chemical Physics, **1939**. 7(10): p. 931-948.
87. Vollhardt, D., *Morphology and phase behavior of monolayers*. Advances in Colloid and Interface Science, **1996**. 64(0): p. 143-171.
88. Blodgett, K.B., *Films built by depositing successive monomolecular layers on a solid surface*. Journal of the American Chemical Society, **1935**. 57(1): p. 1007-1022.
89. Langmuir, I. and V.J. Schaefer, *The Effect of Dissolved Salts on Insoluble Monolayers*. Journal of the American Chemical Society, **1937**. 59(11): p. 2400-2414.
90. Langmuir, I. and V.J. Schaefer, *Built-up films of proteins and their properties*. Science, **1937**. 85: p. 76-80

91. Knoll, M., *Charge potential and secondary emissions of electron irradiated bodies*. Physikalische Zeitschrift, **1935**. 36: p. 861-869.
92. Binnig, G., C.F. Quate, and C. Gerber, *ATOMIC FORCE MICROSCOPE*. Physical Review Letters, **1986**. 56(9): p. 930-933.
93. Vogel, N., et al., *Direct visualization of the interfacial position of colloidal particles and their assemblies*. Nanoscale, **2014**. 6(12): p. 6879-6885.
94. Lyklema, J., *Fundamentals of Interface and Colloid Science*. Vol. III. 2000: Academic Press.
95. Dinsmore, A.D., et al., *Colloidosomes: Selectively Permeable Capsules Composed of Colloidal Particles*. Science, **2002**. 298(5595): p. 1006-1009.
96. Binks, B.P., *Particles as surfactants - similarities and differences*. Current Opinion in Colloid & Interface Science, **2002**. 7(1-2): p. 21-41.
97. Ding, A.L., B.P. Binks, and W.A. Goedel, *Influence of particle hydrophobicity on particle-assisted wetting*. Langmuir, **2005**. 21(4): p. 1371-1376.
98. Ding, A.L. and W.A. Goedel, *Experimental investigation of particle-assisted wetting*. Journal of the American Chemical Society, **2006**. 128(15): p. 4930-4931.
99. McGorty, R., et al., *Colloidal self-assembly at an interface*. Materials Today, **2010**. 13(6): p. 34-42.
100. Vogel, N., C.K. Weiss, and K. Landfester, *From soft to hard: the generation of functional and complex colloidal monolayers for nanolithography*. Soft Matter, **2012**. 8: p. 4044-4061.
101. Kolle, M., et al., *Mimicking the colourful wing scale structure of the Papilio blumei butterfly*. Nature Nano, **2010**. 5(7): p. 511-515.
102. Romanov, S.G., et al., *Probing guided modes in a monolayer colloidal crystal on a flat metal film*. Physical Review B, **2012**. 86(19): p. 195145.
103. Bley, K., et al., *Switching light with light - advanced functional colloidal monolayers*. Nanoscale, **2014**. 6(1): p. 492-502.
104. Manzke, A., et al., *Formation of highly ordered alloy nanoparticles based on precursor-filled latex spheres*. Chem.Mater., **2012**. 24: p. 1048-1054.
105. Manzke, A., et al., *Arrays of size and distance controlled platinum nanoparticles fabricated by a colloidal method*. Nanoscale, **2011**. 3(6): p. 2523-2528.
106. Wang, W.G., et al., *Parallel fabrication of magnetic tunnel junction nanopillars by nanosphere lithography*. Sci. Rep., **2013**. 3.

107. Shiu, J.-Y., et al., *Fabrication of Tunable Superhydrophobic Surfaces by Nanosphere Lithography*. Chemistry of Materials, **2004**. 16(4): p. 561-564.
108. Li, Y., et al., *Biomimetic Surfaces for High-Performance Optics*. Advanced Materials, **2009**. 21(46): p. 4731-4734.
109. Vogel, N., et al., *Transparency and damage tolerance of patternable omniphobic lubricated surfaces based on inverse colloidal monolayers*. Nat Commun, **2013**. 4.
110. Xu, L. and J. He, *Fabrication of Highly Transparent Superhydrophobic Coatings from Hollow Silica Nanoparticles*. Langmuir, **2012**. 28(19): p. 7512-7518.
111. Haynes, C.L. and R.P. Van Duyne, *Nanosphere Lithography: A Versatile Nanofabrication Tool for Studies of Size-Dependent Nanoparticle Optics*. J. Phys. Chem. B, **2001**. 105(24): p. 5599-5611.
112. Anker, J.N., et al., *Biosensing with plasmonic nanosensors*. Nature Mater., **2008**. 7(6): p. 442-453.
113. Vogel, N., et al., *Reusable Localized Surface Plasmon Sensors Based on Ultrastable Nanostructures*. Small, **2010**. 6(1): p. 104-109.
114. Battaglia, C., et al., *Light Trapping in Solar Cells: Can Periodic Beat Random?* ACS Nano, **2012**. 6(3): p. 2790-2797.
115. Zhu, J., et al., *Nanodome Solar Cells with Efficient Light Management and Self-Cleaning*. Nano Letters, **2010**. 10(6): p. 1979-1984.
116. Raccis, R., et al., *Confined Diffusion in Periodic Porous Nanostructures*. Acs Nano, **2011**. 5(6): p. 4607-4616.
117. Jung, M., N. Vogel, and I. Koeper, *Nanoscale Patterning of Solid Supported Lipid Bilayer Membranes by Integrated Diffusion Barriers*. Langmuir, **2011**. 27(11): p. 7008.
118. Yunker, P.J., et al., *Suppression of the coffee-ring effect by shape-dependent capillary interactions*. Nature, **2011**. 476(7360): p. 308-311.
119. Kaz, D.M., et al., *Physical ageing of the contact line on colloidal particles at liquid interfaces*. Nature Mater., **2012**. 11(2): p. 138-142.
120. Manoharan, V.N., M.T. Elsesser, and D.J. Pine, *Dense packing and symmetry in small clusters of microspheres*. Science, **2003**. 301(5632): p. 483-487.
121. Paunov, V.N., *Novel Method for Determining the Three-Phase Contact Angle of Colloid Particles Adsorbed at Air–Water and Oil–Water Interfaces*. Langmuir, **2003**. 19(19): p. 7970-7976.
122. Isa, L., et al., *Measuring single-nanoparticle wetting properties by freeze-fracture shadow-casting cryo-scanning electron microscopy*. Nat Commun, **2011**. 2: p. 438.

123. Binks, B.P., L. Isa, and A.T. Tyowua, *Direct Measurement of Contact Angles of Silica Particles in Relation to Double Inversion of Pickering Emulsions*. Langmuir, **2013**. 29(16): p. 4923-4927.
124. Cayre, O.J. and V.N. Paunov, *Contact angles of colloid silica and gold particles at air-water and oil-water interfaces determined with the gel trapping technique*. Langmuir, **2004**. 20(22): p. 9594-9599.
125. Paunov, V.N. and O.J. Cayre, *Supraparticles and "Janus" particles fabricated by replication of particle monolayers at liquid surfaces using a gel trapping technique*. Advanced Materials, **2004**. 16(9-10): p. 788-791.
126. Mankidy, P.J., R. Rajagopalan, and H.C. Foley, *Facile catalytic growth of cyanoacrylate nanofibers*. Chem. Commun, **2006**: p. 1139-1141.
127. Ryan, B. and G. McCann, *Novel sub-ceiling temperature rapid depolymerization-repolymerization reaction of cyanoacrylate polymers*. Macromol. Rapid Commun., **1996**. 17: p. 217-227.
128. Kulkarni, R.K., D.E. Bartak, and F. Leonard, *Initiation of Polymerization of Alkyl 2-Cyanoacrylates in Aqueous Solution of Glycine and Its Derivatives*. J. Polym. Sci.: Part A-1, **1971**. 9: p. 2977-2981.
129. Weiss, C.K., U. Ziener, and K. Landfester, *A route to non-functionalized and functionalized poly (n-butylcyanoacrylate) nanoparticles: preparation in miniemulsion*. Macromolecules, **2007**. 40: p. 928-938.
130. Pepper, D.C. and B. Ryan, *Initiation Process in Polymerization of Alkyl Cyanoacrylates by Tertiary Amines: Inhibition by Strong Acids*. Makromol. Chem., **1983**. 184: p. 383-394.
131. Ducker, W.A., T.J. Senden, and R.M. Pashley, *Direct measurement of colloidal forces using an atomic force microscope*. Nature, **1991**. 353(6341): p. 239-241.
132. Butt, H.-J., *Measuring electrostatic, van der Waals, and hydration forces in electrolyte solutions with an atomic force microscope*. Biophys. J., **1991**. 60(6): p. 1438-1444.
133. Preuss, M. and H.-J. Butt, *Measuring the Contact Angle of Individual Colloidal Particles*. J. Colloid Interf. Sci., **1998**. 208(2): p. 468-477.
134. Pradip, et al., *Polymer-polymer complexation in dilute aqueous solutions: poly(acrylic acid)-poly(ethylene oxide) and poly(acrylic acid)-poly(vinylpyrrolidone)*. Langmuir, **1991**. 7(10): p. 2108-2111.
135. Park, B.J., et al., *Direct measurements of the effects of salt and surfactant on interaction forces between colloidal particles at water-oil interfaces*. Langmuir, **2008**. 24(5): p. 1686-1694.
136. Park, B.J., J. Vermant, and E.M. Furst, *Heterogeneity of the electrostatic repulsion between colloids at the oil-water interface*. Soft Matter, **2010**. 6(21): p. 5327-5333.

137. Akcora, P., et al., *Anisotropic self-assembly of spherical polymer-grafted nanoparticles*. Nature Materials, **2009**. 8(4): p. 354-9.
138. Ghezzi, F., et al., *Pattern formation in colloidal monolayers at the air-water interface*. Journal of Colloid and Interface Science, **2001**. 238(2): p. 433-446.
139. Lafitte, T., S.K. Kumar, and A.Z. Panagiotopoulos, *Self-assembly of polymer-grafted nanoparticles in thin films*. Soft Matter, **2014**. 10(5): p. 786-794.
140. Ghezzi, F. and J.C. Earnshaw, *Formation of meso-structures in colloidal monolayers*. Journal of Physics-Condensed Matter, **1997**. 9(37): p. L517-L523.
141. Chen, W., et al., *Measured long-ranged attractive interaction between charged polystyrene latex spheres at a water-air interface*. Physical Review E, **2006**. 74(2).
142. Fernández-Toledano, J.C., et al., *Spontaneous Formation of Mesostructures in Colloidal Monolayers Trapped at the Air-Water Interface: A Simple Explanation*. Langmuir, **2004**. 20(17): p. 6977-6980.
143. Hansen, F.K. and J. Ugelstad, *PARTICLE NUCLEATION IN EMULSION POLYMERIZATION .1. THEORY FOR HOMOGENEOUS NUCLEATION*. Journal of Polymer Science Part a-Polymer Chemistry, **1978**. 16(8): p. 1953-1979.
144. Hansen, F.K. and J. Ugelstad, *PARTICLE NUCLEATION IN EMULSION POLYMERIZATION .2. NUCLEATION IN EMULSIFIER-FREE SYSTEMS INVESTIGATED BY SEED POLYMERIZATION*. Journal of Polymer Science Part a-Polymer Chemistry, **1979**. 17(10): p. 3033-3045.
145. Maxwell, I.A., et al., *Entry of free radicals into latex particles in emulsion polymerization*. Macromolecules, **1991**. 24(7): p. 1629-1640.
146. Reynaert, S., P. Moldenaers, and J. Vermant, *Control over colloidal aggregation in monolayers of latex particles at the oil-water interface*. Langmuir, **2006**. 22(11): p. 4936-4945.
147. Alexandridis, P. and T. Alan Hatton, *Poly(ethylene oxide) • poly(propylene oxide) • poly(ethylene oxide) block copolymer surfactants in aqueous solutions and at interfaces: thermodynamics, structure, dynamics, and modeling*. Colloids and Surfaces A: Physicochemical and Engineering Aspects, **1995**. 96(1-2): p. 1-46.
148. Álvarez-Ramírez, J.G., et al., *Phase behavior of the Pluronic P103/water system in the dilute and semi-dilute regimes*. Journal of Colloid and Interface Science, **2009**. 333(2): p. 655-662.
149. Wanka, G., H. Hoffmann, and W. Ulbricht, *Phase Diagrams and Aggregation Behavior of Poly(oxyethylene)-Poly(oxypropylene)-Poly(oxyethylene) Triblock Copolymers in Aqueous Solutions*. Macromolecules, **1994**. 27(15): p. 4145-4159.
150. Zhou, S., et al., *One-Dimensional Assembly of Silica Nanospheres: Effects of Nonionic Block Copolymers*. Langmuir, **2012**. 28(37): p. 13181-13188.

151. Wang, J., et al., *Chain-like nanostructures from anisotropic self-assembly of semiconducting metal oxide nanoparticles with a block copolymer*. Chemical Communications, **2012**. 48(90): p. 11115-11117.
152. Langmuir, I., *Two-dimensional gases, liquids and solids*. Science, **1936**. 84(2183): p. 379-383.
153. Patil, G.S., D.G. Cornwell, and R.H. Matthews, *EFFECT OF IONIZATION AND CATION SELECTIVITY ON EXPANSION OF STEARIC ACID MONOLAYERS*. Journal of Lipid Research, **1972**. 13(5): p. 574-&.
154. Tomoaia-Cotișel, M., et al., *Insoluble mixed monolayers: III. The ionization characteristics of some fatty acids at the air/water interface*. Journal of Colloid and Interface Science, **1987**. 117(2): p. 464-476.
155. Rager, T., W.H. Meyer, and G. Wegner, *Micelle formation of poly(acrylic acid)-block-poly(methyl methacrylate) block copolymers in mixtures of water with organic solvents*. Macromolecular Chemistry and Physics, **1999**. 200(7): p. 1672-1680.
156. Rager, T., et al., *Block copolymer micelles as seed in emulsion polymerization*. Macromolecular Chemistry and Physics, **1999**. 200(7): p. 1681-1691.
157. Schmidle, H., et al., *Phase diagram of two-dimensional systems of dipole-like colloids*. Soft Matter, **2012**. 8(5): p. 1521-1531.
158. Niwa, M., N. Katsurada, and N. Higashi, *Formation of a surface monolayer and built-up multilayer from a well-defined amphiphilic block copolymer*. Macromolecules, **1988**. 21(6): p. 1878-1880.
159. Wypych, G., *Handbook of polymers*. 2012: ChemTec Publishing.
160. *Physical Properties of Polymers Handbook*, ed. J.E. Mark. 2007: Springer.
161. Onoda, G.Y., *Direct observation of two-dimensional, dynamic clustering and ordering with colloids*. Physical Review Letters, **1985**. 55(2): p. 226-229.
162. Hurd, A.J. and D.W. Schaefer, *Diffusion-Limited Aggregation in Two Dimensions*. Physical Review Letters, **1985**. 54(10): p. 1043-1046.
163. Ohno, K., et al., *Suspensions of Silica Particles Grafted with Concentrated Polymer Brush: Effects of Graft Chain Length on Brush Layer Thickness and Colloidal Crystallization*. Macromolecules, **2007**. 40(25): p. 9143-9150.
164. Spatz, J.P., et al., *Ordered Deposition of Inorganic Clusters from Micellar Block Copolymer Films*. Langmuir, **2000**. 16(2): p. 407-415.
165. Mahynski, N.A., S.K. Kumar, and A.Z. Panagiotopoulos, *Tuning polymer architecture to manipulate the relative stability of different colloid crystal morphologies*. Soft Matter, **2015**. 11(25): p. 5146-5153.

166. Mahynski, N.A. and A.Z. Panagiotopoulos, *Grafted nanoparticles as soft patchy colloids: Self-assembly versus phase separation*. Journal of Chemical Physics, **2015**. 142(7).
167. Furukawa, H., et al., *Light-Controlled On-Off Switch of a Fluorescent Nanoparticle*. Macromolecular Rapid Communications, **2008**. 29(7): p. 547-551.
168. Landfester, K. and C.K. Weiss, *Encapsulation by Miniemulsion Polymerization*. Advances in Polymer Science, **2010**. 229: p. 1-49.
169. Weiss, C.K. and K. Landfester, *Miniemulsion Polymerization as a Means to Encapsulate Organic and Inorganic Materials*. Advances in Polymer Science, **2010**. 233: p. 185-236.
170. Hansen, F.K. and J. Ugelstad, *Particle Nucleation in Emulsion Polymerization 3. Nucleation in Systems With Anionic Emulsifier Investigated by Seeded and Unseeded Polymerization*. Journal of Polymer Science Part A: Polymer Chemistry, **1979**. 17(10): p. 3047-3067.
171. Kong, X.Z. and E. Ruckenstein, *Core-shell latex particles consisting of polysiloxane-poly(styrene-methyl methacrylate-acrylic acid): Preparation and pore generation*. Journal of Applied Polymer Science, **1999**. 73(11): p. 2235-2245.
172. Fukaminato, T., et al., *Photochromism of diarylethene single molecules in polymer matrices*. Journal of the American Chemical Society, **2007**. 129(18): p. 5932-5938.
173. Nakamura, S., et al., *Theoretical investigation on photochromic diarylethene: A short review*. Journal of Photochemistry and Photobiology a-Chemistry, **2008**. 200(1): p. 10-18.
174. Li, Z.Y., H. Cheng, and C.C. Han, *Mechanism of Narrowly Dispersed Latex Formation in a Surfactant-Free Emulsion Polymerization of Styrene in Acetone-Water Mixture*. Macromolecules, **2012**. 45(7): p. 3231-3239.
175. Vogel, N., et al., *Wafer-Scale Fabrication of Ordered Binary Colloidal Monolayers with Adjustable Stoichiometries*. Adv. Funct. Mater., **2011**. 21(16): p. 3064-3073.
176. *CRC Chemical Handbook of Chemistry and Physics*. 94th ed. 2013.
177. Irie, M. and M. Morimoto, *Photochromic diarylethene molecules and crystals*. Pure and Applied Chemistry, **2009**. 81(9): p. 1655-1665.
178. Lerch, S., et al., *Nanoprobng the acidification process during intracellular uptake and trafficking*. Nanomedicine: Nanotechnology, Biology and Medicine, (0).
179. Clark, H.A., et al., *Optochemical Nanosensors and Subcellular Applications in Living Cells*. Microchimica Acta, **1999**. 131(1): p. 121-128.
180. Kreft, O., et al., *Polymer microcapsules as mobile local pH-sensors*. Journal of Materials Chemistry, **2007**. 17(42): p. 4471-4476.

181. Park, E.J., et al., *Ratiometric optical PEBBLE nanosensors for real-time magnesium ion concentrations inside viable cells*. *Anal. Chem.*, **2003**. 75(15): p. 3784-3791.
182. Almdal, K., et al., *Erratum: Fluorescent gel particles in the nanometer range for detection of metabolites in living cells*. *Polymers for Advanced Technologies*, **2007**. 18(12): p. 1020-1020.
183. Koo Yong-Eun, L., et al., *Photonic Explorers Based on Multifunctional Nanoplatforms: In Vitro and In Vivo Biomedical Applications*, in *New Approaches in Biomedical Spectroscopy*. 2007, American Chemical Society. p. 200-218.
184. Iversen, T.-G., T. Skotland, and K. Sandvig, *Endocytosis and intracellular transport of nanoparticles: Present knowledge and need for future studies*. *Nano Today*, **2011**. 6(2): p. 176-185.
185. Maeda, K., Y. Kato, and Y. Sugiyama, *pH-dependent receptor/ligand dissociation as a determining factor for intracellular sorting of ligands for epidermal growth factor receptors in rat hepatocytes*. *Journal of Controlled Release*, **2002**. 82(1): p. 71-82.
186. Tannock, I.F. and D. Rotin, *Acid pH in Tumors and Its Potential for Therapeutic Exploitation*. *Cancer Research*, **1989**. 49(16): p. 4373-4384.
187. Lerch, S., et al., *Nanoprobng the acidification process during intracellular uptake and trafficking*. *Nanomedicine: Nanotechnology, Biology and Medicine*, **2015**(0).
188. Ganachaud, F., et al., *Surface characterisation of amine-containing latexes by charge titration and contact angle measurements*. *Colloids and Surfaces a-Physicochemical and Engineering Aspects*, **1998**. 137(1-3): p. 141-154.
189. Sauzedde, F., et al., *Emulsifier-free emulsion copolymerization of styrene with two different amino-containing monomers .2. Surface and colloidal characterization*. *Journal of Applied Polymer Science*, **1997**. 65(12): p. 2331-2342.
190. Lerch, S., *Uptake mechanism, intracellular trafficking and endo-isosomal pH monitoring of polystyrene nanoparticles*. 2011, Johannes Gutenber-Universität Mainz.
191. Zhang, F., et al., *Ion and pH Sensing with Colloidal Nanoparticles: Influence of Surface Charge on Sensing and Colloidal Properties*. *Chemphyschem*, **2010**. 11(3): p. 730-735.
192. Owen, C.S., et al., *pH-dependent intracellular quenching of the indicator carboxy-SNARF-1*. *Journal of Fluorescence*, **1992**. 2(2): p. 75-80.
193. Akiyuki Takahashi, Y.Z., Victoria E. Centonze and Brian Herman, *Measurement of Mitochondrial pH In Situ*. *BioTechniques*, **2001**. 30: p. 804-815.
194. Seksek, O. and J. Bolard, *Nuclear pH gradient in mammalian cells revealed by laser microspectrofluorimetry*. *Journal of Cell Science*, **1996**. 109: p. 257-262.

195. Nett, W. and J.W. Deitmer, *Simultaneous measurements of intracellular pH in the leech giant glial cell using 2',7'-bis-(2-carboxyethyl)-5,6-carboxyfluorescein and ion-sensitive microelectrodes*. Biophysical Journal, **1996**. 71(1): p. 394-402.
196. Tafani, M., et al., *Regulation of Intracellular pH Mediates Bax Activation in HeLa Cells Treated with Staurosporine or Tumor Necrosis Factor- $\alpha$* . Journal of Biological Chemistry, **2002**. 277(51): p. 49569-49576.
197. Rybak, S.L. and R.F. Murphy, *Primary cell cultures from murine kidney and heart differ in endosomal pH*. Journal of Cellular Physiology, **1998**. 176(1): p. 216-222.
198. Cain, C.C., D.M. Sipe, and R.F. Murphy, *REGULATION OF ENDOCYTIC PH BY THE NA<sup>+</sup>,K<sup>+</sup>-ATPASE IN LIVING CELLS*. Proceedings of the National Academy of Sciences of the United States of America, **1989**. 86(2): p. 544-548.
199. Bucci, C., et al., *RAB5A IS A COMMON COMPONENT OF THE APICAL AND BASOLATERAL ENDOCYTIC MACHINERY IN POLARIZED EPITHELIAL-CELLS*. Proceedings of the National Academy of Sciences of the United States of America, **1994**. 91(11): p. 5061-5065.
200. Vonderheit, A. and A. Helenius, *Rab7 associates with early endosomes to mediate sorting and transport of semliki forest virus to late endosomes*. Plos Biology, **2005**. 3(7): p. 1225-1238.
201. Lombardi, D., et al., *RAB9 FUNCTIONS IN TRANSPORT BETWEEN LATE ENDOSOMES AND THE TRANS GOLGI NETWORK*. Embo Journal, **1993**. 12(2): p. 677-682.
202. Sandin, P., et al., *High-Speed Imaging of Rab Family Small GTPases Reveals Rare Events in Nanoparticle Trafficking in Living Cells*. Acs Nano, **2012**. 6(2): p. 1513-1521.
203. Marshansky, V. and M. Futai, *The V-type H<sup>+</sup>-ATPase in vesicular trafficking: targeting, regulation and function*. Current Opinion in Cell Biology, **2008**. 20(4): p. 415-426.
204. Han, J. and K. Burgess, *Fluorescent Indicators for Intracellular pH*. Chemical Reviews, **2010**. 110(5): p. 2709-2728.
205. Ganachaud, F., et al., *PREPARATION AND CHARACTERIZATION OF CATIONIC POLYSTYRENE LATEX-PARTICLES OF DIFFERENT AMINATED SURFACE-CHARGES*. Polymers for Advanced Technologies, **1995**. 6(7): p. 480-488.
206. Musyanovych, A., et al., *Effect of Hydrophilic Comonomer and Surfactant Type on the Colloidal Stability and Size Distribution of Carboxyl- and Amino-Functionalized Polystyrene Particles Prepared by Miniemulsion Polymerization*. Langmuir, **2007**. 23(10): p. 5367-5376.